Magnetic Resonance Imaging of Cerebrovascular Anatomy and Physiology at 7 Tesla



Olivia M. Viessmann

Trinity College

University of Oxford

A thesis submitted for the degree of Doctor of Philosophy.

Hilary Term 2017



This thesis is licensed under a Creative Commons Attribution-NonCommercial-NoDerivatives 4.0 International License.

Abstract

Magnetic Resonance Imaging (MRI) can study the cerebrovasculature non-invasively in humans. It can image the vascular anatomy, as well as functional attributes such as flow and perfusion. This multi-modal capability renders MRI one of the most favourable imaging techniques to study the cerebrovasculature in research and in clinical settings.

The advent of human 7 Tesla (7T) MRI offers further benefits to existing methods. Most evidently, the higher signal-to-noise ratio (SNR) can be used to improve resolution. However concomitant changes in contrast mechanisms, an increase in the specific absorption rate (SAR) and transmit B_1-field inhomogeneity need to be addressed when transitioning to higher field. Vessel wall imaging (VWI) is an exemplar application that benefits from higher resolution but is based on SAR intense methods. In the first part of this thesis the implementation of a VWI method, DANTE-SPACE, is described. The readout scheme was specifically optimised for high resolution wall depiction and enhanced suppression of cerebrospinal fluid to produce vessel wall contrast in the major intracranial arteries at 7T.

Besides refining spatial scales, recent technical developments have accelerated information content in the temporal domain. In-slice acceleration and simultaneous excitation of multiple slices substantially reduced acquisition times for many applications. In particular, multiband techniques have pushed sampling speeds in functional MRI (fMRI) to sub-second regimes. Traditionally, fMRI is used to study low frequency neuro-vascular signals below 0.1Hz. Aliases of cardio-respiratory-induced signals have been regarded as "physiological noise". Sufficiently fast sampling resolves the spectrum beyond the cardiac frequency, thus transforming noise into valuable signal. In the second part of this thesis strategies to map and quantify signal fluctuations at the cardiac frequency are described using echo-planar imaging (EPI). Potential age-related difference in the cardiac EPI signal power were studied. Also, an investigation was made into the underlying MR-mechanisms that form these fluctuations by decomposing the EPI-signal over the cardiac cycle into S_0 and T_2^* waveforms. Ultimately this research aims to foster the understanding of the vascular origins of cardiac-induced EPI signals. This will hopefully serve future research into how EPI data can be exploited to study cerebrovascular properties in healthy and diseased states.

Acknowledgements

The work underpinning this thesis is based on the multiple levels of support I received from many people.

I am particularly grateful to Peter Jezzard, my supervisor who committed tremendous amounts of time guiding me through my DPhil years. He often put me back onto the right track when I diverted on some flawed MR meanders. One of his first year advice (we were discussing how I could validate simulations with experimental data) resonated with me again during thesis writing: "It's important to convince yourself first and then you can convince others". It can be difficult and frustrating, but an essential process to go through as a DPhil student.

A big thanks goes to the FMRIB Centre for being such a stimulating and supportive environment where no stupid or irrelevant questions exist. I tremendously benefited from Linqing Li's experience with DANTE; I very much appreciate the time he took to share his knowledge with me. I also thank Sam Hurley for the help with SNR calculations and image reconstruction and Robert Frost for helping me to handle TWIX data and getting my head around measurement data headers. I thank Mark Jenkinson, Mark Chiew and Tom Okell for the organisation of valuable teaching and lectures and for giving me the opportunity to gain my first teaching experience. I am grateful for all the feedback and critical discussions of my work with Karla Miller and Giovanna Zamboni. I am very grateful for the general help, practical advice, coffee breaks and travel fun with Wilfred, Hannah, Clark, Wenchuan, Robert, Ti, Adam, Ellie and in particular Nadine. I thank all Physics Group DPhil students and the PostDoc gang for the many cheerful lunchtime breaks filled with the most pressing questions of our time from "Would it be more convenient if we switched to metric time?"; "Why parboiled rice?" to "Why a banana is a berry, but a raspberry is not". I learned for life.

I thank Harald Möller and all of the NMR Group at the Max-Planck Institute in Leipzig for their very warm welcome and guidance during my stay in 2015. I thank John Mugler at the University of Virginia for the generous provision of `C++` source code for variable flip angle simulations.

I thank all the amazing friends I made in Oxford - you are my Basic DPhil Life Support. In particular I would like to thank Lien, Laura, Char, Catherine, Edyta, Emma, Robert, Jenni, Charly, Claire, Nabil, Marc, Nayab, Malte, Mauri and the porters.

Besonderer Dank gebührt meiner Familie: Meinen Eltern - vielen Dank für die stetige Erinnerung das sich der Mensch nicht durch Erfolg und Äußerlichkeiten definiert und all die Freiheiten die ihr mir immer geboten habt durch die Versicherung das Zuhause immer offen ist; meiner Schwester Sonja - ich bin Dir dankbar für das Gefühl nie Alleinsein zu müssen, egal wie weit die räumliche Entfernung ist (wenn man in Oxford vom Fahrrad fällt kann man in Düsseldorf anrufen); den Sörensens - für Eure Herzlichkeit; meiner Oma - Deine Großzügigkeit ist beispiellos; meinem Opa - mein Streben war immer Dich zu beeindrucken.

Contents

Publications related to this thesis xi
Abbreviations xiii
Mathematical symbols xvii
List of figures xxi
List of tables xxiv
Preface xxvi

1 Intracranial vessel wall imaging **1**

1.1 Motivation 1
1.1.1 Non-MRI methods 2
1.1.2 MRI methods 3
1.1.2.1 Intracranial vessel wall imaging 3
1.2 Background 4
1.2.1 Concepts of black-blood imaging 5
1.2.1.1 Inversion strategies 5
1.2.1.2 Phase spoiling strategies 6
1.2.2 Concepts of CSF suppression 12
1.3 Scope of this work 13
1.4 Implementation of DANTE-FLASH for VWI 14
1.4.1 DANTE and FLASH signals: Theory 14

1.4.2 Readout order 17
1.5 Methods 18
1.5.1 Simulation and phantom validation at 3T 18
1.5.1.1 MR data 20
1.5.2 *In-vivo* test at 3T 22
1.5.3 *In-vivo* test at 7T 23
1.6 Results 24
1.6.1 Simulation and phantom validation at 3T 24
1.6.2 *In-vivo* test at 3T 25
1.6.3 *In-vivo* test at 7T 26
1.7 Discussion 28
1.7.1 Simulation and phantom validation 28
1.7.2 *In-vivo* experience: 3T vs. 7T 31
1.8 Conclusion 31

2 Intracranial vessel wall imaging at 7T with DANTE-SPACE 33
2.1 Introduction 33
2.1.1 Scope of this work 34
2.2 Methods 34
2.2.1 SPACE optimisation 35
2.2.2 DANTE optimisation 39
2.2.2.1 Simulations 41
2.2.2.2 Signal loss due to brain movement 42
2.2.3 MR data 43
2.2.3.1 Vessel wall conspicuity: SPACE optimisation 43
2.2.3.2 Vessel wall boundary contrast: DANTE-SPACE vs. SPACE 43
2.2.3.3 Signal loss due to brain movement 44

2.2.4 Post-processing and image analysis 44
2.2.4.1 Image analysis of vessel wall conspicuity: SPACE optimisation 44
2.2.4.2 Image analysis of vessel wall boundary contrast: DANTE-SPACE vs. SPACE 45
2.2.4.3 Image analysis of signal loss due to brain movement 49
2.2.5 Patient scan 49
2.3 Results 50
2.3.1 SPACE optimisation 50
2.3.2 DANTE optimisation 51
2.3.3 DANTE-SPACE vs. SPACE 53
2.3.3.1 Signal loss due to brain movement 55
2.3.4 Patient scan 56
2.4 Discussion and conclusion 57
2.4.1 Vessel wall conspicuity: SPACE optimisation 57
2.4.2 Vessel wall boundary contrast: DANTE-SPACE vs. SPACE 58

3 Low- and cardiac-frequency fluctuations in ultra-fast rs-fMRI data 61

3.1 Background 61
3.1.1 The rs-fMRI spectrum 62
3.1.1.1 Sampling speed and aliasing 62
3.1.1.2 Spectral composition 64
3.1.2 Quantifying spectral contributions 69
3.1.2.1 Amplitude of low frequency fluctuations . . . 69
3.1.2.2 Cardiac frequency fluctuations 71

3.1.3 Scope of this work 73
3.2 Methods 73
3.2.1 General linear model 73
3.2.2 Dual regression 76
3.2.2.1 Cardiac efficiency measure 79
3.2.3 Analysis goals 80
3.2.3.1 Initial vs. dual GLM 80
3.2.3.2 Age-related changes in the BOLD spectrum . 82
3.3 Data and post-processing 83
3.3.1 MR data 83
3.3.2 Post-processing 84
3.4 Results 85
3.4.1 Initial vs. dual GLM 85
3.4.2 Age-related changes 90
3.4.2.1 Low frequencies: fALFF vs. cfALFF 90
3.4.2.2 Cardiac frequencies: CEM and CPM 94
3.5 Discussion and conclusion 97
3.5.1 Initial vs. dual GLM 97
3.5.2 Age-related changes 99
3.5.3 Critical points 102
3.5.3.1 Normalisation 102

4 Origins and mechanisms of cardiac-frequency signal fluctuations in brain MRI time series data 103

4.1 Introduction 103
4.1.1 The arterial pressure wave in the brain 103
4.1.2 Means of measuring cerebral pulsatility 105
4.1.2.1 MR methods to study cerebral pulsatility . . 105

4.1.3 Clinical relevance of cardiac pulsatility 107
4.1.4 Scope of this work 108
4.2 Theory 110
4.2.1 Shear wave-induced displacement 110
4.2.2 S_0 and T_2^* fluctuations 111
4.2.2.1 S_0 111
4.2.2.2 T_2^* 112
4.2.2.3 Effect of S_0 and T_2^* fluctuations on the signal phase 116
4.3 Methods 120
4.3.1 Cardiac phase mapping 120
4.3.1.1 Simulation of cardiac phase data 121
4.3.2 S_0 and T_2^* mapping 125
4.3.3 $T_2^*(\tau)$ simulations 128
4.3.4 MR data and post-processing 131
4.3.4.1 Cardiac phase mapping: single-echo EPI . . . 132
4.3.4.2 S_0 and T_2^* mapping: dual-echo EPI 133
4.4 Results 135
4.4.1 Cardiac phase mapping 135
4.4.1.1 Tissue-specific results in EPI space 135
4.4.1.2 Area-specific phase distributions in standard space 135
4.4.2 S_0 and T_2^* mapping 138
4.4.2.1 Absolute T_2^* values 149
4.4.3 $T_2^*(\tau)$ simulations 150
4.4.3.1 Dynamic CSF volume model 150
4.4.3.2 Parenchymal volume fluctuation model 150

4.5 Discussion and conclusion 154
4.5.1 Critical points and limitations 155
4.5.2 Cardiac-related phase distribution and S_0/T_2^* fluctuations 156
4.5.3 On the $T_2^*(\tau)$ waveform 157
4.5.4 Clinical relevance 159
4.5.5 Brief summary of results 159

5 Future work **161**
5.1 DANTE for vessel-wall imaging at 7T 161
5.1.1 Motion correction and scan efficiency 161
5.2 Cardiac-induced fluctuations in EPI time series 163
5.2.1 Methodologies 163
5.2.1.1 GLM approach to map cardiac fluctuations . 163
5.2.1.2 Cardiac phase mapping 164
5.2.1.3 Mapping MR variables over the cardiac cycle 164
5.2.2 Neuroscientifically relevant ideas 165
5.2.2.1 Glymphatic system theory 166
5.2.2.2 Vascular anatomical network model to simulate cardiac-induced MR signals 168
5.2.3 Clinically relevant ideas 169
Bibliography 171

Appendices **193**

A How to run variable flip angle simulations **195**

B χ^2 - goodness of fit for measured vs. simulated data **201**

Publications related to this thesis

Journal articles

"T2-Weighted intracranial vessel wall imaging at 7 Tesla using a DANTE-prepared variable flip angle turbo spin echo readout (DANTE-SPACE)". **O. Viessmann**, L. Li, P. Benjamin and P. Jezzard. *Magnetic Resonance in Medicine*, 77:655-663, 2016.

"7 Tesla MRI in cerebral small vessel disease". P. Benjamin, **O. Viessmann**, A. MacKinnon, P. Jezzard and H. Markus. *International Journal of Stroke*, 10:659-664, 2015.

"Origin and Mechanisms of Cardiac-Frequency Signal Fluctuations in Brain MRI Time Series Data". **O. Viessmann**, H. E. Möller and P. Jezzard. Submitted to *NeuroImage* and currently under review.

Conference proceedings

"Feasibility and Signal Analysis of DANTE-TSE with Variable Flip Angles for Intracranial Vessel Wall Imaging at 7 Tesla". **O. Viessmann** , L. Li and P. Jezzard, '. Proceedings of the ISMRM, Toronto 2015.

"Improved Characterization of Low-Frequency Fluctuations in Resting-State fMRI using GLM Correction of Baseline and Physiological Noise". **O. Viessmann**, P. Jezzard and H. Moeller. Proceedings of the ISMRM, Singapore 2016.

"EPI-signal fluctuations at the cardiac frequency: A tissue-specific quan-

tification of inflow, displacement and potential oxygenation effects over the cardiac cycle". **O. Viessmann** and P. Jezzard. Proceedings of the ISMRM, Honolulu 2017.

Abbreviations

2D; 3D = 2-dimensional; 3-dimensional,

3T; 7T = 3 Tesla; 7 Tesla,

ADC = analogue-to-digital converter,

ALFF = amplitude of low-frequency fluctuations,

A≫P = anterior to posterior,

BB = black blood,

BOLD = blood-oxygen-level-dependent,

BW = bandwidth,

CAIPIRINHA = controlled aliasing in parallel imaging results in higher acceleration,

CBF = cerebral blood flow,

CBV = cerebral blood volume,

CEM = cardiac efficiency metric,

cfALFF = cleaned fractional amplitude of low-frequency fluctuations,

cGM = cortical grey matter,

CNR = contrast-to-noise ratio,

CPM = cardiac pulsatility metric,

CSF = cerebrospinal fluid,

CTA = computed tomography angiography,

DANTE = delay alternating with nutation for tailored excitation,

dGM = deep grey matter,
DIR = double-inversion recovery,
DSA = digital subtraction angiography,
EPI = echo-planar imaging,
ESP = inter-echo spacing,
ETL = echo train length,
fALFF = fractional amplitude of low-frequency fluctuations,
fMRI = functional magnetic resonance imaging,
FA = flip angle,
FLAIR = fluid-attenuated inversion recovery,
FLASH = fast low angle shot,
FLIRT = FSL's linear registration tool,
FNIRT = FSL's non-linear registration tool,
FOV = field of view,
FSL = FMRIB's software library,
FWHM = full-width at half maximum,
GLM = general linear model,
GM = grey matter,
gof = goodness of fit,
GRAPPA = generalized autocalibrating partially parallel acquisition,
GRE = gradient-recalled echo,
HRF = haemodynamic response function,
Hb = haemoglobin,
Hct = haematocrit,
Hz/px = Hertz/pixel,
H$\gg$F = head to feet,
ICA = internal carotid artery or independent component

analysis,

ICP = intracranial pressure,

ISF = interstitial fluid,

k-space = spatial frequency space,

MCA = middle cerebral artery,

MPRAGE = magnetisation-prepared rapid gradient echo,

MP2RAGE = magnetisation-prepared rapid gradient echo with two inversion times,

MPIR = magnetisation-prepared inversion recovery,

MREG = magnetic resonance encephalography,

MRI = magnetic resonance imaging,

MSDE = motion-sensitized driven equilibrium,

MT = magnetisation transfer,

MTF = magnetisation-transfer function,

OCT = optical coherence tomography,

PC-MRA = phase-contrast magnetic resonance angiography,

PCA = posterior communicating artery,

PD = proton density,

$PETCO_2$ = partial pressure of end-tidal CO_2,

PI = pulsatility index,

PSF = point-spread function,

pulse-ox = pulse-oximetry,

PVE = partial volume estimate,

rs = resting state,

rs-fMRI = resting-state fMRI,

RF = radio-frequency,

RMSE = root-mean-square error,

ROI = region of interest,
RSFA = resting-state fluctuation amplitude,
R≫L = right to left,
SAR = specific absorption rate,
SE = spin echo,
SEM = standard error of the mean
SENSE = sensitivity encoding,
SMS = simultaneous multislice,
SNR = signal-to-noise ratio,
SPACE = sampling perfection with application optimised contrast using different flip angle evolutions,
SR = signal ratio,
SSFP = steady-state free precession,
SVD = small vessel disease,
SWI = susceptibility-weighted imaging
T_1-w = T_1-weighted,
T_2-prep = T_2-magnetisation-preparation,
TCS = transcranial Doppler sonography,
TE = echo time,
TOF = time-of-flight,
TR = repetition time,
TSE = turbo-spin echo,
TWIX = raw k-space data,
VAN = vascular anatomical network,
VISTA = volumetric isotropic turbo-spin echo acquisition,
VWI = vessel-wall imaging,
WM = white matter.

Mathematical symbols

Latin

A . . . . power amplitude,

B_0 . . . external magnetic field,

B_1 . . . transmit radio-frequency field,

c . . . . cardiac component or concentration of spins,

c_s . . . shear wave propagation speed,

d . . . . scaling factor,

D . . . tissue density,

$\hat{e}_i$ . . . . unit vector,

$\mathbf{E}$ . . . . relaxation matrix,

$\vec{G}$ . . . . field gradient or shear modulus,

f . . . . frequency,

f_a . . . alias frequency,

f_c . . . cardiac frequency,

fA . . . normalised power amplitude,

f_{max} . . maximum frequency,

f_s . . . . sampling frequency,

f_{true} . . true (non-aliased) frequency,

$F_{c,max}$. subset of maximum cardiac frequency components,

g . . . . g-ratio,

G . . . . scaled g-ratio or shear modulus,

i, j . . . counters,

$\vec{M}$ . . . . magnetisation vector,

M_0 . . . magnetisation at thermal equilibrium,

$M_\perp$ . . . transverse magnetisation component,

M_z . . . longitudinal magnetisation

MB . . . multiband factor,

n, N . . . number of samples/natural number,

p . . . . p-value (error probability),

$\vec{r}$ . . . . position vector,

$\mathbf{R}$ . . . . rotation matrix,

r . . . . respiratory component or reference voxel index,

s . . . . counter,

S . . . . signal in the time domain,

$\tilde{S}$ . . . . signal in the frequency domain,

S_0 . . . signal at "zero-echo time",

$S_{0,p}$ . . . normalized peak signal amplitude,

S_{multi} . . multi-exponential time domain signal,

t . . . . . time,

T_1 . . . . longitudinal relaxation time constant,

T_2 . . . . transverse relaxation time constant (spin-spin interaction),

T_2' . . . . transverse relaxation time constant (local field inhomogeneities),

T_2^* . . . effective transverse relaxation constant,

$T_{2,p}^*$ . . . normalized peak effective transverse relaxation time,

TE . . . echo time,

TE_{eq} . . equivalent echo time,

TI . . . . inversion time,

TR . . . repetition time,

v . . . . partial volume,

v_{art} . . arteriolar blood volume,

v_{cap} . . . capillary blood volume,

$\vec{v}$ . . . . velocity,

Y . . . . voxel power spectrum or oxygenation saturation,

X . . . physiological power spectrum.

Greek

α . . . . flip angle or baseline regressor,

β . . . . cardio-respiratory regressor,

γ . . . . gyromagnetic ratio,

ϵ . . . . error,

θ, ϑ . . . flip angles,

ν . . . spin velocity,

ν_{crit} . . critical spin velocity,

ρ . . . . proton spin density,

σ . . . . standard deviation,

τ . . . . gradient duration or cardiac unit cycle,

τ_c . . . systole-to-systole time period,

τ_d . . . delay between arteriolar and capillary blood volume fluctuations,

τ_D . . . DANTE inter-pulse time,

$\tau_{RF,D}$ . . DANTE RF pulse duration,

τ_{max} . . time of the maximum amplitude of a fluctuation,

ϕ_c . . . cardiac-cycle-related phase shift,

$\phi_{c,i}$ . . cardiac-cycle-related phase shift in voxel i,

$\phi_{i,r}$ . . timing-related phase shift between voxels i and r,

ω . . . . Larmor frequency.

Miscellaneous

$\overline{x}$ . . . . mean value of x,

$\langle x \rangle$ . . . average of x inside an ROI or tissue mask,

$\vec{\nabla}$ . . . . Nabla-operator ("Del"),

∂x . . . . partial derivative w.r.t. x,

x, y, z . . Cartesian spatial dimensions,

FFT . . Fast Fourier transform.

List of Figures

1.1 Single-slice DIR sequence diagram 6
1.2 MSDE sequence diagram 8
1.3 Variable flip angle TSE sequence diagram 9
1.4 DANTE module sequence diagram 11
1.5 Banding pattern simulation 17
1.6 DANTE-FLASH sequence diagram 18
1.7 DANTE simulation vs. experimental results in a static phantom 25
1.8 DANTE simulation vs. experimental results in a flow phantom 26
1.9 DANTE-FLASH simulation in grey matter 27
1.10 DANTE-FLASH *in-vivo* scan at 3T 27
1.11 DANTE-FLASH *in-vivo* scan at 7T 29

2.1 DANTE-SPACE sequence diagram 35
2.2 SPACE optimisation strategy 37
2.3 PSF simulations for different magnetisation evolution schemes 38
2.4 MCA vessel wall intensity profile 45
2.5 SNR and g-factor maps 46
2.6 Location of vessel wall signal masks 47
2.7 DANTE simulations for vessel wall, CSF and blood at 7T . . . 52
2.8 DANTE-SPACE images at the Circle of Willis 55

2.9 DANTE-SPACE images in a lacunar infarct paitient 56

3.1 Whole brain rs-fMRI spectrum and its contributors 63
3.2 Schematic plot of the BOLD HRF after a single time point neuronal activation 65
3.3 Schematic drawing of smooth muscle cells and vasculature . . 66
3.4 Respiratory spectrum for different sampling rates 68
3.5 Cardiac spectrum for different sampling rates 69
3.6 Representative whole brain rs-fMRI spectrum and cardio-respiratory spectra 74
3.7 GLM spatial regressor maps 75
3.8 Schematic overview of dual regression 78
3.9 Different cardiac spectral widths in a younger and an older subject 80
3.10 Spectra in different tissue before and after regression 87
3.11 Comparison of externally measured and refined physiological spectra 88
3.12 Zoom into pulse-ox and refined cardiac spectrum 89
3.13 Age group comparison of fALFF and cfALFF in different tissue 93
3.14 Age group comparison of regressor values and spatial extent in different tissues 95
3.15 Age group comparison of CEM in different tissue 96
3.16 Age group comparison of CPM in different tissue 96

4.1 Schematic arterial pressure waveform. 104
4.2 Arterial pressure waveforms measured with different modalities 106
4.3 Number of RF-excitations experienced for a spin travelling at different speeds 113

4.4 Simulated $S_0(\tau_c)$ and $T_2^*(\tau_c)$) waveforms and their EPI signals 118
4.5 External cardiac spectrum 121
4.6 Synthetic random time series 122
4.7 Phase map of randomly fluctuating voxels 122
4.8 Time series for code testing 123
4.9 Non-phase corrected time series data 124
4.10 Phase corrected time series data 124
4.11 Temporally shifted time series 125
4.12 Cardiac cycle segmentation of a dual-echo multiband sequence 127
4.13 Cardiac-thresholded tissue masks and anatomical reference . . 134
4.14 Phase distributions in different tissue compartments. 136
4.15 Area-specific distribution of cardiac phase values in MNI space. The light blue distribution on the top is the overall grey matter phase distribution that can be split into the cortical (red), putamen (pink), caudate (yellow), thalamus (green) and pallidum (dark blue) distributions. The peak in the cortical distribution is slightly shifted to the left of the dominant arterial phase peak at $-\pi/2$. Subcortical areas' peaks are shifted further apart. Each distribution histogram is displayed normalised to itself. 137
4.16 Cardiac unit cycle fluctuations of S_0 and T_2^* in the arterial mask. 138
4.17 Cardiac unit cycle fluctuations of S_0 and T_2^* in GM. 140
4.18 Arterial mask pulsatility in S_0 and T_2^* for all phase ranges . . 144
4.19 GM pulsatility in S_0 and T_2^* for all phase ranges 145
4.20 WM pulsatility in S_0 and T_2^* for all phase ranges 146
4.21 CSF pulsatility in S_0 and T_2^* for all phase ranges 147
4.22 Venous mask pulsatility in S_0 and T_2^* for all phase ranges . . . 148

4.23 Dynamic CSF volume model animation 151
4.24 Parenchymal volume fluctuation model animation 153

5.1 Partial volume model simulation with exchanging ISF compartment 168

B.1 χ^2 probability density distribution for 8 degrees of freedom. . . 202
B.2 α distribution per normalised χ^2/ν.The red and green dotted lines indicate the χ^2/ν from our model fit in Chapter 4, for the dynamic CSF volume and the parenchymal volume model respectively. 203

List of Tables

2.1 FWHM results for simulated and measured PSFs 50

2.2 SPACE vs. DANTE-SPACE results for SNR, SR and CNR . . 54

2.3 Results of brain motion-induced signal loss in DANTE 54

3.1 Average regressor values and spatial extent in different tissues 91

4.1 Literature values for systolic and diastolic flow velocities . . . 113

4.2 Estimates of oxygenation fluctuation-induced changes in T_2^* . . 116

4.3 Peak-to-peak percentage fluctuation of $S_{0,p}$, $T_{2,p}^*$ 141

4.4 Average T_2^* values in different tissue. 149

Preface

This thesis describes research on two major aspects of cerebrovascular magnetic resonance imaging (MRI) - anatomy and physiology.

The anatomical imaging work focusses on intracranial vessel wall imaging (VWI). Chapter 1 describes general MR concepts and strategies of black-blood imaging as well as vessel wall contrast. DANTE, the method used in this work, is introduced. The initial sequence implementation, comprising phantom tests, simulation validations and *in-vivo* scans on a 3 Tesla system are presented. Chapter 2 describes the implementation of DANTE-SPACE, a T_2-weighted sequence for *in-vivo* intracranial VWI at 7 Tesla (7T). The contrast-to-noise and effective resolution (point-spread-function analysis) of DANTE-SPACE in comparison to the vendor-provided default sequence is assessed in a study of healthy volunteers.

The physiological imaging aspect of this work is presented in Chapters 3 and 4. Chapter 3 introduces analysis strategies to map and quantify cardio-respiratory-induced fluctuations in echo-planar imaging (EPI) resting-state functional MRI using a general linear model and a refined dual regression model in the frequency domain. The introduced methods are then applied in a 7T study of "younger" and "older" volunteers to investigate if low-

frequency ($< 0.1\,\mathrm{Hz}$) and cardiac-frequency EPI power change in normal ageing. Chapter 4 presents novel methods to study cardiac-induced signal variations in EPI time series data. The phase dispersion of the magnitude EPI signal in different tissues and brain areas is investigated. An in-depth study into the origins and mechanisms of these signal fluctuations is conducted by disentangling the EPI signal into its underlying S_0 ("signal at zero-echo time") and T_2^* (effective transverse decay rate) waveforms over the cardiac cycle.

Chapter 1

Intracranial vessel wall imaging: Theory, implementation and validation

1.1 Motivation

Atherosclerosis is thought to be the cause of 25% of ischemic strokes [1]. The distinct causes are under debate and are thought to be widespread from traditional risk factors such as diet and lifestyle to infections and inflammatory diseases [2]. The disease is affecting all levels of the arteriovasculature, from the aorta to the peripheral arteries. Atherosclerotic lesions occur at the vessel wall and are referred to as plaques. Plaques vary in composition, for example extracellular matrix, cholesterol, collagen and macrophages are common components [3]. Early identification is important to prevent them to turn into so called vulnerable plaques, which are at high risk to rupture and cause thrombosis in the vessel [4]. Vessel wall imaging (VWI) comprises imaging techniques that assess arterial stenosis, luminal diameter, wall thick-

ness, plaque accumulation and composition. Studies in the aorta wall have in particular identified plaque thickness (with a reoccuring critical value of > 4mm in the literature) and composition, in particular calcification states, to be predictors of future vascular events, such as stroke and infarcts [5, 6]. VWI is applied to all larger arterial structures in the human body, from the peripheral arteries to the aorta, coronary and carotid arteries. Imaging modalities have advanced over the last decade and the regions of interest have moved further down the vascular tree to intracranial vessels.

1.1.1 Non-MRI methods

The most common non-MR VWI methods are computed tomography angiography (CTA), digital subtraction angiography (DSA) [7, 8], ultrasound and optical coherence tomography (OCT) [9]. CTA and DSA depict stenosis and luminal narrowing at sub-millimetre resolution, but are based on ionizing radiation. They require the administration of a contrast agent and the final image is based on the subtraction of the pre- and post-contrast image. As such the final image only depicts the contrast agent-filled lummen (inner vessel area) and lacks information about the wall itself which is inparticular problemativ when plaque lesions are turned inwards [10]. Ultrasound real-time imaging is used to measure the thickness of vessel walls which appear as a double-line pattern in a B-mode scan [11]. Ultrasound is a cheap, "easy-to-handle" technique with negligible bio-effects, but suffers from poor resolution and penetration depth and can only be applied to the brain in the area of the cranial window. However, intravascular application of ultrasound, using a catheter probe, has been shown to produce sub-millimetre resolution [12], but is highly invasive. Similarly, OCT uses catheter probes, but provides resolution on the micrometre scale. However, field of views are limited to a a

few millimetres, penetration depths are limited to a millimetre and the field of view has to be flushed from blood during imaging, limiting tolerable scan times [9].

1.1.2 MRI methods

The non-invasive nature, large field of view and reduced bio-effects render MRI an ideal tool to study the vessel wall and plaque accumulation in humans. The multi-contrast ability further allows the assessment of plaque composition and can facilitate the identification of vulnerable plaques before the subject becomes symptomatic [13, 14]. A typical protocol in a clinical setting comprises a bright-blood time-of-flight (TOF) angiography scan to localise the site of stenosis, a T_2- (transverse relaxation time constant) weighted VWI scan to visualise luminal narrowing, an additional T_1-(longitudinal relaxation time constant) and/or a proton density (PD) -weighted scan [15]. In some cases Gadolinium-based contrast agent is administred between two consecutive T_1-weighted scans. Gadolinium has been proven to be a suitable contrast agent in carotid plaques with enhancement in particular in vulnerable plaques, neovascularisation and macrophages [16]. Contrast agent uptake is thought to be due to a defected endothelium, i.e. a leakage in the microvessels in the plaque lesion. As a result the agent accumulates in the tissue's perivascular space [17]. Gadolinium uptake in plaque is associated with a shortening of T_1 and improves visualisation in pre- and post-contrast subtracted images [18, 19].

1.1.2.1 Intracranial vessel wall imaging

Intracranial VWI is of interest in research into cerebrovascular diseases that implicate vessel wall pathology. Certain types of ischemic strokes, e.g., la-

cunar infarcts, can result from blockages of the lenticulostriate arteries near their origins at the middle cerebral artery (MCA) [20, 21]. Clinically established methods, such as CTA/DSA and MR angiography (bright-blood TOF) detect only the lumen of the vessel, and early thickening of the wall is likely to be missed. A major advantage of VWI over these methods is its ability to not only depict the lumen, but the wall with its inner and outer boundary itself. VWI has the potential to detect early pathology and the non-invasive nature of MRI has made VWI a popular method to study wall pathology *in-vivo* [22–25].

The increase in signal-to-noise ratio (SNR) at 7T can be used to improve spatial resolution. High resolution is crucial for intracranial VWI as the wall thickness of the major arteries is on the order of approximately $200\mu m$ [26, 27]. VWI has been used widely at 1.5T and 3T, but methods and protocols have to be adapted for 7T to account for high field challenges, such as the increased specific absorption rate (SAR), transmit B_1-field inhomogeneities and different contrast mechanisms due to changes in T_1- and T_2-relaxation times [28].

1.2 Background

There are three conditions that must be met by an intracranial VWI sequence:

1 **Inner boundary:**
Blood in the lumen (the inner vessel area that is confined by the wall) must be sufficiently suppressed. This is usually referred to as black-blood (BB) imaging.

2 **Outer boundary:**
Cerebrospinal fluid (CSF) outside of the lumen must be sufficiently suppressed.

3 **Wall signal level:**
The vessel wall signal must be sustained at a sufficiently high level to produce inner and outer boundary contrast.

With these three requirements in mind, we will introduce the common concepts and methods used for BB imaging and CSF nulling.

1.2.1 Concepts of black-blood imaging

1.2.1.1 Inversion strategies

BB sequences aim to null the signal of flowing blood. The interest in BB imaging started in the early 90s with the development of the Double-Inversion Recovery (DIR) method [29,30]. A DIR sequence diagram is given in Figure 1.1. This 2D sequence uses a combination of a non-selective and selective 180°-inversion pulse. The non-selective inversion is applied to image the slice at the blood nulling time (TI). The slice-selective pulse re-inverts the magnetisation of static tissue to facilitate high contrast in the imaging slice. This technique has several downsides. First of all it does not suppress CSF. Also, the T_1 of arterial blood is already relatively long and is further increased at 7T to about 2500 ms [31], prolonging TI and thus repetitions times (TRs).

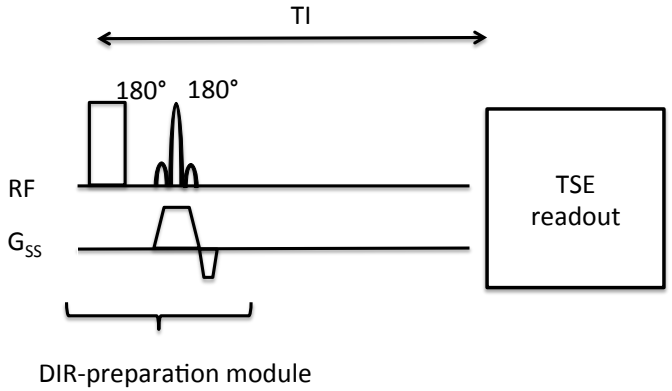


Figure 1.1: Single-slice DIR sequence diagram. A non-selective 180° pulse globally inverts all spins. A slice-selective inversion flips back the magnetisation of static tissue in the imaging slice. The slice is then read out (usually by a turbo-spin echo sequence) at the blood nulling time (TI).

The use of inversion pulses in combination with a turbo-spin echo (TSE) readout further renders a practical 7T protocol implementation problematic due to SAR constraints. Simon et al. used DIR at 7T for imaging lesions in multiple sclerosis and used a TR of 5000 ms [32]. They reported their main challenge to the be the pronounced B_1-inhomogeneity and drop-off towards the neck for typical 7T head coils.

1.2.1.2 Phase spoiling strategies

All other BB techniques are based on phase spoiling effects. This phenomenon can be derived from the first principles of nuclear magnetic resonance. The Larmor frequency ω of a spin isochromat scales linearly with the external magnetic field B

$$\omega(\vec{r}) = \gamma \cdot \underbrace{B(\vec{r})}_{=B_0+\Delta B(\vec{r})} \quad , \tag{1.1}$$

where we already imply that the field, and thus the resonance frequency, varies across space $\vec{r}$. Within a time increment $\mathrm{d}t$, the spin isochromat precesses by an angle $\phi(\vec{r})$

$$\phi(\vec{r}) = \gamma \int B(\vec{r})\,\mathrm{d}t \tag{1.2}$$

$$= \underbrace{\phi_0}_{\gamma \cdot B_0 \cdot t} + \gamma \int \underbrace{\Delta B(\vec{r})}_{\vec{\nabla} B(\vec{r}) \cdot \vec{r}}\,\mathrm{d}t\,. \tag{1.3}$$

The above expression can be rewritten in terms of spatial gradients $G(\vec{r}) = \vec{\nabla} B(\vec{r})$ [1], to relate it to the hardware tools that are used in sequence design (i.e. the gradient system):

$$\phi(\vec{r}) = \underbrace{\phi_0}_{\text{const. phase}} + \underbrace{\gamma \int \vec{G}(t) \cdot \vec{r}(t)\,\mathrm{d}t}_{\text{position-dependent phase}}\,, \tag{1.4}$$

where we further imply that the position $\vec{r}(t)$ of the spin isochromat may change over time. Eq. 1.4 is key to understand all phase spoiling BB strategies.

Diffusion-like

The motion-sensitized driven equilibrium (MSDE) strategy uses a diffusion-like preparation module as displayed in Figure 1.2 [33–35]. An initial 90°-tip into the transverse plane is followed by strong gradients to introduce a phase spoiling effect. A 180° in-plane excitation and the repetition of identical gradients refocuses the dephasing for static spins, but not for spins that have changed their position $\vec{r}$ in the field, i.e. flowing blood spins. A voxel that

[1] Nabla operator: $\vec{\nabla} = \frac{\partial}{\partial x}\hat{e}_x + \frac{\partial}{\partial y}\hat{e}_y + \frac{\partial}{\partial z}\hat{e}_z$

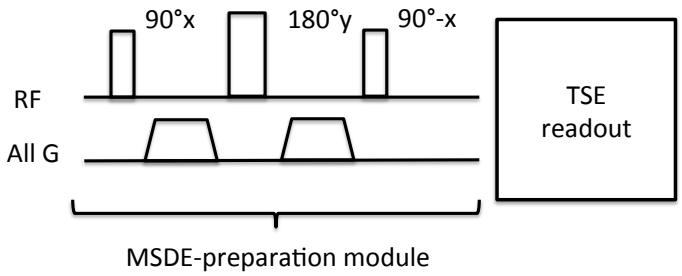


Figure 1.2: MSDE sequence diagram. A 90°-flip into the transverse plane is followed by strong gradients to introduce phase spoiling. The in-plane 180° excitation, followed by the same gradients rephases static spins, but not moving blood spins. A TSE sequence is usually applied for readout.

contains spins flowing at a range of velocities will subsequently contain a range of different phases. This voxel will have a vanishing net magnetisation as the readout signal is the sum of all magnetisation states within the voxel. MSDE preparation overcomes the DIR constraint to wait for long inversion times of arterial blood. However, it would not comply with SAR limits at 7T unless TRs would likely have to be prolonged to the order of two seconds, compared to about one second at 3T. Further rephasing inefficiency is likely to cause unsuccessful gradient moment nulling in static tissue.

Variable flip angles

The energy transmitted scales with the square of the Larmor frequency ω_0 and the square of the transmit amplitude B_1. Thus, in practical terms, SAR scales with the square of the external field strength B_0 and the square of the RF flip angle α [36]

$$SAR \propto \omega_0^2 \cdot B_1^2 \propto B_0^2 \cdot \alpha^2 \,. \tag{1.5}$$

Consequently, lower flip angle sequences are preferred at 7T to counteract the increased SAR burden. Promising schemes are TSE readouts with variable

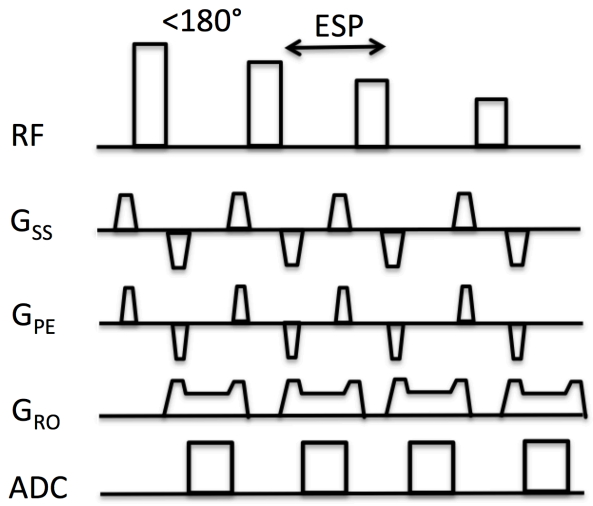


Figure 1.3: Sequence diagram for a slab-selective 3D TSE sequence with variable non-180° flip angles. All RF-pulses are hard pulses, i.e. non-selective. The phase-encoding gradients are the in-plane G_{PE} and the through-slice G_{SS} gradients. The readout gradient G_{RO} is further used for spoiling. Note, that the G_{PE} and G_{SS} overlap the crusher gradients to reduce the inter-echo spacing (ESP) in order to maximise the number of echoes that can be acquired before the signal becomes too small.

flip angles. The classical TSE sequence consist of an initial 90°-flip angle, followed by 180°-refocusing pulses creating T_2 contrast. The TSE with variable flip angles sweeps through a list of non-selective angles that are below 180°. Figure 1.3 displays the sequence diagram. The gradient moment of flowing spins is non-zero for this sequence scheme. Long echo train lengths and intra-voxel velocity profiles produce sufficient phase spoiling for a BB effect [37,38]. The usage of smaller flip angles comes with the advantage of SAR reduction and has basically replaced the classic TSE sequence at 7T for anatomical imaging such as T_2-FLAIR [39, 40]. It further offers interesting strategies to control the magnetisation decay in the transverse plane. This can be used to keep readout signals steady over remarkably long echo trains, reducing blurring and allowing time-efficient 3D acquisitions [41–43]. The common

literature abbreviations for implementations of variable flip angle schemes are General Electric's VISTA (standing for Volumetric ISotropic TSE Acquisition) [44] and Siemens' SPACE (standing for Sampling Perfection with Application optimised Contrast using different flip angle Evolutions) [45].

Higher order phase spoiling

Variable flip angle schemes reduce the SAR load by the use of non-180° flip angles. However, SAR is a "rate", and the transmitted energy is divided by the inter-echo spacing (ESP) or TR and limits apply to periods over ten seconds and 6 minutes. As such, variable flip angle schemes are still prone to SAR problems if high resolution is desired that demands protocols with short ESPs and long echo trains. Another phase spoiling technique that uses very low flip angles is DANTE (standing for Delay Alternating with Nutation for Tailored Excitation). The "Tailored Excitation" in the name already hints that DANTE was originally developed for other purposes. Indeed it was invented for high spectral resolution in MR spectroscopy [46]. DANTE's application to imaging for tracking motion was first described in the early 90s [47] (it was used to put dark lines on the heart to track its motion, also known as SPAMM [48]). The first implementation and validation of DANTE as a BB technique was done by Li et. al [49]. Figure 1.4 shows a sequence diagram for a representative DANTE pulse train when used as a BB module. A train of non-selective pulses of a constant low flip angle is played out with ultra-short inter-pulse times of one to a few milliseconds. The inter-pulse time is filled by strong gradients that introduce the phase spoiling effect for flowing spins. As such, it can also be thought of as an unbalanced steady-state free precession (SSFP) sequence. Balanced SSFP usually shows unwanted flow effects and artefacts that result from the contribution of flowing spins that

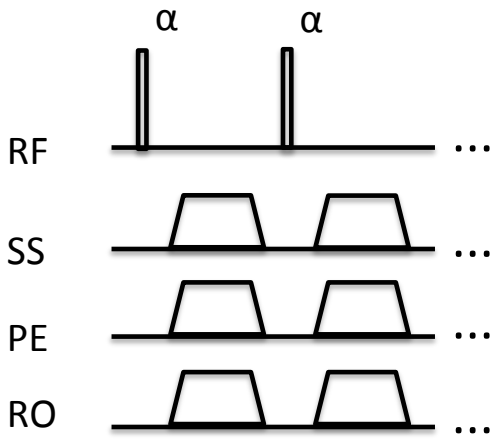


Figure 1.4: A sequence diagram of a DANTE module. A train of low angle hard pulses is followed by strong gradients for phase spoiling.

get excited in-slice but have left the slice at the time of readout [50]. The goal of DANTE is to fully spoil the flowing spins by the application of non-zero gradient moments. For the n-th DANTE RF-pulse a phase increment $\Delta\phi_n$ is accumulated by the spin isochromat. The velocity dependence of the n-th increment can be expressed by Taylor-expanding the position in time ($\vec{r}(t) \approx \vec{r}_0 + \vec{v}t + \mathcal{O}(2)$) in the phase accumulation equation (Eq. 1.4)

$$\Delta\phi_n \approx \gamma \int_{(n-1)\tau}^{n\tau} \vec{G}(t) \cdot (\vec{r}_0 + \vec{v}t)\, \mathrm{d}t \tag{1.6}$$

$$= \underbrace{\gamma \langle \vec{G} \rangle \cdot \vec{r}_0 \tau}_{\text{const. increment}} + \underbrace{\gamma \left(n + \frac{1}{2}\right) \langle \vec{G} \rangle \cdot \vec{v}\tau^2}_{\text{increasing with n and velocity-dependent}} . \tag{1.7}$$

From Eq. 1.6 we infer that a static spin isochromat at $\vec{r}_0$ accumulates constant phase increments and is *phase-coherent*. Moving spin isochromats accumulate a *non-coherent* phase increment that scales with n, and velocity $\vec{v}$, the time-average gradient amplitude $\langle \vec{G} \rangle$ and is further quadraticly dependent on the gradient duration τ. A more detailed discussion of steady-state signal levels and contrast will be provided in the Section 1.4.1.

DANTE has been combined with FLASH (standing for fast-low-angle-shot) readouts to image carotid artery walls [51] and the peripheral femoral artery

[52]. A combination of DANTE and TSE has been used to suppress CSF in spinal cord imaging [53]. Intracranial VWI with DANTE was achieved with a variable flip angle scheme readout recently by Wang et al. at 3T [54]. At that point in time the performance of DANTE at 7T had not been investigated. We started our work on a 3T system (this chapter) with the ultimate aim to optimise a DANTE module for VWI at 7T.

1.2.2 Concepts of CSF suppression

The early BB sequences did not particularly address CSF suppression (this is why they are indeed better referred to as BB imaging rather than VWI). The initial developments focussed on the larger arteries in the neck (vertebral, external and internal carotid arteries) that have no or fast flowing CSF in their vicinity. The resolution/SNR limitations at lower fields ($\leq 1.5T$) put intracranial VWI out of reach.

Intracranial vessels, in particular the arteries of the Circle of Willis, are located outside of the cortex with some segments being closely attached to tissue, but mostly surrounded by CSF. Especially in the elderly population, with onset of atrophy and widening of perivascular spaces, arterial structures are increasingly immersed in CSF. The signal of CSF renders the delineation of the outer wall boundary difficult. Efficient CSF suppression is therefore needed. This is usually achieved with global inversion pulses, imaging at CSF's nulling TI. This is known as Fluid-Attenuated-Inversion Recovery (FLAIR). At 7T tissue and CSF T_1 values are drawn closer together and FLAIR preparations destroy the SNR gain of the higher field. To address the T_1 convergence Visser et al. implemented a clever strategy to separate CSF and grey matter magnetisation time courses with a T_2-magnetisation preparation (T_2-prep) [40]. A module of a 90°-pulse is followed by in-plane

refocusing pulses and a $-90°$-flip back pulse. CSF has a much longer T_2 (close to water) than grey matter and is refocused before being flipped back along the longitudinal axis, whereas grey matter is effectively spoiled. After a subsequent adiabatic inversion pulse CSF undergoes inversion recovery, but grey matter starts with a saturation recovery. The T_2-prep FLAIR has been used with a contrast agent for wall enhancement for intracranial VWI at 7T to study vessel wall pathology in patients with cerebrovascular diseases [55, 56].

1.3 Scope of this work

The ultimate goal was to achieve intracranial VWI at 7T. With the SAR constraints in mind we started this work with a DANTE-prepared FLASH sequence because of the low flip angle nature of both the preparation and readout scheme. Firstly, we implemented DANTE-FLASH on our 3T system for validation purposes. We tested simulated against experimentally measured magnetisations in a static and a flow phantom. *In-vivo* pilot scans were carried out to test the BB effect. The sequence was then transferred to the 7T system for *in-vivo* piloting using our previously validated simulations as a guide for finding optimal scan parameters.

We explain below why our initial goal to use DANTE-FLASH at 7T turned out to be infeasible with the current hardware. Our alternative approach for ultra-high field VWI is then be presented in Chapter 2.

1.4 Implementation of DANTE-FLASH for VWI

1.4.1 DANTE and FLASH signals: Theory

We use the Bloch formalism to draft the mathematical framework of magnetisation evolution during DANTE and FLASH. Concepts are taken from the book by Haacke et. al [57].
Let $\vec{M} = [M_x, M_y, M_z]$ be the magnetisation vector of a spin isochromat, with the initial thermal equilibrium state $\vec{M}_0 = [0, 0, M_0]$.

FLASH

Immediately after the first excitation pulse θ the magnetisation is

$$M_x(0^+) = 0, \qquad M_y(0^+) = M_0 \sin(\theta) \qquad \text{and} \qquad M_z = M_0 \cos(\theta)\,. \quad (1.8)$$

After this perturbation the longitudinal component recovers while the transverse component decays. In matrix formulation this reads

$$\vec{M}(t) = \mathbf{E}(T_1, T_2, t)\mathbf{R_x}(\theta)\vec{M}_0 + (1 - e^{-t/T_1})\vec{M}_0\,, \quad (1.9)$$

with the rotation by θ around the x-axis:

$$\mathbf{R_x}(\theta) = \begin{Bmatrix} 1 & 0 & 0 \\ 0 & \cos(\theta) & \sin(\theta) \\ 0 & -\sin(\theta) & \cos(\theta) \end{Bmatrix} \quad (1.10)$$

and the decay/recovery matrix:

$$\mathbf{E}(T_1, T_2, t) = \begin{Bmatrix} e^{-t/T_2} & 0 & 0 \\ 0 & e^{-t/T_2} & 0 \\ 0 & 0 & e^{-t/T_1} \end{Bmatrix}, \tag{1.11}$$

where T_1 and T_2 are the longitudinal and transverse decay constants. FLASH sequences are usually "spoiled", i.e. the transverse component is brute-force destroyed by a strong gradient before the next θ-excitation. Therefore we do not have to include a precession term in Eq. 1.9. We can write the steady-state $M_{z,ss}$ after n pulses as

$$M_{z,n} = M_{z,n-1}\cos(\theta)E_1 + M_0(1 - E_1)\,, \tag{1.12}$$

where $E_1 = exp(-\mathrm{TR}/T_1)$. With $n \to \infty$ this yields

$$M_{z,ss} = \frac{M_0(1 - E_1)}{1 - E_1\cos(\theta)}\,. \tag{1.13}$$

DANTE

DANTE can be described similarly as above, but as it is not spoiled (unbalanced SSFP), we need to include a precession term (the phase increment from Eq. 1.6). The magnetisation from one DANTE α-pulse to the next reads

$$\vec{M}_n = \underbrace{\mathbf{R_z}(\Delta\phi_n)}_{\text{precession}}\mathbf{E}(T_1, T_2, \tau)\mathbf{R_x}(\alpha)\vec{M}_{n-1} + (1 - e^{-\tau/T_1})\vec{M}_0\,. \tag{1.14}$$

The precession term is key to the BB effect as we discussed earlier, but it is further responsible for a mixed T_1/T_2 contrast in DANTE. Fractions of the

transverse components are rotated back into the longitudinal component by the α-pulses. The DANTE inter-pulse time τ is only one to two milliseconds in duration, but the "recycling" of magnetisation yields a surprisingly high steady-state signal for tissue (a FLASH sequence with such short TR would have a negligible steady-state signal). The derivation of the steady-state in the static case is lengthy and we will only give the result here. The derivation assumes small flip angles α and that the DANTE inter-pulse time τ is much smaller than the tissue T_1 and T_2 values (see Appendix E2 of Li et al. [53])

$$M_{z,ss} = M_0 \left(1 - \frac{\alpha}{2} \sqrt{\frac{T_1}{T_2}} \right) \tag{1.15}$$

Note, that the steady-state solely depends on α, T_1 and T_2. However, τ plays a crucial role and cannot be chosen arbitrarily short for multiple reasons. The phase range over the spatial dimension of the voxel $(\Delta x, \Delta y, \Delta z)$ has to be at least 2π to avoid a banding pattern of signal dropouts across the field of view (FOV)

$$2\pi \leq \gamma \sqrt{(G_x \Delta x)^2 + (G_y \Delta y)^2 + (G_z \Delta z)^2}\, \tau \,. \tag{1.16}$$

Figure 1.5 shows a simulated banding pattern. The magnetisation is incoherent and crushes at equidistant positions. Imaging parameters have to be chosen such that an entire or integer multiples of one band squeezes into the voxel dimensions. Therefore, the gradient amplitude and duration have to be traded off with the spatial resolution to guarantee a non-stripy image. Stronger gradients are favourable but compete with nerve stimulation limits and temporal efficiency.

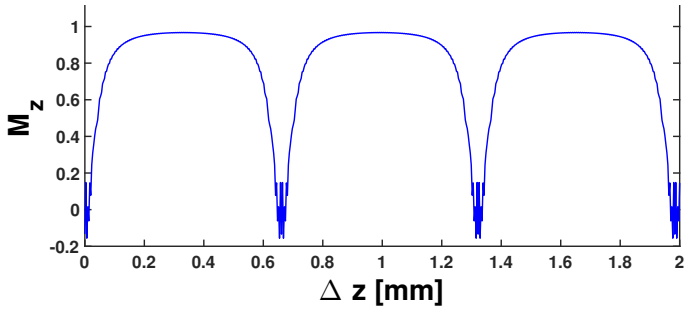


Figure 1.5: Simulation of a typical banding pattern. The longitudinal magnetisation M_z is a function of position and is crushed at equidistant positions in the FOV. Imaging parameters (resolution, gradient duration and amplitude) have to be chosen such that an entire or an integer multiple of the band squeezes into the dimension of the voxel.

1.4.2 Readout order

The parameters of DANTE and FLASH have to be chosen carefully to minimise signal oscillations during the readout. The M_z component undergoes an oscillation into the DANTE steady-state first and then undergoes an oscillation towards the FLASH steady-state. Parameters, such as flip angles and TRs can be chosen such, that the oscillation in M_z is reduced as much as possible to avoid a variation in the readout signal. The effective resolution, or point-spread function (PSF) will be narrower the more stable the signal (recall that the Fourier-transform of a boxcar function is the sinc function). Matching parameters will always be imperfect due to tissue heterogeneity and imperfect flip angles, so it is important to consider a suitable readout scheme to mitigate the effect of blurring. Figure 1.6 provides a sequence diagram. After each DANTE preparation the slice encode direction is read out in centric order, whereas the phase encode direction is stepped through linearly in a loop over the DANTE-FLASH blocks. Signal variations therefore occur in the slice direction and blurring in the axial plane is minimised which we considered to be the most important plane for wall pathology in-

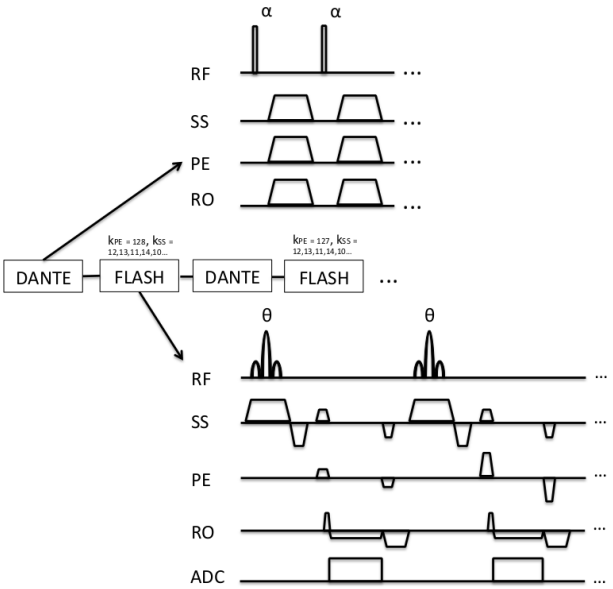


Figure 1.6: Sequence diagram of DANTE-FLASH. The readout scheme in the phase encode direction is linearly ascending, whereas we use a centric scheme in the slice direction. The DANTE module is repeated between every step in the phase encode direction.

spection. It is also more practical to implement the slice encode direction in multiple slabs so that 15-30 lines (comprising one slab) could be read out per DANTE module. With TRs of $10-20$ ms, longer readouts risk the exchange of DANTE-prepared blood with new fresh blood.

1.5 Methods

1.5.1 Simulation and phantom validation at 3T

I implemented a DANTE module in the Siemens IDEA environment. To test this DANTE module on the scanner and to validate our Bloch simulations we conducted phantom scans on a 3T whole body scanner (Siemens Verio, Erlangen, Germany). A four-channel head coil was used to collect the raw k-space data (Siemens so-called "TWIX" files) of the individual coils. To

measure the M_z component as a function of applied DANTE pulses n we combined the DANTE module with a 2D single-slice echo-planar imaging (EPI) free induction decay readout. These experiments were carried out during the early stage of sequence programming so we did not have a full 3D-set of gradients implemented yet. However, this was not a concern here, as we only needed the gradient to be along the direction of flow and could align the flow phantom along one axis. The DANTE module only applied a uni-directional gradient along the slice encode dimension. DANTE-EPI scans were looped over, starting with a DANTE-free volume (M_0 measurement) followed by volumes with increasing DANTE pulses. The TR of the EPI was chosen long enough to allow for a complete recovery until the next volume. Our first attempts to match the simulated and measured signals in the static phantom showed strong deviations, particularly when we used high DANTE flip angles. We attributed this mismatch to B_1 inhomogeneity, i.e. the flip angle we set at the scanner, and subsequently used in the simulation, was actually not achieved. Hence, we decided to additionally construct a B_1 map to correct the flip angles in the simulations. A phantom bottle of unknown content was used as a static specimen. We used spin-echo EPI (SE-EPI) scans to estimate T_2 and additional inversion recovery SE-EPI (IR SE-EPI) scans to estimate T_1. In a second set of experiments we used a flow phantom. This flow phantom consisted of a pump that pumped water through latex tubes at adjustable pump levels. The latex tube had an inner diameter of 4 mm. The pump level that we used here had a mean velocity $\bar{v} = 10\,\mathrm{cm/s}$. We assumed the T_1 and T_2 values to be 3400 ms and 600 ms for bulk water at 3T. Simulations with synchronised parameters were subsequently performed to replicate the experimental data. The Bloch formalism as described in section 1.4.1 was implemented in MATLAB, R2013a (Mathworks, Nattick, USA).

1.5.1.1 MR data

B_1 mapping scans (static and flow phantom)

Two single 2D-EPI scans were acquired with a flip angle $\vartheta_1 = 40°$ and $\vartheta_2 = 2 \cdot \vartheta_1 = 80°$. Base resolution = 64; FOV = 250 mm; slice thickness, Δz = 2.6 mm; bandwidth, BW = 3000 Hz/px; echo time, TE = 21 ms, TR = 5000 ms. The actual flip angle achieved can then be calculated as

$$M_{\perp,\vartheta_1} = M_z \sin(\vartheta_1)\,, \quad M_{\perp,\vartheta_2} = M_z \sin(2\vartheta_1)\,, \tag{1.17}$$

$$\sin(2\vartheta_1) = 2\sin(\vartheta_1)\cos(\vartheta_1)\,, \tag{1.18}$$

$$\Rightarrow \quad \frac{M_{\perp,\vartheta_1}}{M_{\perp,\vartheta_2}} = \frac{M_z \sin(\vartheta_1)}{M_z \cdot 2\sin(\vartheta_1)\cos(\vartheta_2)} = \frac{1}{2\cos(\vartheta_1)} \tag{1.19}$$

$$\Rightarrow \quad \vartheta_1 = \cos^{-1}\left(\frac{M_{\perp,\vartheta_2}}{2M_{\perp,\vartheta_1}}\right). \tag{1.20}$$

$M_\perp$ is the transverse magnetisation that is available for readout and is proportional to the signals S measured in each scan

$$\vartheta_{1,\text{actual}} = \cos^{-1}\left(\frac{S_{\vartheta_2}}{2S_{\vartheta_1}}\right). \tag{1.21}$$

DANTE-EPI in the static phantom

EPI: flip angle $\theta = 90°$, TR = 17840 ms, TE = 24 ms. All other parameters were as in the B_1 mapping scans.

DANTE: $G_z = 20$ mT/m, $\tau = 1$ ms. This produces a phase range of 4π over $\Delta z \approx 2.4$ mm (Eq.1.16) and avoids banding pattern effects as it is an integer multiple of 2π. DANTE pulses were incremented for each TR in steps of 2 to 400. Three different DANTE flip angles of $\alpha = 5°/10°/15°$ were tested.

SE-EPI/IR SE-EPI for T_2/T_1 measurements (static phantom)

SE-EPI for T_2: A series of SE-EPIs was applied with varying TEs = [15, 25, 30, ..., 220] ms and a long TR = 1000 ms. All other parameters were as in the B_1-mapping scans.
IR SE-EPI for T_1: A series of IR SE-EPIs was acquired with varying TIs = [100, 110, 120, ... , 350, 400] ms and a fixed TE= 15 ms. All other parameters were as in the B_1 mapping scans.

DANTE-EPI in the flow phantom

EPI: flip angle $\theta = 90°$, TR = 17840 ms, TE = 24 ms. All other parameters were as in the B_1 mapping scans.
DANTE: $G_z = 20$ mT/m, $\tau = 1$ ms, slice thickness $\Delta z = 2.4$ mm. DANTE pulses were incremented for each TR in steps of 20 to 400. Three different DANTE flip angles of $\alpha = 5°/10°/15°$ were tested.

Post-processing

The SE-EPI and IR SE-EPI data were reconstructed on the scanner and the magnitude images were taken for T_2 and T_1 calculations as outlined below. The DANTE-EPI data was loaded off the scanner in the form of raw k-space data (TWIX). The data were read into MATLAB and TWIX data was further phase-corrected using in-house scripts. The following steps were then performed:

1. The k-space data of the DANTE-EPI scans was Fourier-transformed into image space for each individual coil and the absolute values were calculated and taken as the equivalent to the longitudinal magnetisation M_z.

2. A central voxel was chosen as an ROI in the static phantom. In the flow phantom a voxel in the tube's cross section was selected.

3. The B_1 correction was performed as outlined in Eq.1.21.

4. The T_2 value was calculated from fitting a mono-exponential decay (Bloch equation) to the SE-EPI data. The T_1 in the static phantom was calculated from fitting a mono-exponential recovery (Bloch equation) to the IR SE-EPI data.

5. The simulation of the DANTE-prepared $M_z(n)$ was then performed with the T_1/T_2 values from the fit. DANTE parameters were exactly the same as in the experiment, with B_1-corrected flip angles. To calibrate experimental and simulated data the $M_0 = M_z(0)$ value for the simulation was set to the first (DANTE-free) EPI scan value.

6. For the flow phantom simulation we further assumed a parabolic flow profile across the tube's cross section to model for velocity averaging.

1.5.2 *In-vivo* test at 3T

A full 3D-gradient implementation of the DANTE-FLASH sequence was implemented to test for the intracranial *in-vivo* BB effect at the Circle of Willis. From the preceding simulation validation in phantoms (see Results) we concluded that our simulation scripts model the magnetisation reliably within an acceptable error range. For the *in-vivo* scanning it was crucial to match the DANTE-prepared M_z with the steady-state signal of the FLASH readout. This guarantees minimal variations of M_z over k-space and a sharper point-spread function. However, it should be kept in mind that a perfect matching is impossible, given the heterogeneity of T_1 and T_2 values between

tissues and subjects. This will be even further heterogenous in patient populations where deviating relaxation parameters are implied, in particular in the vessel wall tissue with potential plaque accumulation. We used reported DANTE parameters for carotid artery imaging at 3T as a starting point for the DANTE module [49] and simulated DANTE-FLASH signal evolutions for different DANTE and FLASH flip angles α/θ and TRs. With the simulations as a guide, we tested a set of parameters on the scanner. Here, we only report the final parameters that we found to match best. A 24 years-old subject was scanned under institutional ethical approval on the 3T system using a 32-channel head coil (Siemens, Erlangen, Germany). The sequence was run twice, once without DANTE to get a bright blood TOF reference image.

FLASH: 3 slabs (20% oversampling), resolution = $0.5 \times 0.5 \times 0.5 mm^3$, TR = 21ms, TE = 3.89 ms, $\theta = 18°$, BW = 70 Hz/px. 20 lines of k-space were acquired within each FLASH block.

DANTE: $n = 150$, $\alpha = 12°$, $\vec{G} = [18, 18, 18]$ mT/m, $\tau = 1660$ ms.

1.5.3 *In-vivo* test at 7T

Following the *in-vivo* test at 3T, we transferred the sequence to the 7T whole-body scanner (MAGNETOM 7T, Siemens, Erlangen, Germany). The frequency was increased accordingly. Another important adaptation for the 7T system was the avoidance of the "forbidden" resonance frequencies of the different gradient system. DANTE gradients are driven to their maxima and inter-pulse times τ are on the order of one to a few milliseconds, risking to coincide with the hardware-specific resonance frequencies. The gradient system on the 7T allowed us to increase gradient amplitudes compared to 3T and we decided to maximise the amplitude along an oblique direction with

a maximum the z-component to $G_z = 40$ mT/m as this is a likely dominant direction of blood flow (see the individual gradient vector components in the DANTE protocol below), although this direction will differ at different locations in the vascular tree and also between subjects. To reduce the SAR load we further increased the duration of both DANTE and FLASH excitation pulses. Again, simulations were used as a guide for DANTE and FLASH settings to explore on the scanner. Healthy volunteers were scanned under institutional ethical approval. A 1 channel Tx/32 channel Rx head coil (Nova Medical, Wilmington, MA, USA) was used. The data presented in the Results are representative pilot data and were acquired with the following settings:

DANTE: $n = 100$, $\alpha = 12°$, $\tau = 1750$ ms, DANTE RF-pulse duration $\tau_\alpha = 200$ ms, $\vec{G} = [40, 12, 12]$ mT/m.

FLASH: 2 slabs with 48 slices (25% oversampling), resolution $= 0.44 \times 0.44 \times 0.44\, mm^3$, $FOV_{\text{readout}} = 320$, $FOV_{\text{phase}} = 96\%$, TR $= 9.3$ ms, TE $= 3.56$ ms, $\theta = 12°$, BW $= 220$ Hz/px. 20 lines of k-space were acquired within each FLASH block.

1.6 Results

1.6.1 Simulation and phantom validation at 3T

Static phantom

Results for a representative coil are given in Figure 1.7. As expected we observe a reduction in the steady-state signal level with increasing DANTE flip angles. Errors between simulated and measured data points are more pronounced during the initial oscillation with up to 4% and tend to be below

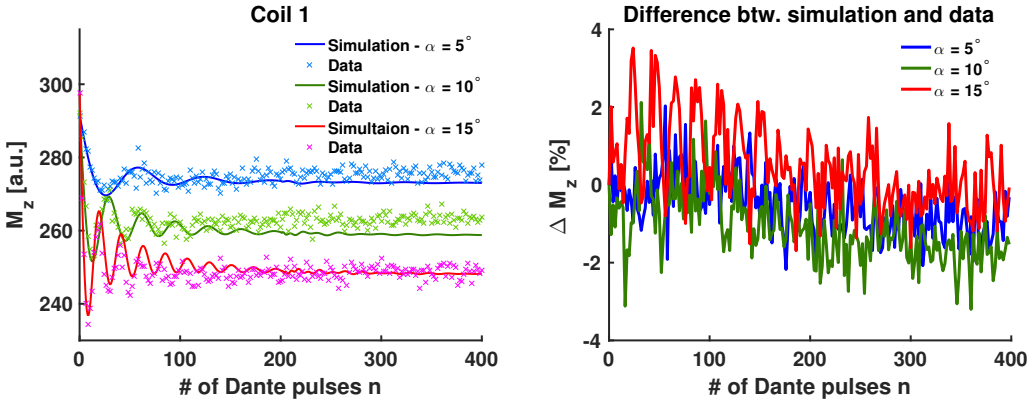


Figure 1.7: Representative coil data in the static phantom. *Left:* Experimental M_z data points are plotted with crosses, simulated data points are drawn in solid lines. *Right:* Difference between the simulated and experimental data.

$1-2\%$ towards the steady state. The deviation between simulated and measured data points is reasonable, given the uncertainty introduced by the measured T_1/T_2 values in the static phantom.

Flow phantom

Results for a representative coil are given in Figure 1.8. The flow crushing effect is enhanced with increasing flip angle and number of applied pulses. Simulation and experimental data is deviating to a larger degree (up to 14%) than in the static phantom measurement. This is most likely due to inaccuracies in the estimate of the tap water T_1/T_2 values and the oversimplified modelling of the flow profile. The water was pumped through the tubes and was rather pulsatile which should add to the intra-voxel dephasing effect.

1.6.2 *In-vivo* test at 3T

A simulation of the expected DANTE-FLASH signal in grey matter for a fixed FLASH readout (constant flip angle θ and TR), but varying DANTE flip angles α is given in Figure 1.9. The aim was to keep the M_z component as

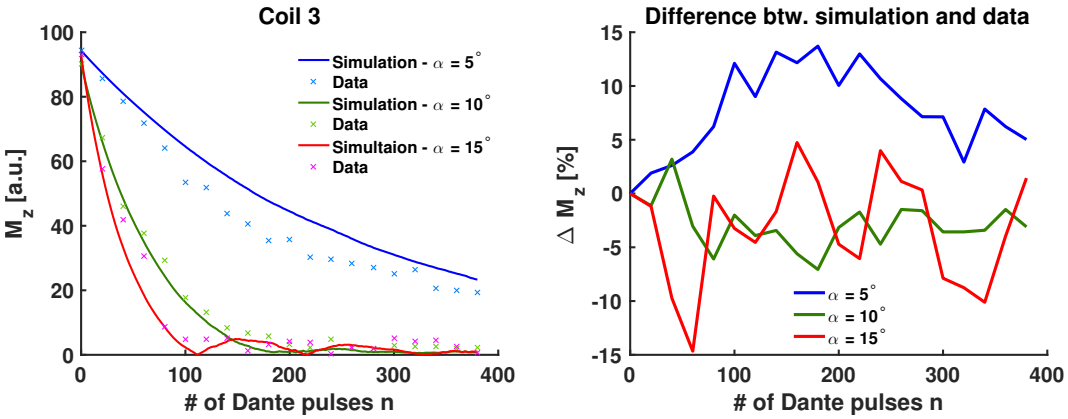


Figure 1.8: Representative coil data in the flow phantom. *Left:* Experimental M_z data points are plotted with crosses, simulated data points are drawn in solid lines. *Right:* Difference between the simulated and experimental data.

stable as possible over the readout. Figure 1.10 shows an example DANTE-FLASH and FLASH image in the region of the Circle of Willis. Bright areas in the FLASH reference (TOF bright blood contrast) show a BB effect on the DANTE-prepared images. The MCA vessel wall is discernible in some sections.

1.6.3 *In-vivo* test at 7T

The BB effect of DANTE-FLASH at 7T turned out to be disappointing. We initially expected an enhanced blood crushing effect at higher field given the prolonged T_1 of arterial blood and stronger gradient system. However, particularly fast flow in the internal carotid artery (ICA), posterior cerebral artery (PCA) and MCA was not suppressed successfully. Figure 1.11 shows a representative pilot scan in the region of the Circle of Willis. Comparing the DANTE-FLASH and TOF control scan it becomes clear that fast-flowing areas are not sufficiently suppressed. The DANTE preparation hard pulses act globally, but in contrast to the whole-body excitation at 3T, they are only transmitted via the head coil, which is known to have a rapid B_1 drop-off

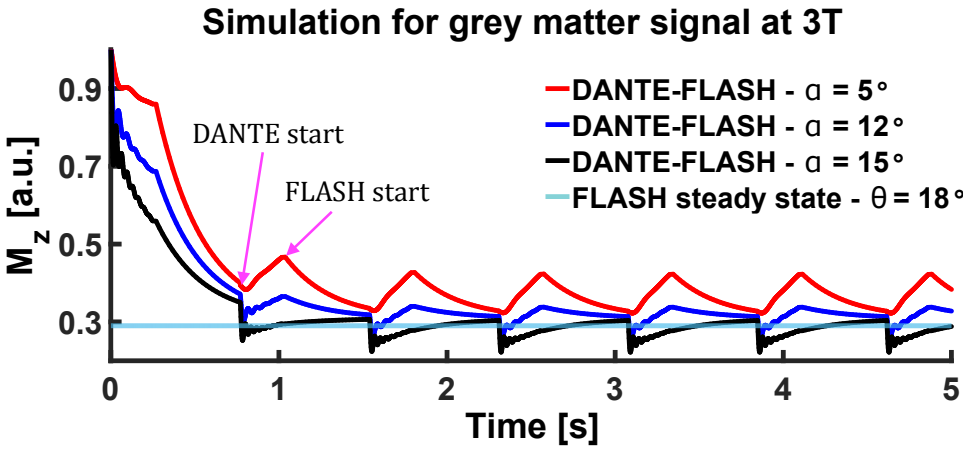


Figure 1.9: Simulation of the DANTE-FLASH signal in grey matter at 3T. The FLASH readout angle θ is kept constant and the DANTE flip angle α is varied. The aim was to keep the readout signal as stable as possible to reduce blurring.

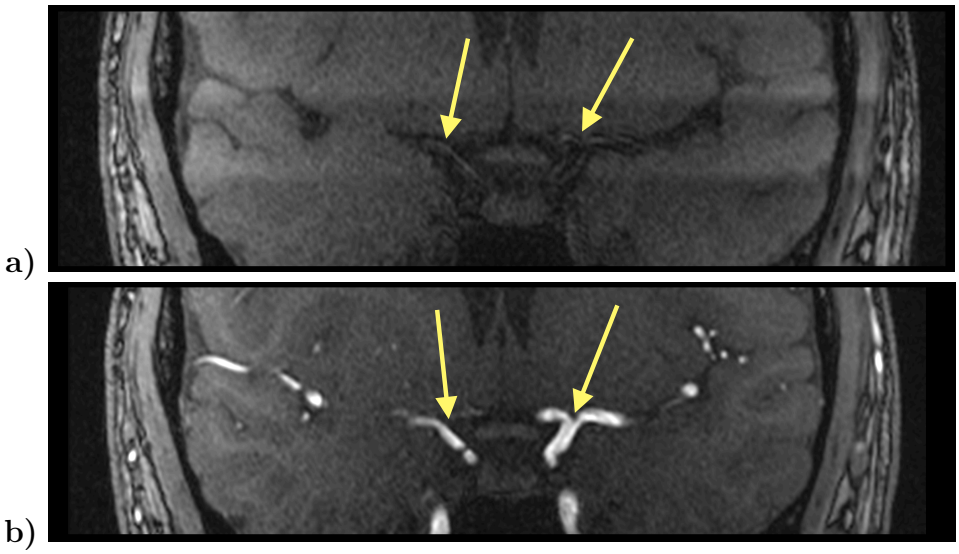


Figure 1.10: DANTE-FLASH (a) and FLASH (b) images in the region of the Circle of Willis. The right and left branches of the M1 segment are marked with yellow arrows. The DANTE-FLASH images show a BB effect in the larger vessels.

towards the neck. The slower flowing spins spend more time in the RF-field and are therefore sufficiently tilted into the transverse plane for the gradient to crush them. The RF-field was a fundamental issue and increasing the DANTE flip angle did not result in a better BB effect in the larger arteries.

1.7 Discussion

Summary of key findings.

- A DANTE module was successfully implemented at 3T and 7T.
- Bloch simulations were validated to accurately predict DANTE signals.
- The excitation efficiency for fast moving spins is too low to produce a BB effect in the large vessels of the Circle of Willis with the current RF-hardware available at 7T.
- DANTE sufficiently suppresses slowly moving spins at 7T.

1.7.1 Simulation and phantom validation

The static phantom experiments validated our simulation of the DANTE signal for stationary spin isochromats. We judged the errors of $0-4\%$ to be acceptable given the inaccuracies introduced by the measured T_1/T_2 values, the B_1 inhomogeneity and the imperfect slice profile. The mismatch between simulated and experimental data in the flow phantom was higher, with error levels of up to 14% during the initial oscillation into the DANTE steady-state. Deviations reduced to below 5% towards the final steady-state, which

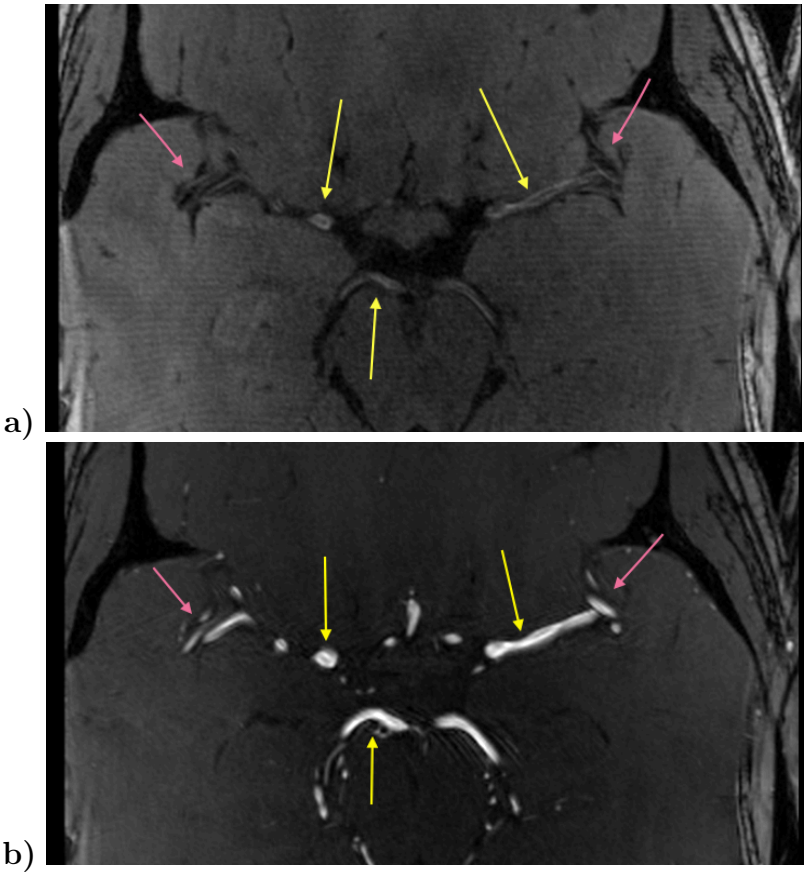


Figure 1.11: DANTE-FLASH (a) and FLASH (b) images in the region of the Circle of Willis at 7T. The yellow arrows mark vessel segments with fast flow that is not sufficiently suppressed in the DANTE-FLASH scan. This particularly affects the ICA, PCA and MCA segments. The pink arrows mark slower flow in higher arterial branches with a better BB effect. It is also worth noting, that the DANTE-prepared image in (a) shows a subtle banding pattern along the anterior-posterior direction, indicating that the attempt to disguise the inherent banding sensitivity of DANTE has not been fully successful. This is likely due to the voxel size not being a perfect integer multiple of the banding periodicity.

is the crucial state that we are aiming to simulate. The same inaccuracies as above hold and additional imprecision was introduced by the velocity profile of the pulsatile flow pump. In summary, we were confident that our DANTE simulations were able to correctly simulate the magnetisation state in static tissue and in flowing blood.

Magnetisation-transfer effects

Our DANTE signal simulations neglect any M_z reduction from magnetisation transfer (MT) effects. The repeated RF pulses of the DANTE preparation lead in theory to a saturation of the macromolecular spins in tissue, resulting in a magnetisation exchange process between the macromolecular pool and the longitudinal magnetisation of the mobile water pool - the MT effect [58]. The significance of the MT effect depends on the imaging sequence, particularly the RF pulse (amplitude and frequency offset) and it is not straightforward to make an estimation of the MT effect in DANTE. Bieri and Scheffler [59] evaluated the MT effect in balanced SSFP. DANTE is an unbalanced SSFP type, but we assume that the gradients will not impact this RF-induced phenomenon. For a TR of 3.5 ms they found a doped agar phantom (mimicking white matter) to have a negligible MT effect for flip angles below 15°. This study was conducted at 1.5T and MT effects decrease at higher field strengths [60]. However, we are using inter-pulse times half of what has been tested in the reference. Nonetheless we assume that our work was not compromised by MT effects, a conclusion supported by the results in Figure 1.7 a), where the simulated M_z component is clearly not overestimating the experimental data.

1.7.2 *In-vivo* experience: 3T vs. 7T

The DANTE-FLASH simulations were used as a guide to set up a parameter space to explore for *in-vivo* pilot scans at 3T. A BB effect was observed in the intracranial vessels and the MCA vessel wall was discernible. After successful implementation of the sequence code at 3T we transferred it to 7T and repeated the parameter search and piloting. However, we found a disappointing crushing effect at 7T in the case of fast-flowing blood spins in the ICA, PCA and MCA. In contrast, slower flowing spins further up the arterial tree showed a good BB effect even at 7T. We concluded that the lack of the whole-body excitation, in combination with the B_1 drop-off towards the neck, renders sufficient preparation of fast blood spins infeasible.

1.8 Conclusion

The major arteries of the Circle of Willis are the vessels that are of highest interest for clinical research into intracranial vessel wall pathology. As mentioned in the introduction a successful VWI sequence has to produce inner wall contrast, i.e. fully null the blood lumen signal. Our experimental experience with DANTE-preparation using the Nova coil at 7T we found an unsatisfactory suppression of blood spins in the MCA. This is due to the fast velocites of blood spins from the heart to the Circle of Willis. The blood crushing effect requires multiple RF-exciations. Given the poor coverage down the neck of the Nova coil the fast spins do not experience enough DANTE exciations to be crushed. An additional neck-coil could be used to

increase the preparation time of fast spins. However, due to SAR limitations it might be necessary to concentrate the DANTE preparation pulses onto the neck coil only in the early phase of preparation. A neck coil was not available (mainly due to safety concerns) at that point in time. Similar issues have been encountered by other research groups who are working towards the 7T-implementation of sequences that excite lower brain and neck areas. For example, arterial spin labelling has to battle the B_1 drop-off and the pronounced off-resonance effects that cause ill-defined slab excitations and low labelling efficiencies [61–63].

Due to the above limitations it was felt that an alternative to DANTE-FLASH had to be found. It was concluded that another readout or preparation scheme would need to be put in place to produce a BB effect. Our initial DANTE-FLASH experience at 7T demonstrated DANTE's ability to sufficiently suppress slow flow. As such, it could be capable of suppressing slowly moving CSF spins to produce outer wall contrast. The next chapter describes attempts to combine DANTE with a different readout strategy.

Chapter 2

T_2-weighted intracranial VWI at 7T using a DANTE-prepared variable flip angle TSE readout (DANTE-SPACE)

This chapter is based on the publication "T_2-weighted intracranial vessel wall imaging at 7 Tesla using a DANTE-prepared variable flip angle turbo-spin echo readout (DANTE-SPACE)" [64].

2.1 Introduction

Variable flip angle sequences were initially developed to reduce SAR and blurring at higher field and have effectively replaced the classic 180°- TSE readout at 7T [40, 65]. Another feature of non-selective variable flip angle schemes is their BB effect that has already been discussed in the previous chapter. The flip angle scheme calculation requires knowledge of the tissue

relaxation times T_1 and T_2. The vendor-implemented scheme is not optimal for vessel wall tissue T_1 and T_2 at 7T. Here we sought to optimise a variable flip angle sequence (Sampling Perfection with Application optimised Contrast using different Flip Angle Evolution – SPACE [45]) to produce a sharp depiction of the vessel wall. Albeit effectively suppressing fast flowing blood spins, SPACE has a limited effect on slowly flowing CSF spins in the vicinity of the MCA. To accomplish the latter, we use the DANTE module, that we found to be sensitive to slow velocities in the previous chapter. Recently, a combination of DANTE and variable flip angle TSE has been used by Wang et al. [54] and Xie et al. [52] to improve VWI at 3T.

2.1.1 Scope of this work

SPACE was optimised for VWI at 7T for sharp wall depiction and high boundary contrast. DANTE was optimised to further enhance CSF suppression. In a PSF analysis study of healthy volunteers we assessed wall conspicuity of the vendor-provided default and our optimised SPACE sequence. On the basis of the three criteria for successful VWI introduced in the previous chapter (section 1.2) we measured the SNR of the three compartments in the MCA: vessel wall, CSF and lumen for both DANTE-SPACE and SPACE sequences and additionally calculated the CNR and signal ratio (SR) between these compartments. An exemplar MCA stenosis patient was scanned with DANTE-SPACE.

2.2 Methods

Figure 2.1 shows the DANTE-SPACE sequence diagram. Note that we marked three time variables in this diagram: $\tau_{\mathrm{RF,D}}, \tau_{G,D}$ and τ_D in the

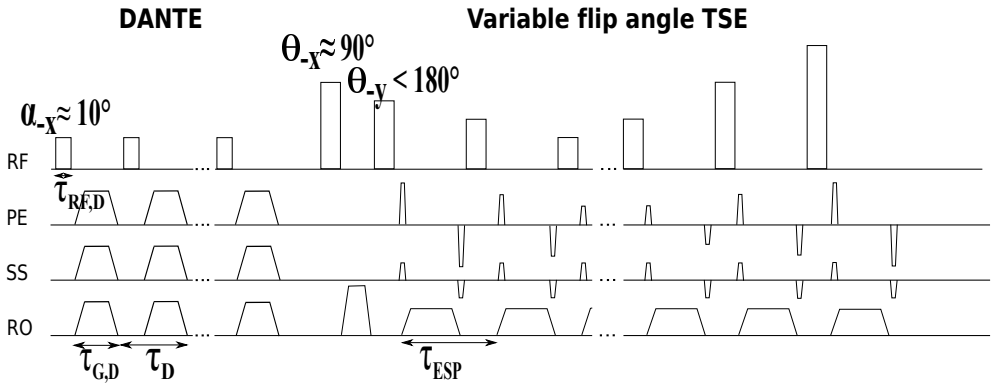


Figure 2.1: Sequence diagram of DANTE-SPACE. A DANTE module is followed by a variable flip angle TSE of refocusing flip angles $< 180°$.

DANTE module. In the previous chapter we only used the inter-pulse time τ as the duration of the DANTE α-pulse and the gradient rise times were negligible compared to the overall inter-pulse time. However, in the 7T implementation DANTE α-pulses had to be prolonged to $\tau_{\mathrm{RF,D}} = 200\,\mu$s due to SAR constraints and the gradient is effectively dephasing over a significantly shorter time period $\tau_{G,D}$.

2.2.1 SPACE optimisation

The magnetisation transfer function (MTF; not to be confused with the magnetisation transfer effect from the previous chapter's Discussion) is the transverse magnetisation over the course of the readout. The MTF of a spin-echo train is more distorted at higher field and leads to image blurring due to the faster T_2-decay. Flip angle sweeps, calculated with a Bloch formalism, are used to counteract this effect [41, 66]. The goal is to find a scheme with a flat MTF over the central part of k-space, assuming some default relaxation times T_1 and T_2. All simulation/optimisation procedures described below were conducted in `C++` and MATLAB. Original `C++` code was kindly provided to us by John Mugler (University of Virginia). A detailed descrip-

tion of the `C++` and `.h` files, and how they were adapted, is provided in the appendix under "How to run variable flip angle simulations".

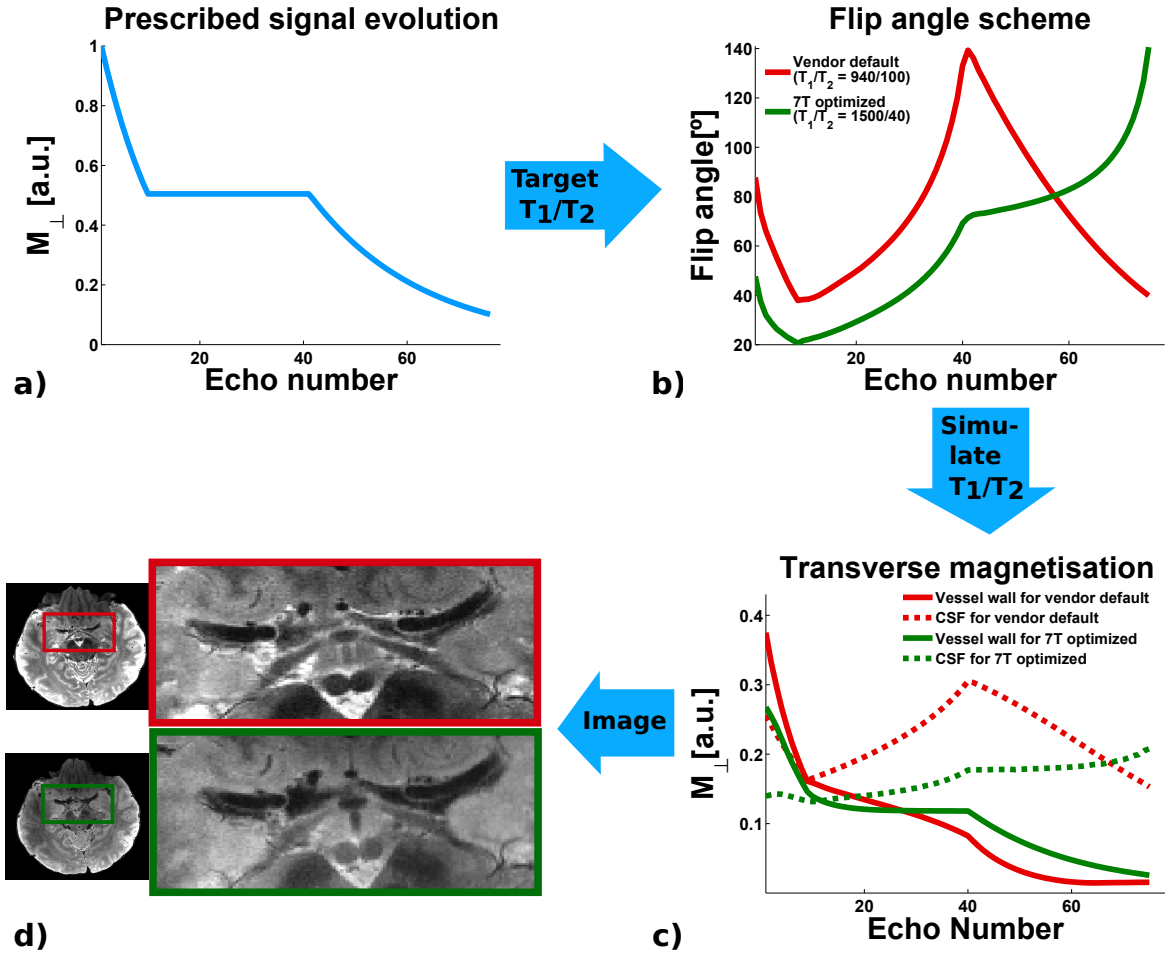


Figure 2.2: Schematic overview of the SPACE optimisation. **a)** Prescribed signal evolution of the transverse component $M_\perp$. The signal is kept constant over the central part of the readout (central part of k-space for a T_2-weighted linear ascending readout scheme). **b)** The algorithm calculates the flip angles that produce the closest match to the prescribed signal for a given combination of T_1 and T_2 values. Red line: Flip angle scheme for the vendor-implemented values of $T_1 = 940$ ms and $T_2 = 100$ ms. Green line: Flip angle scheme for vessel wall $T_1 = 1500$ ms and $T_2 = 40$ ms at 7T. **c)** MTF for vessel wall (solid lines) and CSF (dotted lines), simulated for both flip angle schemes (red for default, green for optimised). **d)** Zoom of the MCA region for the same subject scanned with DANTE-SPACE using the default scheme (red frame) and the optimised scheme (green frame).

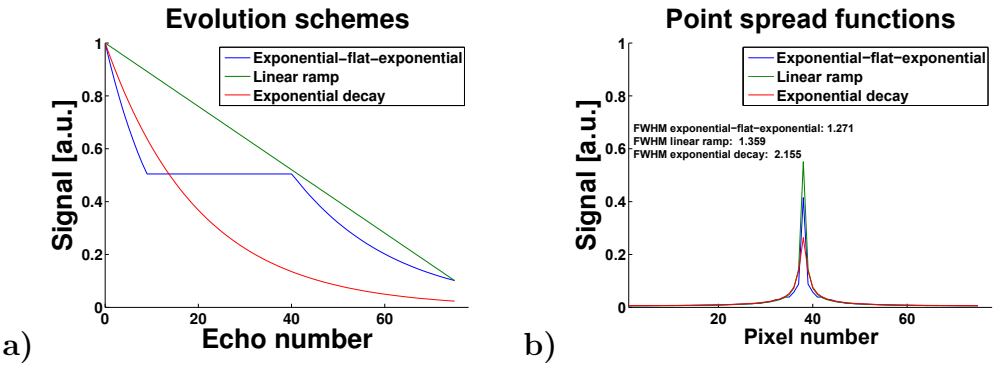


Figure 2.3: Comparison of different evolution schemes (a) and the resulting PSF (b). The FWHMs are plotted in the figure. The PSF for the exponential-flat-exponentail scheme is narrower than the linear ramp and the mono-exponential decay.

Figure 2.2a shows the principal steps of the optimisation. The starting point is the vendor-provided prescribed signal evolution for T_2-weighted TSEs. This evolution is a combination of an initial mono-exponential decay (with a time constant of 17.5 ms and a duration of 11.9 ms per 100 ms of total echo train length (ETL)), a constant part and a final mono-exponential decay (with a time constant of 29 ms and a duration of 46.5 ms per 100 ms ETL). The Fourier transform of the evolution scheme is the PSF along the phase encode direction. The full width at half maximum (FWHM) of the PSF was calculated as an indicator of the theoretical effective resolution achievable with that scheme. We compared the exponential-flat-exponential scheme with the other obvious schemes of a linear ramp and a mono-exponential evolution. The three schemes are shown in Figure 2.3a and the resulting PSFs in Figure 2.3b. The full-width at half maximum (FWHM) of the exponential-flat-exponential scheme's PSF is almost half of the FWHM of the mono-exponential evolution's PSF (1.271 vs. 2.155 pixels) and slightly narrower than the linear ramp's PSF FWHM (1.359 pixels).

To achieve a flat MTF the flip angles need to be calculated that best

match the evolution (Figure 2.2b) for the T_1 and T_2 values encountered by vessel wall at 7T. The calculated scheme can then be used to simulate the MTF for any tissue of interest, in our case vessel wall and CSF (Figure 2.2c). The relative amplitudes of the MTFs indicate the contrast between static CSF and vessel wall. Since 7T measurements of intracranial vessel wall values of T_1 and T_2 were not available in the literature, we estimated their values from carotid artery wall measurements at 3T, multiplying by scaling factors for white matter differences between 3T and 7T [67]. We used factors of 1.45 [31] and 0.67 [68] for T_1 and T_2 respectively. Measured T_1 values of carotid arterial wall at 3T are about 1000 ms [69] and T_2 about 54 ms [70], resulting in T_1 and T_2 estimates of 1500 ms and 40 ms at 7T[1]. This contrasted with the vendor-implemented T_1 of 940 ms and T_2 of 100 ms. A flip angle scheme was therefore calculated for the estimated relaxation times. The FWHM of the simulated vessel wall PSF was then calculated as an indicator of achievable image resolution for the vendor-implemented scheme and the new scheme. It is to note, that T_1 and T_2 values are likely to change in patient populations where vessel wall pathology is implicated. Ultimately, a study of vessel wall T_1 and T_2 values in a suitable patient population would be needed to test how much their relaxation times differ and potentially a slightly different flip angle scheme should be applied.

2.2.2 DANTE optimisation

The goal of the DANTE optimisation is to maximise the contrast between the outer wall and the surrounding CSF, i.e. the difference in the longitudinal

[1]Note that a 7T-study by Koning et al. [71] published after our own study had commenced has reported carotid vessel wall $T_1 = 1628 \pm 13$ms and $T_2 = 46 \pm 4$ms, in agreement with our estimates within the standard deviation.

magnetisations, M_z, weighted by their spin densities ρ_0

$$|\Delta M_{z,VW/CSF}| = \rho_{0,VW} \cdot M_{z,VW} - \rho_{0,CSF} \cdot |M_{z,CSF}| \,. \tag{2.1}$$

The absolute value of the CSF signal is considered in Eq. 2.1 since oscillations into the steady-state can lead to a negative undershoot of $M_{z,CSF}$ for a certain range of pulse numbers, whereas the MR image itself displays only the magnitude. The same equation applies to the inner wall and lumen contrast $\Delta M_{z,VW/Blood}$. Contrast between moving and static spin isochromats in DANTE arises from the velocity-induced phase spoiling effect that builds up with an increasing number of pulses. This was derived in the previous chapter in detail (see Eq. 1.6). The major uncertainty in simulations is the CSF velocity in the MCA vicinity. The predominant pattern for CSF velocity fluctuations is sinusoidal with the cardiac cycle. The highest amplitudes have been measured to be in the range of 3-5 cm/s in dynamic flow regions such as the cerebral aqueduct [72, 73]. In many other areas, such as the subarachnoid space, CSF is almost static and the DANTE-spoiling effect is expected to be negligible. Larger gradient amplitudes lead to a more efficient phase spoiling, although peripheral nerve stimulation imposes an upper limit. Decreasing the slew rate at the cost of longer gradient durations $\tau_{G,D}$ is not a viable option. Longer $\tau_{G,D}$ would require a longer DANTE preparation module to achieve the same contrast level as with shorter inter-pulse times as it is the number of RF-excitation that are experienced by the flowing spins that determine the crushing effect, see Wang et al. for a detailed simulation study [54].

2.2.2.1 Simulations

We simulated the magnetisation of vessel wall, dynamic CSF and blood voxels using the Bloch formalism validated in the previous chapter. Simulations were run for a flip angle range of $\alpha = 7° - 12°$ and up to $n = 700$ pulses. Besides exploring the range of suitable parameters, this flip angle range further addresses the increased B_1 variations at 7T. A CSF or blood voxel consists of multiple spin isochromats of different velocities. This velocity dispersion was taken into account by averaging over a range of velocities. A CSF voxel was modelled to have velocities of 2 cm/s ±2.5% in the z-direction and 0.5 cm/s ±2.5% in the other directions. The blood velocities were set to 20 cm/s ±2.5% in the z-direction as measured in the carotid artery [74]. All further simulation parameters were chosen to match the optimal sequence parameters achievable by the scanner and that were in accordance with nerve stimulation limits. We chose the maximum gradient amplitude along the head≫feet direction as this is the major direction of CSF and blood flow: head≫feet ($H \gg F$), $G_{H \gg F} = 40$ mT/m; anterior≫posterior ($A \gg P$); $G_{A \gg P} = 28$ mT/m, Right≫Left ($R \gg L$); $G_{R \gg L} = 20$ mT/m. An inter-pulse time τ_D of 1.6 ms was used, which is at the limit of the scanner's mechanical resonance response ("forbidden" frequencies). Other parameters were $T_{1,CSF}/T_{2,CSF} = 4019/311$ms (average values from [31, 75]), $T_{1,blood}/T_{2,blood} = 2290/100$ms (for arterial blood [76]) and a voxel size of $0.5 \times 0.5 \times 1mm^3$. Vessel wall relaxation times were set to $T_{1,VW}/T_{2,VW} = 1500/40$ ms, as explained above. To calculate the contrasts $|\Delta M_{z,VW/CSF}|$ and $|\Delta M_{z,VW/Blood}|$ from Eq. 2.1, we used a normalised CSF and blood spin density of $\rho_{CSF} = 1$ and $\rho_{blood} = 0.89$ and assumed a vessel wall spin density of $\rho_{VW} = 0.72$ (which is the average of grey and white matter spin densities relative to CSF [57]).

2.2.2.2 Signal loss due to brain movement

A common simplification in DANTE simulations of tissue is the assumption of perfectly static conditions. However, brain movement, due to physiologically-induced motion with the respiratory and cardiac cycle, is a known phenomenon and causes signficant signal loss in diffusion and perfusion imaging [77]. Similarly, it could cause an unwanted DANTE signal loss in tissue. We investigated the level of signal loss in static brain tissue caused by the DANTE module beyond the expected value. We anticipated potential signal loss in the region of the brainstem, which is known to move particularly with the cardiac cycle, and lies close to the MCA. Brain movement with the cardiac cycle is anisotropic and peak amplitudes of $1.5-2$mm/s in a caudally-anterior direction have been measured in the brainstem [78]. When single directional gradients along the principal axes are applied, i.e. $\vec{G} = G \cdot \hat{e}_i$, the velocity-induced phase term in Eq. 1.6 will solely depend on the velocity amplitude along that direction, i.e. $G \cdot v_i$. If DANTE preparation causes additional signal loss in tissue due to anisotropic brain movement, the image intensity should vary between DANTE scans that are run with different single directional gradients. Indeed, the observations above would predict that a DANTE scan acquired with a gradient along the H$\gg$F direction leads to more signal dropout in the brainstem compared to a DANTE scan acquired with a gradient along the R$\gg$L direction.

We used DANTE preparations with the gradient aligned along each of the three principal axes in turn: $\vec{G}_{H\gg F}$, $\vec{G}_{A\gg P}$ and $\vec{G}_{R\gg L}$. We acquired data in four healthy volunteers and in a pork phantom. The pork phantom served as a truly rigid tissue control for validation. Each subject underwent a total of four scans, consisting of the three single-directional DANTE-SPACE scans and a SPACE scan with DANTE switched off for normalisation.

2.2.3 MR data

The scans were acquired on a 7T whole-body scanner (MAGNETOM 7T, Siemens, Erlangen, Germany) using a 1 channel Tx/32 channel Rx head coil (Nova Medical, Wilmington, MA, USA) and under institutional ethical approval.

2.2.3.1 Vessel wall conspicuity: SPACE optimisation

A SPACE scan with the vendor-implemented scheme and the optimised scheme were acquired in four subjects (mean age = 32) for a comparison of wall depiction. DANTE was applied for these scans to reduce the CSF signal as much as possible to enhance vessel wall conspicuity for line profile measurements (see Section 2.2.4 below). The following settings apply:
DANTE: flip angle $\alpha = 10°$, number of pulses $n = 300$, inter-pulse duration $\tau_D = 1.6$ ms, gradient duration $\tau_{G,d} = 1.4$ ms.
SPACE: resolution $= 0.5 \times 0.5 \times 1 mm^3$, $\text{FOV}_{read} = 240$ mm, $\text{FOV}_{phase} = 75\%$, 176 slices, TR = 2620 ms, equivalent echo time $\text{TE}_{eq} = 165$ ms, ESP = 4.6 ms, ETL = 345 ms, GRAPPA acceleration factor = 4 in the phase-encode direction, turbo factor = 39, slice turbo factor= 2, echo trains per slice = 3, BW = 465 Hz/px. The total scan time was about 11 minutes per scan.

2.2.3.2 Vessel wall boundary contrast: DANTE-SPACE vs. SPACE

To test the effect of DANTE, we ran the 7T-optimised SPACE sequence with and without DANTE in 11 healthy volunteers (age range 25-64 years, mean age = 35 years). The same settings as listed above apply.

For SNR measurements (see Section 2.2.4 below) we had to calculate the

spatially varying noise amplification due to the GRAPPA acceleration used in the sequences. For this purpose we acquired a fully-sampled GRE scan with and without RF-pulses (62 seconds duration each) in four subjects. The RF-free scan is a pure noise scan and does not yield any signal. The same FOV as in the DANTE-SPACE and SPACE scans was used. The raw k-space data were analysed off-line.

2.2.3.3 Signal loss due to brain movement

DANTE: Parameters were the same as for the DANTE preparation described above, with the exception that the gradients were only switched on along a single axis at the maximum amplitude of 40 mT/m.
SPACE: resolution= $1 \times 1 \times 1mm^3$, FOV_{read} = 220 mm, FOV_{phase} = 75%, base resolution = 258, 176 slices, TR = 3980 ms, equivalent TE_{eq} = 198 ms, ESP = 3.4 ms, ETL = 401 ms, GRAPPA acceleration factor = 4 in the phase-encode direction, BW = 592 Hz/px.

2.2.4 Post-processing and image analysis

2.2.4.1 Image analysis of vessel wall conspicuity: SPACE optimisation

Intensity line profiles across the MCA wall were positioned parallel to the phase-encode direction (here, R≫L) in locations where the wall was aligned perpendicularly and was not touching surrounding tissue (Figure 2.4). To increase the number of profiles that meet both conditions we further included profiles across the basilar artery. Across all four subjects a total of 24 profiles were identified. The profile maximum was assigned the PSF centre. Two pixels to each side from the centre (Figure 2.4b) were included in the fitting

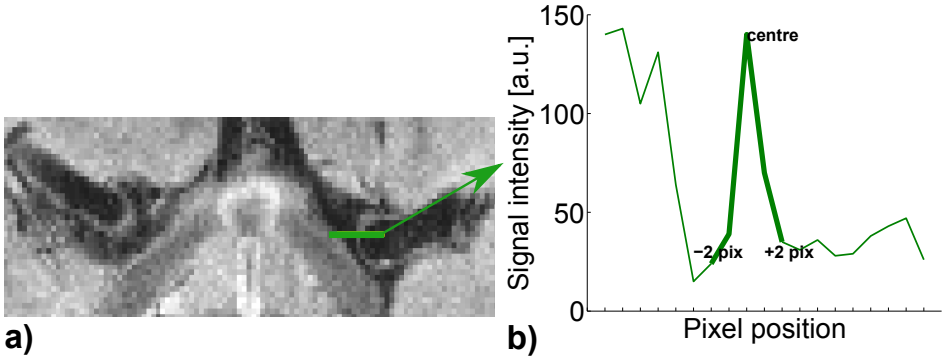


Figure 2.4: An examplar intensity line profile. The profile (green line) is positioned parallel to the phase-encode (here, R≫L) direction in a location where the wall is perpendicular to that direction. The corresponding intensity profile is plotted in b). The values used for the Gaussian fit are highlighted in bold.

of a Gaussian profile. The FWHM was calculated from the fitted parameters. The PSF centre values were further used to compare the vessel wall signal ratio of the optimised to non-optimised SPACE scheme. To compare the signal ratio of CSF between both schemes we measured four CSF ROIs (two in the ventricles and two in the subarachnoid spaces) in each subject. All analysis was carried out in MATLAB, R2013a (Mathworks, Nattick, USA).

2.2.4.2 Image analysis of vessel wall boundary contrast: DANTE-SPACE vs. SPACE

SNR measurements

GRAPPA acceleration is known to amplify noise over the FOV. This amplification is not uniform due to the non-uniform FOV coverage of the coil sensitivity profiles that are used in the reconstruction. So called g-factor maps quantify this spatial amplification variation. As such, the standard strategy to quantify SNR via the ratio of the signal in the tissue ROI to the signal standard deviation in an alias-free extracranial noise ROI cannot be

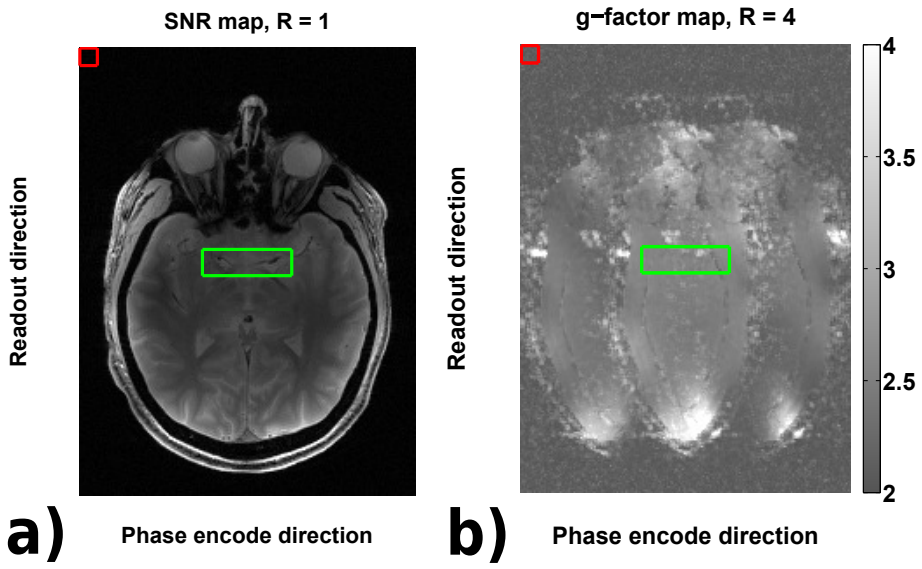


Figure 2.5: **a)** Non-accelerated SNR map with the MCA (green box) and a noise area (red box). **b)** g-factor map for parallel acceleration in the phase-encode direction of a factor 4. The ratio of the mean g-factors within the ROIs is used to scale thermal noise in the parallel-accelerated DANTE-SPACE and SPACE scans.

applied. To account for the spatially varying noise amplification we defined a new SNR measure, that factors in local g-factor variations

$$\mathrm{SNR}_{\mathrm{tissue}} = \frac{S_{\mathrm{tissue}}}{G \cdot \sigma_{\mathrm{noise}}}, \tag{2.2}$$

where S_{tissue} is the signal in the tissue ROI and σ_{noise} is the standard deviation in a noise ROI in a ghost-free area outside of the brain and

$$G = \frac{g_{\mathrm{tissue\ ROI}}}{g_{\mathrm{noise\ ROI}}} \tag{2.3}$$

is the ratio of the g-factors in the noise and tissue ROIs. Thermal noise cannot be measured reliably in tissue areas themselves, but multiplying σ_{noise} by G accounts for the amplified noise in the tissue region, here the MCA area. To calculate the g-factor maps, SNR maps were simulated in MATLAB

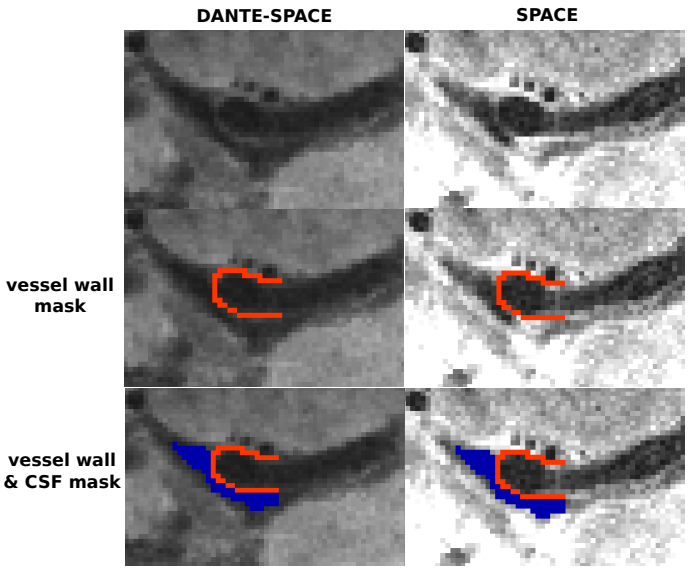


Figure 2.6: Location of the signal masks. The vessel wall mask (red) and CSF mask (blue) were drawn first on the DANTE-SPACE scan (left column) and then applied to the registered SPACE scan (right column).

with the "pseudo multiple replica" method by Robson et al. [79], using code that was kindly provided to us by the authors. This method uses the non-accelerated RF-free k-space data to derive the noise covariance matrix to account for spatial correlations and scaling. Corrected artificial noise is then added to the k-space data to form multiple replicas of the true data that only vary by noise. Images are reconstructed for each replica. For each pixel the magnitude in the true reconstruction is then divided by the standard deviation over all replica reconstructions to yield the SNR map. For each subject a region over multiple slices that contained the MCA was identified on the non-accelerated SNR map and transferred to the g-factor map to calculate the local $g_{\text{tissue ROI}}$. A noise area was selected in the upper right corner of the FOV to yield $g_{\text{noise ROI}}$. Example SNR and g-factor maps are provided in Figure 2.5 showing the areas that were used to calculate G. An average G value was calculated from the four subjects and applied to all subsequent analyses.

CNR measurements

To assess the ability of DANTE-SPACE to improve outer wall contrast we measured the CNR between wall and surrounding CSF, defined as

$$\mathrm{CNR}_{VW/CSF} = \mathrm{SNR}_{VW} - \mathrm{SNR}_{CSF}\,. \tag{2.4}$$

$\mathrm{CNR}_{VW/Lumen}$ between wall and lumen was measured similarly.

SR measurements

Additionally we calculated the signal ratios between wall and CSF as

$$\mathrm{SR}_{VW/CSF} = S_{VW}/S_{CSF}\,, \tag{2.5}$$

$\mathrm{SR}_{VW/Lumen}$ between wall and lumen was calculated similarly.

For all three measurement (SNR, CNR and SR) we drew two ROIs on each side of the MCA within each subject (total of four ROIs per subject) using FSLview (part of FSL). We used the DANTE-SPACE rather than the SPACE scan since it was more difficult to distinguish between wall, tissue and CSF signal on the latter due to the higher CSF signal. The DANTE-SPACE scan was registered linearly to the SPACE scan within each subject using the FSL tool FLIRT [80]. We checked that registration was successful for every subject to avoid any bias when transforming the ROI masks. It is to note, that this registration could introduce smoothing from the interpolation and subsequent signal reduction. In hindsight a halfway registration between both scans would have been a more accurate form of post-processing. Figure 2.6 shows an example of the ROI selection process. A Student's paired-sample

t-test was used for statistical analysis.

2.2.4.3 Image analysis of signal loss due to brain movement

To ensure that the signal is evaluated in equivalent regions across the subjects all datasets were non-linearly registered to the standard space MNI (Montral Neurological Institute) T_1-template using FSL FNIRT [81]. Three ROIs were defined: one in the brainstem and one in the grey/white matter tissue proximal to the MCA in each hemisphere. The signal loss in each ROI was defined as the mean voxel signal ratio $\langle S_{\text{DANTE-SPACE}}/S_{\text{SPACE}}\rangle$, which was calculated for each of the three single directional DANTE gradient scans. The values were then averaged over all four subjects. The ROI in the pork phantom was drawn manually in a central part of the tissue.

2.2.5 Patient scan

To test the ability of DANTE-SPACE to depict pathology, we scanned a 31 years-old female patient diagnosed with a lacunar infarct in the right hemisphere and stenosis in the right MCA M1 segment. This patient was scanned under the study "The Role of Atherosclerosis in Lacunar Stroke – A 7T MRI study" (REC reference 13/LO/0205). We ran a T_1-MPRAGE sequence in that subject to visualise blood flow and a DANTE-SPACE scan for VWI (settings as described above). The T_1-MPRAGE settings were: - resolution = $0.8 \times 0.8 \times 0.8$ mm^3, FOV_{read} = 256 mm, $\text{FOV}_{\text{phase}}$ = 100%, 256 slices, TR = 2200 ms, TE = 2.9 ms, TI= 1050 ms, flip angle $\theta = 7°$, GRAPPA acceleration factor = 2, BW = 240 Hz/px, ESP = 7.2 ms. The scan time was 7 minutes.

Method	Default scheme	Optimised scheme
FWHM of PSF derived from Bloch simulations [pixels]	1.73	1.29
FWHM $\pm\sigma$ from Gaussian fit to vessel wall line profiles [pixels]	3.28 ± 0.51	2.61 ± 0.36

Table 2.1: Results of the FWHM estimates of the vessel wall PSF for the default and optimised flip angle schemes. The first row is the theoretical estimate derived from the FWHM of the Fourier transform of the vessel wall signal evolution from the Bloch simulations. The second row is the experimentally measured FWHM of 24 line profiles drawn on the vessel wall in four subjects.

2.3 Results

2.3.1 SPACE optimisation

Figure 2.2a shows the prescribed MTF used for the flip angle calculation. Figure 2.2b plots the flip angle schemes that arise from the default implementation (red) and the calculation based on vessel wall relaxation times (green). As an appreciated by-product, the new scheme reduces the overall flip angle amplitudes (red vs. green lines in Figure 2.2b) and therefore SAR, allowing for shorter TR and scan time. The MTFs of the schemes are plotted in Figure 2.2c for vessel wall (solid lines) and CSF (dotted lines). Note that Figure 2.2c shows the predicted signal of static CSF, with no motion-induced effects taken into account, which will suppress the CSF signal further. The FWHM of the theoretically derived vessel wall PSF and the FWHM of the experimentally measured line profiles are displayed in Table 2.1. The theoretical FWHM of the default implementation is 1.73 pixels versus 1.29 pixels for the optimised implementation, predicting an improvement in vessel wall resolution of 25%. The experimentally measured FWHM reduction was 17%. Example images with (green) and without (red) optimisation are shown in

Figure 2.2d. The MTF simulations predict a reduction of the CSF $M_{\perp}$-component (dotted red versus dotted green line in Figure 2.2c), whereas the vessel wall $M_{\perp}$-component is almost unchanged (solid red versus solid green line). From the ROI measurements we found a CSF signal reduction of 38% from default to optimised scheme, but also a reduction of vessel wall signal of 33% which is not expected from the MTF simulations.

2.3.2 DANTE optimisation

Figure 2.7a shows the simulated approach to steady-state of the $M_{z,\mathrm{VW}}$ component as a function of increasing flip angle and number of DANTE pulses. Figures 2.7b and 2.7d show the predicted spoiling of $M_{z,\mathrm{CSF}}$ and $M_{z,\mathrm{blood}}$. The achievable crushing effect scales with flip angle, with almost complete spoiling for 10° and 150 pulses, whereas this level is only reached with 500 pulses when the flip angle is 7°, suggesting a significant variation with actual flip angle and B_1 inhomogeneity. Figures 2.7c and 2.7e show the resulting contrast between wall and CSF, and between wall and blood, respectively. Contrast is predicted to peak earlier for higher flip angles, but with an overall lower steady-state compared to smaller flip angles. Empirically on the scanner we found an insufficient CSF signal crushing effect for a short pulse train and a high flip angle of 12°, and had to increase the number of pulses to 300 with a flip angle of 10°, suggesting B_1 inhomogeneities and a flip angle drop-off towards the neck. A lower flip angle with more preparation pulses is preferred over a larger flip angle with fewer pulses as the latter will decrease the tissue steady-state signal in regions where B_1 is accurate.

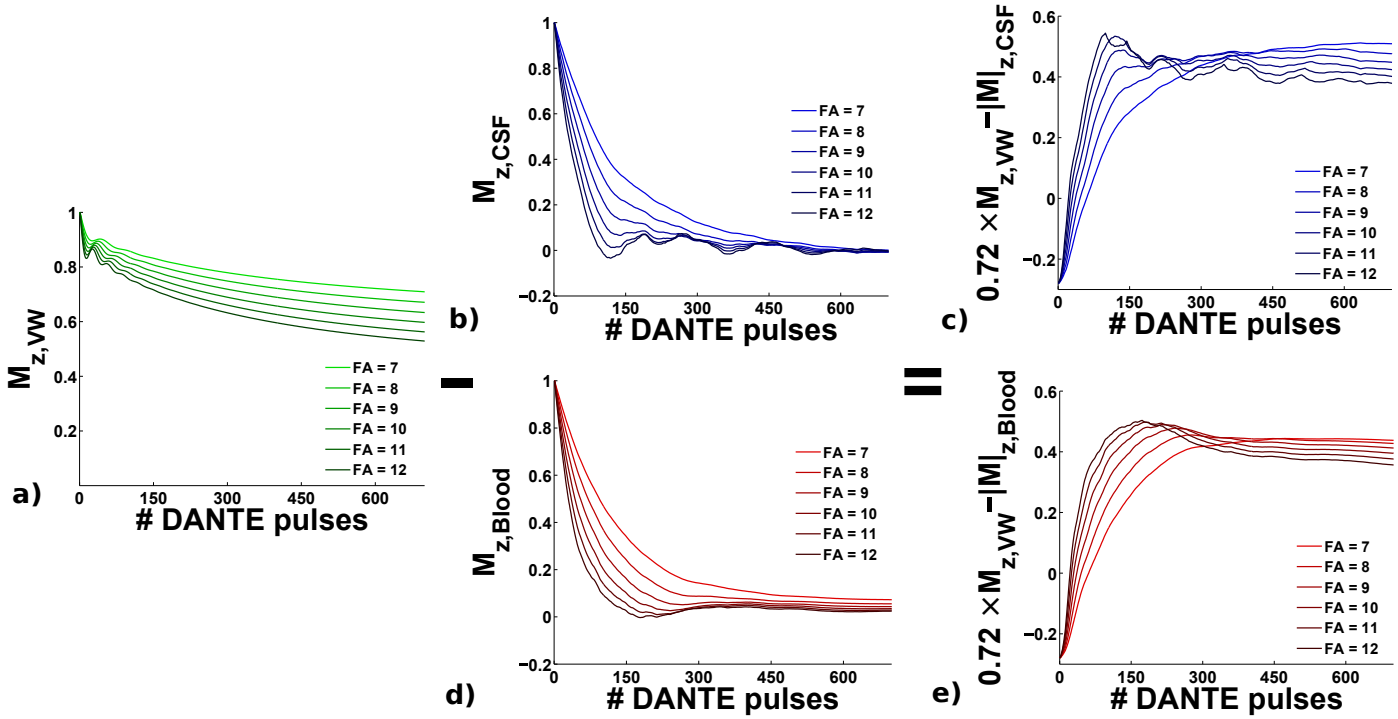


Figure 2.7: Simulation results of the M_z component of vessel wall, flowing CSF and arterial blood for an increasing number of DANTE pulses. Although the DANTE module was optimised for the contrast between vessel wall and CSF, we also included the signal behaviour of blood here. The Results are plotted for a range of flip angles from $\alpha = 7°$ (light colour) to 12° (dark colour). **a)** DANTE steady-state approach for vessel wall tissue. **b)** Signal crushing effect of DANTE for a CSF voxel. **c)** Resulting contrast between vessel wall and CSF. **d)** Signal crushing effect of DANTE for a blood voxel. **e)** Resulting contrast between vessel wall and blood.

2.3.3 DANTE-SPACE vs. SPACE

The g-factor measurements gave a mean scaling factor G of 1.27 with a standard deviation of 0.05 ($< 4\%$) between subjects. The results of the SNR, CNR and SR measurements are given in Table 2.2 (in two subjects we could only identify one ROI on the right side as the MCA wall was adjacent to the cortex and not surrounded by CSF, yielding a total of 42 ROIs). $\mathrm{SNR_{VW}}$ drops by almost a factor of two for the DANTE preparation. However, as the decrease of $\mathrm{SNR_{CSF}}$ is larger, there is an improvement in outer wall boundary contrast $\mathrm{CNR_{VW/CSF}}$ for DANTE-SPACE compared to SPACE. This improvement was significant ($p = 0.0159$) in the right hemisphere, but not in the left ($p = 0.09$). Generally, values vary strongly, with stronger variations for the SPACE scans without DANTE. The $\mathrm{CNR_{VW/CSF}}$ variations occur within and across subjects. 32 out of the 42 ROIs ($\approx 76\%$) have positive $\mathrm{CNR_{VW/CSF}}$ on the SPACE scans which increases to 40 ROIs ($\approx 95\%$) with positive contrast on DANTE-SPACE scans. $\mathrm{SNR_{Lumen}}$ in the lumen area decreases on DANTE-SPACE scans, but the reduction is not statistically significant ($p = 0.089$ for right and $p = 0.055$ for left). In combination with the $\mathrm{SNR_{VW}}$ reduction this leads to a decrease of inner wall boundary contrast $\mathrm{CNR_{VW/Lumen}}$. $\mathrm{SR_{VW/CSF}}$ increases significantly for the DANTE-prepared scans in both hemispheres ($p < 10^{-4}$ for right and $p < 10^{-5}$ for left). $\mathrm{SR_{VW/Lumen}}$ decreases significantly for DANTE-SPACE, again because of the decrease in vessel wall signal. Example DANTE-SPACE and SPACE images are given in Figure 2.8 for a 64 year-old healthy subject.

	Compartment		**DANTE**	**No DANTE**	**p-value**
SNR $\pm\sigma$	Vessel wall	right	44.53 ± 21.60	74.20 ± 49.71	$< 10^{-5}$
		left	41.54 ± 16.55	82.82 ± 53.81	$< 10^{-6}$
	CSF	right	31.74 ± 18.56	68.38 ± 53.46	$< 10^{-3}$
		left	29.23 ± 15.75	77.09 ± 65.80	$< 10^{-3}$
	Lumen	right	16.53 ± 5.90	18.77 ± 9.72	0.089
		left	17.93 ± 6.61	21.25 ± 12.10	0.055
SR $\pm\sigma$	Vessel wall vs. CSF	right	1.47 ± 0.28	1.22 ± 0.25	$< 10^{-4}$
		left	1.44 ± 0.37	1.18 ± 0.35	$< 10^{-5}$
	Vessel wall vs. lumen	right	2.62 ± 0.45	3.9 ± 1.06	$< 10^{-6}$
		left	2.32 ± 0.32	3.93 ± 0.87	$< 10^{-8}$
CNR $\pm\sigma$	Vessel wall vs. CSF	right	12.79 ± 8.81	5.81 ± 11.56	0.0159
		left	12.31 ± 6.43	5.72 ± 20.03	0.09
	Vessel wall vs. lumen	right	27.99 ± 16.30	55.42 ± 41.77	$< 10^{-3}$
		left	23.61 ± 10.76	61.56 ± 43.25	$< 10^{-4}$

Table 2.2: Results of the SNR, SR and CNR calculations between vessel wall, CSF and lumen for a total of 42 ROIs from 11 subjects (four ROIs per subject, for two subjects only three ROIs could be defined). Mean values and standard deviations are listed for the DANTE-SPACE and the SPACE scan. The p-values correspond to paired t-tests.

	$\langle S_{\textbf{DANTE-SPACE}}/S_{\textbf{SPACE}}\rangle \pm \sigma$		
	$G_{R\gg L} = 40\text{mT/m}\cdot\hat{e}_x$	$G_{A\gg P} = 40\text{mT/m}\cdot\hat{e}_y$	$G_{H\gg F} = 40\text{mT/m}\cdot\hat{e}_z$
brainstem	0.63 ± 0.02	0.64 ± 0.05	0.47 ± 0.07
close to right MCA	0.75 ± 0.03	0.71 ± 0.04	0.69 ± 0.02
close to left MCA	0.72 ± 0.02	0.67 ± 0.01	0.64 ± 0.05
tatic pork phantom	0.65	0.67	0.65

Table 2.3: Results of the brain motion-induced signal loss measurements using single directional DANTE gradients. The numbers are the mean signal intensity ratios ($\pm$ standard deviation) between the acquisitions with and without applied DANTE gradient. Signal loss varies for different DANTE directions when measured in the human brains, but is directionally independent for the rigid pork phantom.

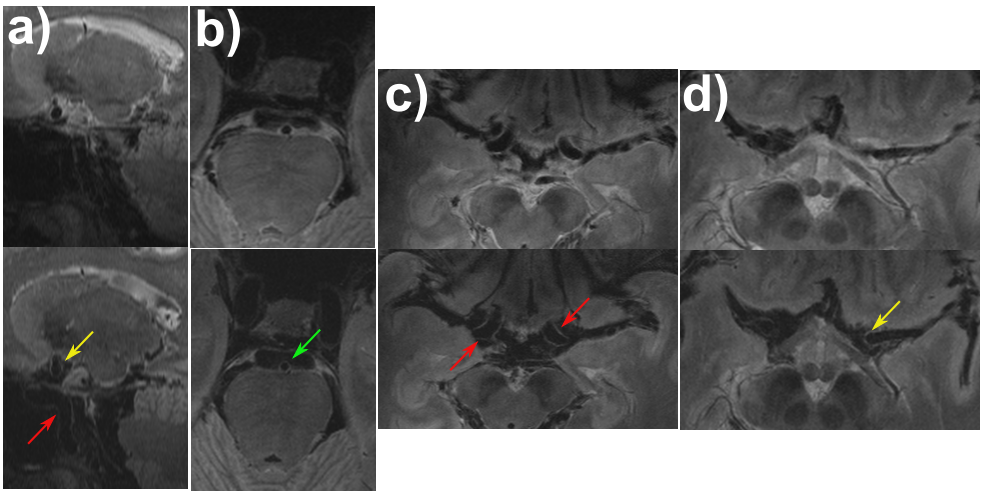


Figure 2.8: SPACE (top row) and DANTE-SPACE (bottom row) scans of a 64-years-old male subject with no known neuro-pathological condition. Both scans are shown at the same signal and window levels. **a)** Coronal view of the ICA (red arrow) and the cross section of the MCA (yellow arrow). **b)** Sagittal view of the brainstem with the basilar artery (green arrow). **c)** Sagittal view of the ICA (red arrows) at the level where they split into the posterior cerebral artery and the MCA. **d)** M1 segments of the right and left MCA (yellow arrows).

2.3.3.1 Signal loss due to brain movement

Results showing the effect of DANTE on static tissue are shown in Table 2.3. The pork phantom measurement confirms that there is no significant difference in signal reduction for different gradient directions in the case of truly static tissue. However, in the brainstem ROI we measured an additional reduction along the H≫F direction of 25% compared to the other two directions. The A≫P and R≫L directions do not differ significantly. In ROIs proximal to the MCA the signal ratios in the left hemisphere are lower for all ROIs compared to their right counterpart. Again, the H≫F direction generates a higher signal loss than the other directions with a maximum of 11% compared to the R≫L direction. The results suggest that there is additional signal loss in tissue close to the MCA region due to brain movement

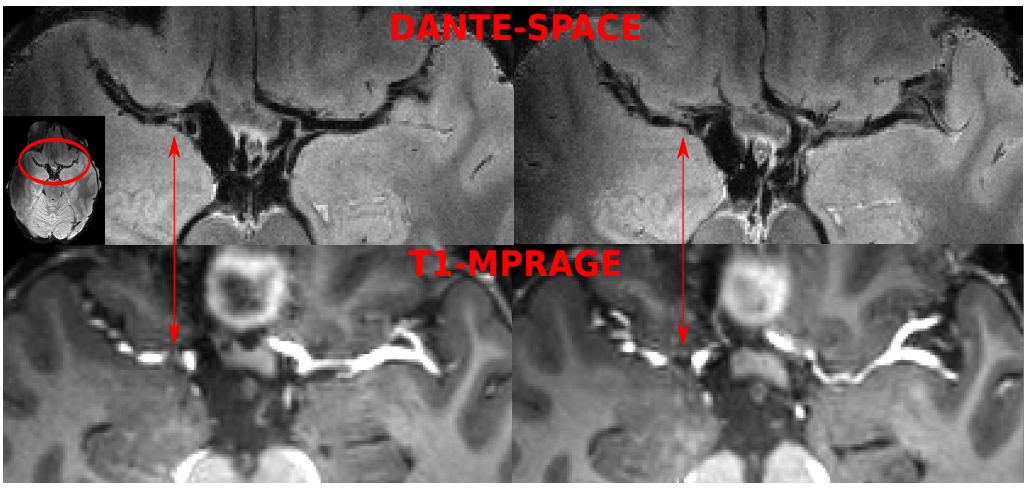


Figure 2.9: Two example images in a lacunar stroke patient with stenosis in the right M1 segment. The red arrows indicate the side of stenosis on the DANTE-SPACE vessel wall scans (top row) and the T1-MPRAGE bright-blood scans (bottom row).

during DANTE-SPACE, with a worst-case loss of 13% in the H≫F direction in the left hemisphere compared to the R≫L direction. However, this finding cannot be applied to the MCA vessel wall directly as there is additional pulsatility. This further underlines that DANTE induces unwanted signal reduction if there is sufficient movement in the direction of the DANTE gradients. Brain movement is thought to support the pumping of CSF through the ventricular system, hence CSF flow and brain movement are likely to be along similar directions, making the choice of an optimal DANTE gradient problematic.

2.3.4 Patient scan

Figure 2.9 shows two slices from the exemplar stenosis patient. The regions of hindered blood flow, visible on the bright-blood T_1-MPRAGE scan, coincide with the vessel wall structure on the DANTE-SPACE scan (red arrows). There appears to be vessel wall signal on the DANTE-SPACE scan where the

signal appears absent on the bright blood T1-MPRAGE. This might indicate a restriction in blood flow (on the T1-MPRAGE) due to either occlusion of the wall by plaque or the collapse of the wall structure itself.

2.4 Discussion and conclusion

Summary of key findings.

- The optimised SPACE readout produces a sharper vessel wall depiction and reduces SAR at 7T.
- DANTE-SPACE doubles contrast between wall and CSF compared to SPACE only, which comes with the trade-off of lower wall to lumen contrast that can be tolerated given that this contrast is generally higher than the contrast to the outer boundary.
- Signal level and contrast show a strong inter- and intra-subject variability. This is likely due to variations in CSF dynamics between subjects, but also between different regions within the subject itself. The sequence's strong sensitivity to motion, which will further reduce signals in pulsatile regions, e.g. close to the brain stem further adds to this variability, which is a general weakness of velocity-induced contrast techniques such as DANTE-SPACE over methods that use inversion to create contrast.

2.4.1 Vessel wall conspicuity: SPACE optimisation

The proposed optimised variable flip angle scheme produced a sharper vessel wall PSF, reduced CSF signal and reduced SAR compared to the vendor-

provided implementation. The improvement in vessel wall PSF was theoretically predicted to be 25% and experimentally a narrowing of the FWHM of 17% was measured. However, the measured FWHM was approximately double the theoretical prediction: 2.88 vs. 1.29 pixels and 3.38 vs. 1.73 pixels, for optimised and default schemes, respectively. This is likely due to inaccuracies in the measurement and fitting of the line profiles. We cannot assume that the wall was a point-like structure along the profile. As the wall structure is assumed to be smaller than the image resolution, CSF and blood at the boundary produce a partial volume effect. These factors further explain the PSF broadening and are likely to produce the vessel wall signal reduction that is observed in the measurement but is not predicted by the MTF simulation that assumes pure vessel wall tissue.

2.4.2 Vessel wall boundary contrast: DANTE-SPACE vs. SPACE

To further reduce the CSF signal for outer wall contrast enhancement a DANTE preparation was applied. There was a mismatch between optimal DANTE parameters derived from the simulations and the experimental findings. One explanation is the inhomogeneous B_1-field, that leads to the flip angles chosen in the protocol likely not being achieved in the lower brain regions due to the poorer excitation profile towards the neck for 7T head coils. A large variation in $\mathrm{SNR_{CSF}}$ and $\mathrm{CNR_{VW/CSF}}$ was found across and within subjects and is likely due to variations in CSF dynamics. $\mathrm{CNR_{VW/CSF}}$ measurements showed an improvement for DANTE-SPACE versus SPACE in the MCA, but this was only statistically significant in the right hemisphere. Generally, $\mathrm{CNR_{VW/CSF}}$ values were found to be lower in the left hemisphere, likely to be caused by the asymmetric right-left excitation profile, which has

been observed by other groups that use the Nova coil at 7T. Specifically for T_2-SPACE acquisitions Eggenschweiler et al. reported reduced contrast in the left hemisphere [82] using the same coil at 7T. Parallel transmit approaches to mitigate local B_1 variations may help to address this issue in the future [83]. The signal ratio between wall and CSF is increased and contrast is doubled in DANTE-SPACE, enhancing outer wall boundary contrast. This comes with the trade off of reduced inner boundary contrast, which is halved, but still at a high level of approximately 25. Sufficient signal ratio between both boundaries is crucial for plaque assessment.

The major limitation of our study is the resolution ($0.5 \times 0.5 \times 1mm^3$). The MCA wall thickness is assumed to be in the range of 0.2 mm for healthy subjects. In line with the vessel wall PSF measurements we found a larger $\mathrm{SNR_{VW}}$ drop than expected from the simulations and the same partial volume effect argument holds. However, increasing the resolution is not straightforward, due to scan time, DANTE banding patterns and SAR. Nevertheless, wall thickening with age could make DANTE-SPACE the preferred VWI sequence over SPACE. The images of the stenosis patient show the potential of DANTE-SPACE to depict vessel wall architecture and pathology. However, ultimately a study with a larger number of patients with pathology would be needed. A recent review of the literature on VWI [55] lists only magnetisation-prepared inversion recovery-TSE (MPIR-TSE) [40] as an alternative sequence for VWI *in-vivo* at 7T. That sequence has an acquisition time of 11-12 minutes, comparable to our protocol. The MPIR-TSE sequence has been used with a lower, but isotropic resolution of $0.8 \times 0.8 \times 0.8mm^3$. We chose a conservatively long TR to guarantee SAR compliance for every head geometry and to keep the imaging protocol consistent (SAR ranged between subjects from 66% to 98% of the maximum allowed limit). In a

clinical setting the TR could be adjusted individually to reduce scan time. Here, we only present T_2-weighted images and future work should address the implementation of multi-contrast DANTE-SPACE at 7T. Other possible improvements could be an increase in resolution, trading off the size of the imaging slab, similar to Qiao et al. [44] who presented high resolution VWI of up to 0.4 mm at 3T with the VISTA sequence.

Chapter 3

Low- and cardiac-frequency fluctuations in ultra-fast rs-fMRI data

3.1 Background

Resting-state fMRI (rs-fMRI) is the recording of fMRI signals in the absence of any task, and subjects are usually only instructed to stay awake [84]. Throughout the last decade BOLD (standing for blood-oxygen level dependent) fMRI has been used extensively to study rs-activity in humans. This led to the establishment of rs-network analysis. These are sets of functionally connected brain regions with temporally correlating BOLD signals and an underlying structural connectivity [85–87]. For this analysis the BOLD signal is ideally of a pure neuro-vascular origin. However, in reality additional signals ranging from hardware influence [88] to subject-induced thermal [89] and physiological noise can cause spatio-temporal correlations in the fMRI timecourses [90]. Usually these signals are regarded as confounds and many

research over the last decade has focused on the removal of this "noise" [91]. In the following subsection we will go through the various contributions to the BOLD fMRI signal in detail.

3.1.1 The rs-fMRI spectrum

A discussion of contributions to the BOLD signal is more approachable in the frequency domain instead of the time domain. Different phenomena contribute to the spectrum in different frequency bands. Figure 3.1 shows a schematic overview of the most prominent contributors to an EPI power spectrum. The neurovascular-driven haemodynamic response and slow vasomotor fluctuations constitute the very low band below 0.1 Hz. Respiration can overlap into the very low frequencies, but dominates between 0.1 and 0.3 Hz. Cardiac fluctuations in healthy subjects occur around 1 Hz. The entire spectrum has a baseline due to frequency-independent Gaussian thermal noise.

3.1.1.1 Sampling speed and aliasing

The spectral width of the acquired data is defined by the sampling speed, i.e. the repetition time (TR). Before discussing the spectral composition it is essential to understand the effect of TR on the data. In the previous decade standard protocols were restricted to TRs on the order of one to three seconds. Cardiac and (in part) respiratory fluctuations occur at rates that are too fast to be temporally resolved by such sampling rates. If sampled too slowly these components alias into lower frequency bands or the zero component. The *Nyquist-frequency* f_{max} is the highest resolvable frequency

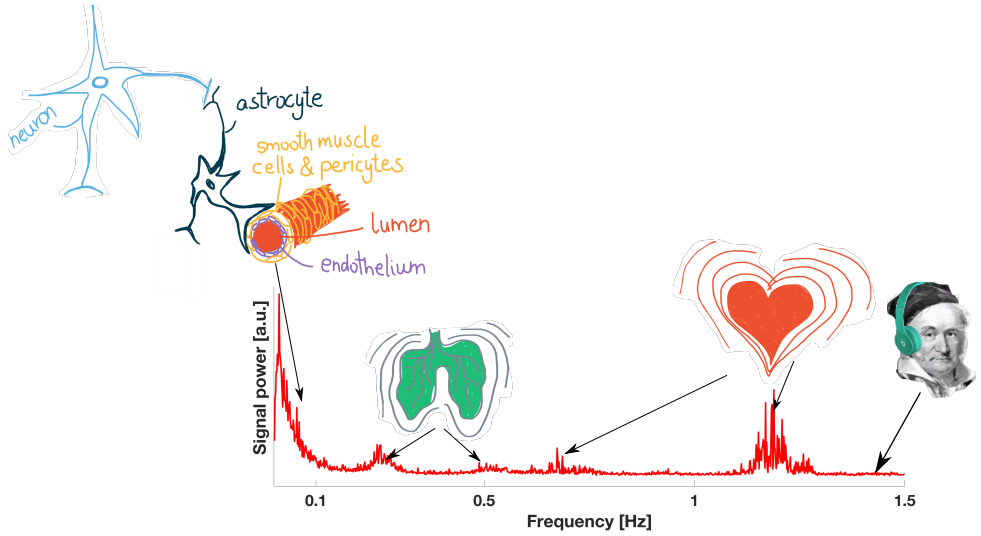


Figure 3.1: The rs-fMRI spectrum and its contributors. The low frequency range (< 0.1 Hz) is governed by the neuro-vascular BOLD-response and vasomotor fluctuations. Respiration can reach into the very low frequencies, but is usually dominant between 0.1 and 0.3 Hz. Cardiac fluctuations are situated at around 1 Hz and aliases of higher harmonics can fold in. The entire spectrum is offset by a baseline power of Gaussian-distributed white thermal noise.

for a given sampling frequency f_s

$$f_{max} = \frac{f_s}{2} = \frac{1}{2\mathrm{TR}}\,. \tag{3.1}$$

Signal fluctuations above f_{max} fold into lower alias frequencies f_a according to

$$f_a(n) = |n f_s - f_{\mathrm{true}}| \quad , n \in \mathbb{N}\,. \tag{3.2}$$

For example a "slow" TR of two seconds has a Nyquist frequency of $f_{max} = 0.25$ Hz, leading to aliasing of cardio-respiratory induced signal fluctuations. fMRI acquisition speed has already benefited from in-plane acceleration techniques, such as GRAPPA [92] and SENSE [93]. Both methods undersample the phase-encode dimension of k-space and thereby reduce slice sample time. As a "lossy" technique they come with SNR penalties and acceleration factors

are limited by the number of receive coil elements. However, a leap in sampling speed came with recent advances in slice-direction acceleration. This was achieved by two major developments: the implementation of RF-pulses that excite multiple slices in the imaging slab simultaneously [94–96] and the unaliasing of collapsed signal from multiple slices, for example with blipped-CAIPIRINHA (standing for Controlled Aliasing in Parallel Imaging Results in Higher Acceleration) [97]. These techniques are termed either "simultaneous multislice " (SMS) or "multiband". They allow an enormous reduction in TR, about equal to the number of simultaneous excitations, i.e. multiband factor. As such, it complements the increased resolution achievable at higher field that increases k-space [98]. Sub-second TRs, whilst keeping a decent spatial resolution and coverage, become feasible. The "unaliasing" of cardio-respiratory signals offers a more reliable sampling for resting-state network analysis, but also a better sampling and analysis of the physiological noise itself. As such, physiological noise is turned into a signal of interest.

3.1.1.2 Spectral composition

0.01 – 0.1Hz: Neuro-vascular fluctuations (BOLD effect)

Neuronal activity triggers a complex interplay of increased cerebral blood volume (CBV), blood flow (CBF) and metabolic rate of oxygen consumption ($CMRO_2$) to cater for the increased demand in oxygen. The vascular response is termed the haemodynamic response (HRF), and is the origin of the BOLD signal [99]. The HRF is magnitudes slower than the underlying neuronal action potentials. Usually the FWHM of the HRF is assumed to be about 4 seconds [100]. A typical timecourse of a BOLD response is given in Figure 3.2. The spatiotemporal characteristics of the HRF vary with cortical depths, mainly due to variations in vascularisation [101]. For high-frequency stimuli

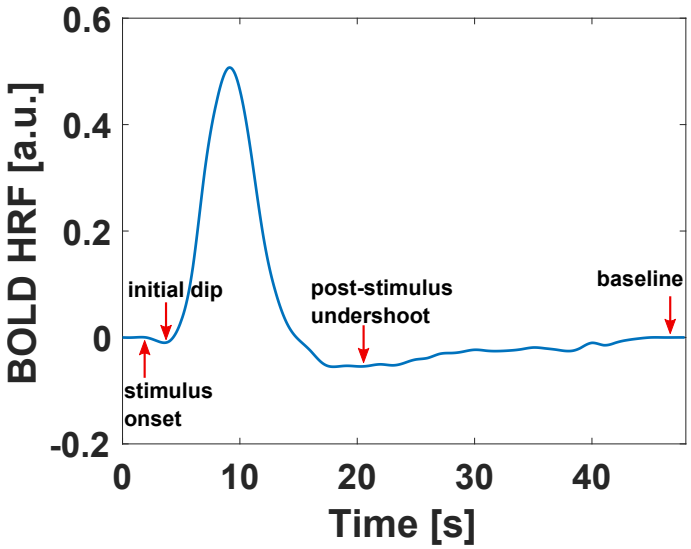


Figure 3.2: Schematic plot of the BOLD HRF after a single time point neuronal activation (stimulus). An initial dip in signal after stimulus onset is followed by a rise to peak over a few seconds. After a post-stimulus undershoot the signal returns to the baseline level. The slow nature of the HRF is temporally blurring the signal.

BOLD signal fluctuations (although phase locked) up to 0.75 Hz have been reported at 7T [102]. However, in the resting state the neuronal network fluctuations are usually assumed to be down-sampled to a range of 0.01-0.1Hz by the slow nature of the HRF, although the underlying electrophysiological activity is much faster [103].

$\approx$ 0.1Hz: Vasomotor fluctuations

Vasomotion refers to vessel diameter fluctuations, often also termed vascular tone. It occurs independent of the heart beat. Vessel expansion and contraction is achieved by smooth muscle fibres that are wrapped around the vasculature. Figure 3.3 shows a schematic picture. The smooth muscle cells were classically thought to be regulated by calcium channels in the astrocytes, however this view has recently been challenged and vasodilation may

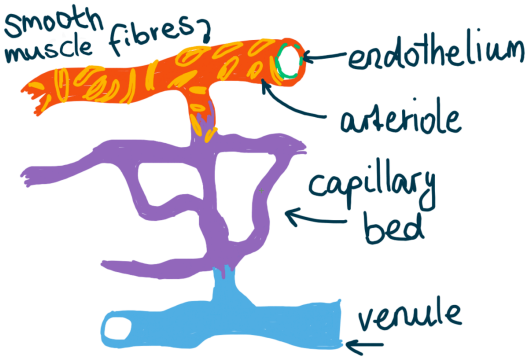


Figure 3.3: Schematic picture of smooth muscle fibres wrapping around the arterial vasculature. They facilitate the expansion and contraction of the vessels during vasomotor oscillations. Fibre density decreases towards the capillaries and very few fibres are found in the venous vasculature.

be regulated via alternative pathways [104]. Vasomotion is thought to be an autoregulatory mechanism, but there is no definite agreement in the literature on the underlying physiological rationale [105]. Animal studies found frequency bands to be inversly related to vessel size, i.e. being highest in the end arterioles [106]. Different cerebral vasomotor wave frequencies have been reported in the literature. They range from $< 0.03\,\text{Hz}$ [107], measured with MRI, to $0.04\,\text{Hz}$ and most prominent $0.1\,\text{Hz}$ [108, 109], measured with near-infrared spectroscopy. Although the definition and knowledge about cerebral vasomotor waves is rather vague, we have to assume that the induced CBF and CBV changes could add to the rs-fMRI spectrum. Recent research suggests that vasomotion-induced EPI signal fluctuations could be linked to vascular properties. For example Patel et al. reported EPI signal decreases at $0.1\,\text{Hz}$ when manipulating vasomotion in rat brains by increasing blood pressure [110].

0.1 Hz: Mayer-waves

Variations in arterial blood pressure over an interval of 10 seconds causes another vascular tone fluctuation referred to as Mayer-waves [111]. The physiological rationale and mechanism are again under debate, but Mayer-waves are thought to be linked to baroreceptor activities [105, 112].

$0 - 0.05\,\mathrm{Hz}$: CO_2 fluctuations

The partial pressure of end-tidal CO_2 ($PETCO_2$) in arterial blood fluctuates at a low frequency range $< 0.1\,\mathrm{Hz}$ at rest [113]. CO_2 is a vasodilator. Hence, $PETCO_2$ oscillations cause variations in CBV and CBF. $PETCO_2$ fluctuations have been proven to account for a unique variance in the rs-fMRI BOLD signal [114, 115]. Fluctuations occur in the range between 0 and 0.05 Hz.

$0.05 - 0.3$Hz: Respiration

Respiration causes multiple changes in the EPI-signal. Chest and diaphragm movements induce magnetic susceptibility variations in the chest, leading to field gradients that extend into the brain. This additional B_0 gradient increases with field strength [116]. At 7T resonance frequency offsets at the head have been reported to be between $1.45 - 4$ Hz [117]. In the case of EPI this produces shifts in the phase-encoding dimension. Other respiratory-induced phenomena are subject bulk movement and O_2 fluctuations in the venous compartment that arise from thoracic pressure changes [118]. Respiration rates vary amongst individuals between $0.05 - 0.3\,Hz$ with decreasing frequencies towards resting, drowsy and sleeping state and can lead to an overlap with the neuro-vascular spectrum. When "slow" TRs are used respiratory frequencies and harmonics can further alias into the spectrum. Figure 3.4 illustrates the effect of respiratory signal aliasing on the power spectrum for three different TRs.

$0.6 - 1.5\,\mathrm{Hz}$: Cardiac fluctuations

The cardiac pressure wave causes a variation in the EPI-signal. An in-depth investigation of this phenomenon will be the subject of Chapter 4. One cardiac-induced mechanism is brain movement. It has been measured to

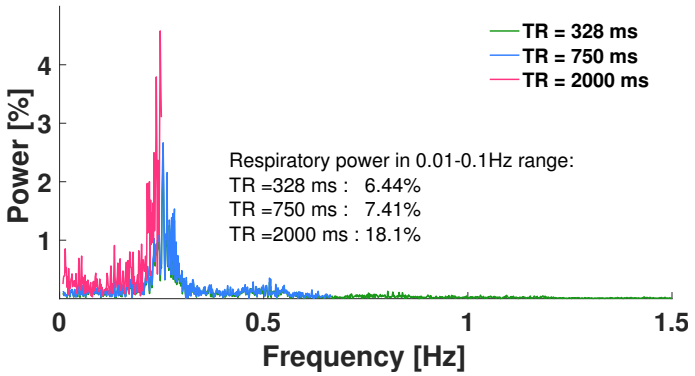


Figure 3.4: A respiratory power spectrum sampled at different TRs. The Nyquist frequencies are $f_{max} \approx 1.5\,\text{Hz}$ (TR= $328\,ms$), $f_{max} \approx 0.67$ Hz (TR=750 ms) and $f_{max} = 0.25\,\text{Hz}$ (TR=$2\,s$).

be most severe in the brainstem with a maximum velocity of $1.5 - 2\,\text{mm/s}$ during systole [119], with "movement [occuring] in a funnel-shaped fashion as if the brain were pulled by the spinal cord" [78]. Besides tissue movement CSF moves in narrow spaces and around the arterial structures. EPI signal fluctuations in tissue are further caused by changes in CBV and CBF over the cardiac cycle. Cardiac frequencies vary across healthy individuals from about $0.6 - 1.5\,\text{Hz}$ at rest. To guarantee the unaliased sampling of the fundamental cardiac frequencies a TR shorter than about $300 - 350\,\text{ms}$ is needed. Figure 3.5 shows an example cardiac spectrum sampled at different TRs. In this case a TR of $750\,ms$ is too long to unalias the cardiac fluctuations. Note that there is a second minor cardiac peak at around $f = 0.6\,\text{Hz}$ in the spectrum of the fast TR= $328\,ms$ sampling. This is an alias of the second order harmonic of the dominant cardiac peak at $\approx 2.4\,\text{Hz}$ ($\approx 2 \cdot 1.5 - 2.4 = 0.6$ after Eq. 3.2). Besides the dominant peak there can further be low frequency oscillations in the cardiac cycle. Often they are termed heart rate variability and are ascribed to regulatory waves of the autonomous nervous system causing variations at about 0.04Hz [120]. Heart rate variability has been shown to contribute to the rs-fMRI signal variance [121].

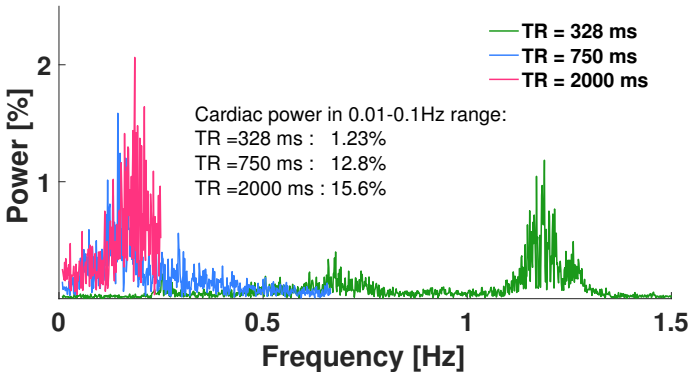


Figure 3.5: A cardiac power spectrum sampled at different TRs. The Nyquist frequencies are $f_{max} \approx 1.5\,\text{Hz}$ (TR= $328\,ms$), $f_{max} \approx 0.67$ Hz (TR=750 ms) and $f_{max} = 0.25\,\text{Hz}$ (TR=$2\,s$).

Miscellaneous

Although single-shot EPI is a rather fast imaging technique and freezes bulk motion in the single image, there can be signal variations from spin history effects. Slow subject motion (e.g. a drift of the head over the scan time) causes low-frequency fluctuations. Motion correction in post-processing can realign the position, but dropout and spin history effects are irreversible. Drifts in the baseline signal are further introduced by instabilities in the scanner hardware causing B_0 drifts in the range of $0 - 0.015\,\text{Hz}$ [122].

3.1.2 Quantifying spectral contributions

3.1.2.1 Amplitude of low frequency fluctuations

In the above review of the BOLD spectrum we found much low frequency contribution phenomena that are related to vascular properties, from the HRF to vasomotion or PETCO_2-induced signal fluctuations. The HRF varies strongly between subjects [123] and within a subject and cortical-depth-dependent vascular architectures and densities have been shown to correlate

with the amplitude in rs-fMRI as well as task-based fMRI [124,125]. Between-subject disparities are largely attributed to different levels of physiological baseline state [126, 127]. As such, the rs-fMRI power in the low frequency range has gained interest in recent years as a means of studying neurological diseases and vascular ageing. A measure called "amplitude of low frequency fluctuations" (ALFF), was introduced initially as the power sum between 0.01 and 0.1 Hz [128]. It is derived by Fourier-transforming the time series $x(t_j)$

$$\tilde{X}(f_i) = FFT[x(t_j)] \qquad j = 1 \ldots N,\, i = 1 \ldots \frac{N}{2}\,. \tag{3.3}$$

and summing over the power amplitudes $A(f_i)$ in the low frequency range

$$A(f_i) \;=\; \sqrt{Re(\tilde{X}(f_i))^2 + Im(\tilde{X}(f_i))^2} \tag{3.4}$$

$$\text{ALFF} \;:=\; \sum_{f_i=0.01}^{0.1} A(f_i)\,. \tag{3.5}$$

As this definition uses the absolute amplitudes it is basically impossible to compare results between different scanner sites and even a subject test-retest has been shown to be unreliable [129]. The normalised form of a "fractional amplitude of low frequency fluctuations" (fALFF) [130] has been widely adopted instead

$$\text{fALFF} := \sum_{f_i=0.01}^{0.1} \text{fA}(f_i) \tag{3.6}$$

with $\text{fA}(f_k)$ simply being normalised by the total spectral power

$$\text{fA}(f_i) = \frac{A(f_i)}{\sum\limits_{f_{min}}^{f_{max}} A(f_i)}\,. \tag{3.7}$$

fALFF and ageing

A fALFF decrease in a subset of grey matter (GM) areas has been reported in healthy ageing [131] and similar findings were reported using the RSFA (standing for Resting State Fluctuation Amplitude, which is the standard deviation of amplitude fluctuations in the time domain) [132]. Age-related arterial wall stiffening can be attributed to many mechanisms and the literature provides a long list, such as endothelial cell dysfunction (the cell layer between lumen and smooth muscle cells), increases in collagen (molecules promoting tensile stiffness), lipid accumulation and changes in the smooth muscle cells or dysfunctions in the neuronal signalling pathways of vasoconstriction [133–135]. The reduced ability of arteries to expand and contract could affect the amplitude of CBV and CBF changes. This would alter the HRF itself as well as vasomotion-induced signal fluctuations and could be an explanation for the reported fALFF decrease. However, the simpleness of the fALFF (only being the integrated power in a frequency band) renders it a rather "brute force" measure. It does not allow a disentanglement of all the possible contributors to the low frequency range and neuronal changes with age could be the origin of the reported fALFF decline as well. A change in haemodynamic coupling to neuronal activity with normal ageing has been suggested [136]. A study of 7- to 61-years old subjects reported systematic changes in the HRF timecourse, of which the latency of the trailing edge was the most significant factor to change with age (being prolonged with age) [137].

3.1.2.2 Cardiac frequency fluctuations

So far the literature has focussed on comparing the low frequency range of the spectrum. This might be attributed to previous sampling speed limitations,

but the recent improvements in acquisition speed transform cardiac signals from "noise" into informative signal. The question of whether vascular properties are reflected in the cardiac frequency band hence becomes interesting. Similar to the known alterations of the HRF with vascular density and potential wall stiffening, there should be an effect on the haemodynamic response to the arterial pressure wave. One study by Makedonov et al. [138] used fast rs-fMRI to introduce a cardiac BOLD power measure. Their "Cardiac Pulsatility Metric" (CPM) aims to calculate the amount of signal fluctuation in percent at the cardiac frequency. Their strategy is to identify the frequency component with the highest power amplitude f_c in an externally measured cardiac spectrum (pulse-ox) and calculate the average power within a window of $\pm 0.02\,\mathrm{Hz}$ around it

$$\mathrm{CPM} = \sum_{f_i=f_c-0.02}^{f_c+0.02} \mathrm{fA}(f_i)\,. \tag{3.8}$$

This width is chosen on a "manual evaluation of the average width of the cardiac peak" [138]. They compared CPM variations in a group of younger and healthy older subjects and small vessel disease patients. They found a CPM increase with age, particularly in the white matter (WM), and a further increase in the patients.

The CPM is based on a fixed frequency window width (similar to fALFF). We suspect this definition to be problematic as heart rate variations are known to decline with age [139], i.e. older subjects' cardiac power spectra are narrower, whereas younger subjects' spectral power is distributed over a broader range of frequencies. Consequently, a fixed frequency window may find an age-dependent difference in the amount of cardiac "input" power that might actually be explained merely by changes in the cardiac width.

We therefore propose here to compare the amount of transmitted power for a fixed amount of input power, which is thus a measure of efficiency (details are presented in the Methods).

3.1.3 Scope of this work

In this chapter we aim to model broad-band spectra, obtained with fast fMRI, aided by externally measured cardio-respiratory recordings. We introduce a general linear model (GLM) to disentangle neuro-vascular from cardio-respiratory contributions. The very low frequency range is quantified by means of the fALFF in a healthy cohort of "younger" and "older" subjects to test the decline in fALFF with ageing reported previously in the literature. With the GLM we can further regress out cardio-respiratory fluctuations which potentially provides us with insights into what contributes to the age-related fALFF decline.
In particular, we are interested in studying the cardiac frequency band, that to date has been studied to a lesser extent. We introduce a cardiac efficiency measure and compare it with the previously reported CPM measure.

3.2 Methods

3.2.1 General linear model

Figure 3.6 shows an average whole brain rs-fMRI spectrum with the cardio-respiratory spectra plotted below. The physiological spectra were obtained with an external measurement (pulse-ox and respiratory pad) during the scan. Above the low frequency range the EPI spectrum looks almost like a replica of the physiological spectra and suggests that it could be modelled

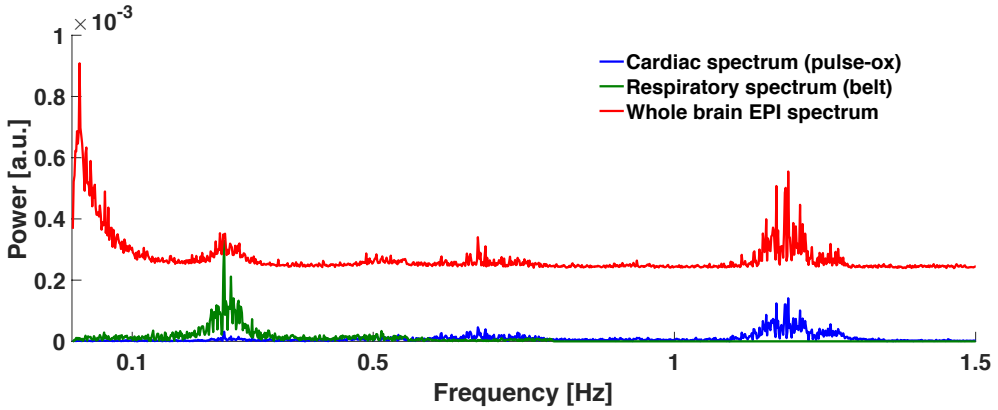


Figure 3.6: A single subject's average rs-fMRI spectrum (red) and the simultaneously acquired respiratory (green) and cardiac (blue) spectra.

by a GLM with the external physiological spectra as explanatory variables.

Let $Y(f)$ be the power spectrum (i.e. magnitude of the signal) of a single voxel's rs-fMRI time course. Here we assume that the HRF down-samples any neuronally driven signal to at least below 0.2 Hz. The power distribution above the threshold can then be modelled as a combination of respiratory $X_r(f)$, cardiac $X_c(f)$ and thermal noise spectra. Thermal noise is assumed to be frequency independent and modelled as a constant. A voxel-by-voxel linear regression

$$Y(f) = \alpha + \beta_r X_r(f) + \beta_c X_c(f)\,, \qquad \text{with } f > 0.2\,\text{Hz} \tag{3.9}$$

provides spatial regressor maps α, β_r and β_c that quantify how much thermal noise, respiration and cardiac fluctuations contribute to the signal power in each voxel. All spectra are normalised, i.e.

$$\sum_{f_i=0}^{f_{max}} Y(f_i) = 1,\,. \tag{3.10}$$

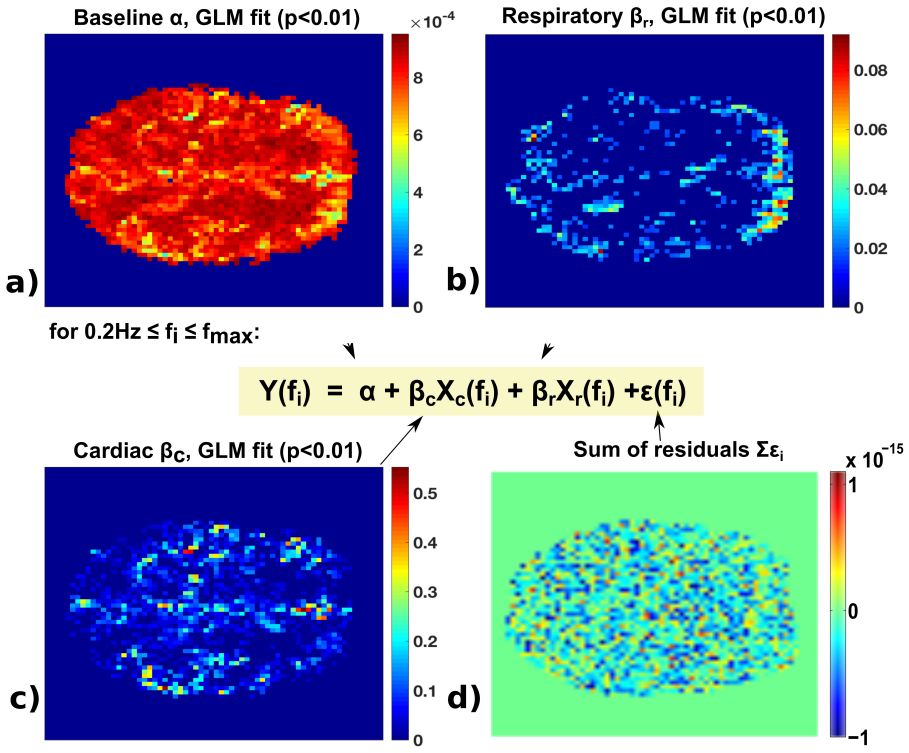


Figure 3.7: The GLM with example maps from a single subject. The EPI spectrum above 0.2 Hz is modelled by a constant noise baseline (a), a respiratory (b) and a cardiac regressor (c). The residuals are shown in (d).

The external cardio-respiratory spectra $X_{r,c}(f)$ are normalised in the same manner, i.e. the sum under the power spectra curves is 1. Figure 3.7 illustrates the model with example regressor maps. The regressor maps α, β_r and β_c can be used for the purpose of identifying voxels with significant physiological signal modulations and to regress out their power contribution. Although the physiological regressor maps are derived (or "trained") on frequencies above 0.2 Hz we make the assumption that we can subtract the power in the low frequency range as we know the physiological spectra for the entire range. This can be particularly relevant for subjects that have very slow respiratory cycles, low frequency heart rate variability or higher order

cardiac harmonics that alias into the fALFF range. We define a "cleaned" version of the fALFF (cfALFF) as

$$\text{cfALFF} := \quad \text{fALFF} - \sum_{f_i=0.01}^{0.1} [\alpha + \beta_r X_r(f_i) + \beta_c X_c(f_i)] \tag{3.11}$$

3.2.2 Dual regression

The proposed GLM uses the externally measured chest movements and pulse-ox signals as a template. The assumption that chest movement can be linearly translated to all respiration-induced EPI signal fluctuations is an over-simplification. Different aspects associated with respiration will translate into different amounts of EPI signal fluctuations and further might be frequency dependent. For example, air volume change, associated with breathing affect B_0, but respiratory volume will also influence PETCO_2 levels which in turn influence the EPI signal via vasodilation mechanisms. The pulse-ox measures cardiac fluctuations at the finger tip which are likely filtered throughout the vascular tree with higher order oscillations being damped. To test for frequency-dependent gains or filters we expand the GLM approach and incorporate an additional dual regression step.

The dual regression concept has been used in the literature on rs-fMRI time series data for subject-specific rs-network analysis [140, 141]. A typical statistical analysis of rs-fMRI signals is usually done using independent component analysis (ICA). ICA assumes that the fMRI signal is the sum of independent sources (components) that are non-Gaussian distributed in their values. The spatial maps (of an ICA component) of a group level functional connectivity analysis are used as a set of spatial regressors in a second

GLM to solve for the time series associated with each particular map. The resulting timecourses are then used as explanatory variables in a re-run of the initial GLM to find subject-specific maps associated with the particular component. Here, an equivalent strategy can be applied to the spectral data. Figure 3.8 gives an overview of the steps. There are three steps involved:

1. **Run a GLM according to the model in Eq. 3.9** with the externally measured physiological data as the "initial guess" of the explanatory variables.

2. Strip the resulting α, β_c and β_r maps along the spatial dimension. **Run a second GLM along the frequency dimension** (opposed to the spatial dimension in step 1) to find refined physiological spectra $\tilde{X}_c$ and $\tilde{X}_r$ and noise baseline constant $\tilde{\mathbf{1}}$.

3. **Re-run step 1 with the refined spectra** as input and compute the associated refined spatial maps $\tilde{\alpha}$, $\tilde{\beta}_c$, $\tilde{\beta}_r$.

For the remainder of the section we will refer to the first GLM regressor maps α, β_r, β_c as "initial" regressor maps and to the dual regressed $\tilde{\alpha}$, $\tilde{\beta}_c$, $\tilde{\beta}_r$ as "refined". The initial externally measured spectra and the new brain-specific refined spectra can then be compared to infer if there are frequency amplifications or attenuations. Also, the refined spectra together with the refined spatial maps should explain the unique variance of the data with the baseline, cardiac and respiratory fluctuations[1].

[1]The unique variance of an observed variable (here the rs-fMRI voxel spectrum) with an explanatory variable is the amount of specific variance that is not shared with any other explanatory variable of the model and the error variance. [142]

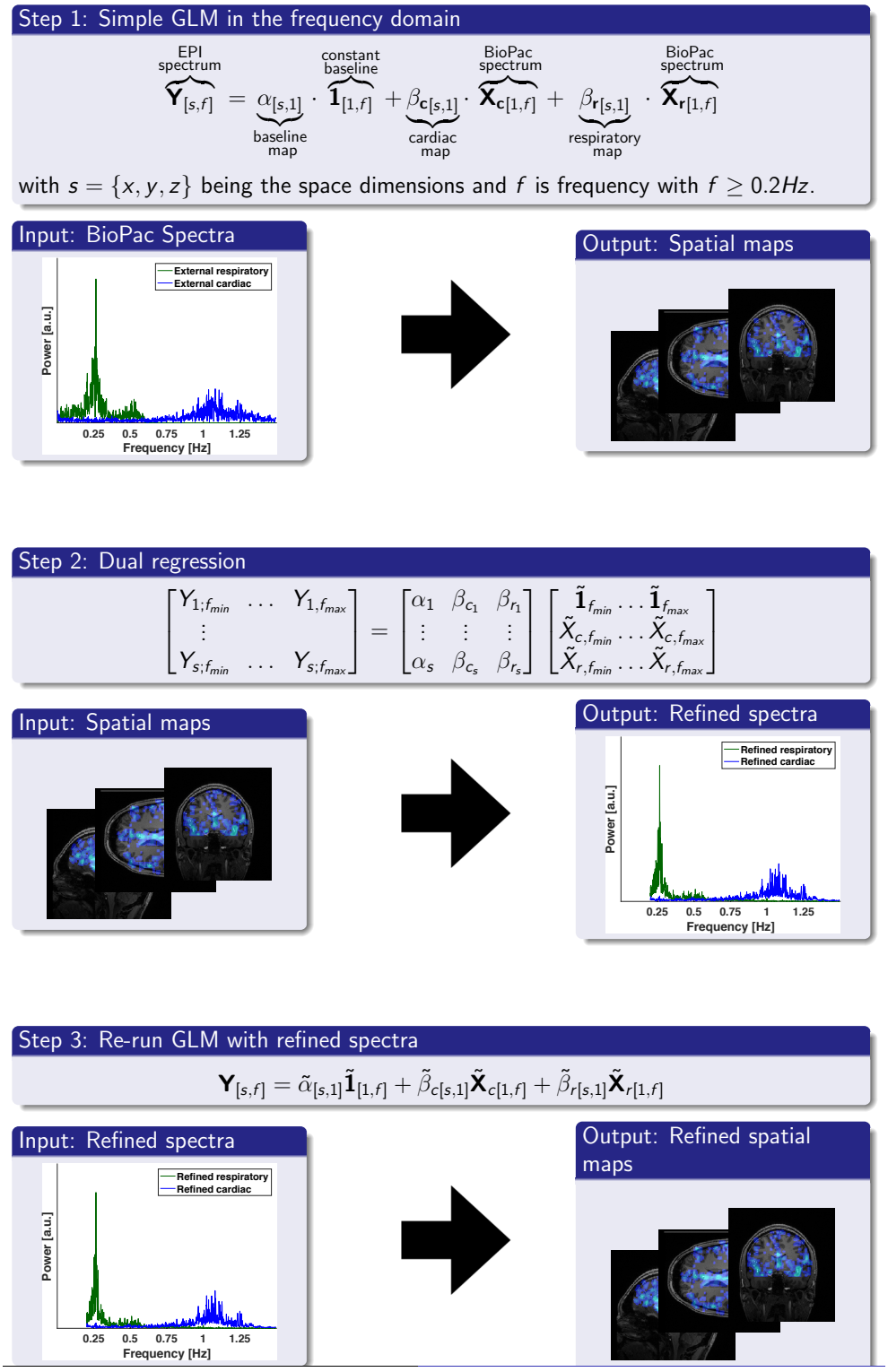


Figure 3.8: Schematic overview of the dual regression analysis.

3.2.2.1 Cardiac efficiency measure

To complement and expand the spectral analysis we define a similar measure to the fALFF (Eq. 3.6) for the cardiac fluctuations. The "cardiac efficiency measure" (CEM) measures the fMRI power, subtracted by the noise baseline, for a fixed input power

$$\text{CEM} := \sum_{f_i \in F_{c,max}} [\text{fA}(f_i) - \alpha] \tag{3.12}$$

with

$$\{f_i \in F_{c,max} \,|\, X_c(f_i) < X_c(f_{i-1}) < ... < X_c(f_1) \;\&\; \sum_i X_c(f_i) = 0.1\}\,, \tag{3.13}$$

the above definition describes the subset $F_{c,max}$ of frequency components with the highest power amplitude in the external cardiac spectrum $X_c(f)$ (first condition of definition 3.13) that sum up to a total power of 10% (second condition of definition 3.13). This definition allows the number of frequency components to vary between subjects in contrast to the fixed range used in the original fALFF and CPM definitions. To illustrate our rationale to chose a variable window width for the CEM measure we plotted representative cardiac spectra for a younger (21 years) and an older (57 years) subject in Figure 3.9. The younger subject's cardiac power is distributed over many more frequencies than the older subject. If we were to use a fixed frequency range we would compare significantly different levels of cardiac input power into the brain. Hence, our decision to compare the strongest cardiac components that together transmit a fixed amount of power. The fixation of the input power to 10% was based on our experience that a larger value led to the inclusion of aliased components of higher-order harmonics in some subjects. We did

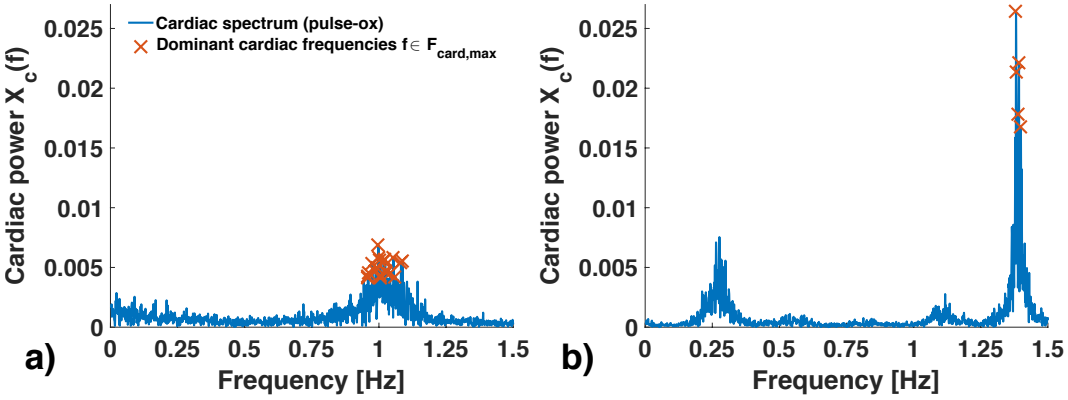


Figure 3.9: Representative cardiac power spectra for a younger subject of 21 years (a) and an older subject of 57 years (b). The dominant cardiac frequencies as defined by Eq. 3.13 are marked by the red crosses. The younger subject has a broader cardiac spectral width, whereas the older subject's cardiac power is represented by fewer frequency components.

not want to include aliased components as we found their power contribution to be overestimated with the external measurement as we will show later in the results of the dual regression analysis.

3.2.3 Analysis goals

With the methods outlined above we investigated the following points:

3.2.3.1 Initial vs. dual GLM

We compared the externally measured spectra X_c, X_r with the refined spectra $\tilde{X}_c$, $\tilde{X}_r$ by simple subtraction

$$X_q(f_i) - \tilde{X}_q(f_i) \begin{cases} < 0 & \text{filter} \\ = 0 & \text{ideally explained,} \\ > 0 & \text{gain} \end{cases} \qquad q = r, c. \tag{3.14}$$

If a frequency component in the refined spectrum $\tilde{X}(f_i)$ is smaller than in the externally measured spectrum we will refer to this as a "filter" effect as the brain-specific spectrum appears to have reduced power at this component. If the refined spectrum is larger than the external measured component we refer to it as a "gain" effect as this component appears to have an enhanced power in the brain. We further compared the average values of the initial and refined regressor maps α, β_c, β_r and $\tilde{\alpha}$, $\tilde{\beta}_c$, $\tilde{\beta}_r$. We calculated tissue-specific mean regressor values over all subjects. The tissue-specific average regressor $\langle\beta\rangle$ was calculated such that partial volume estimates (PVEs) were taken into account. A PVE-weighted sum over all βs from significantly modulated voxels, was divided by the tissue-specific volume

$$\langle\beta_q\rangle = \sum_{\substack{\mathrm{PVE}(s)>0.7 \\ p_q(s)<0.01}} \beta_q(s)\cdot\mathrm{PVE}(s) \Big/ \sum_{\substack{\mathrm{PVE}(s)>0.7 \\ p_q(s)<0.01}} \mathrm{PVE}(s)\,, \qquad q=\mathbf{1},r,c\,. \quad (3.15)$$

The p-value threshold was set to 0.01 to only include voxels that are significantly modulated by each phenomenon. To mitigate partial voluming effects we only included voxels with PVE values higher than 0.7.
We further calculated the ratio of significantly modulated volume to total mask volume ("spatial extent of the effect")

$$R_q = \sum_{\substack{\mathrm{PVE}(s)>0.7 \\ p_q(s)<0.01}} \mathrm{PVE}(s) \Big/ \sum_{\mathrm{PVE}(s)>0.7}^{N} \mathrm{PVE}(s)\,, \qquad q=\mathbf{1},r,c\,. \quad (3.16)$$

The refined ratios $\tilde{R}_q$ are defined in the same manner. Ideally, if our explanatory variables of the noise baseline and the cardio-respiratory spectra $(1, X_c, X_r)$ were completely explaining the voxel spectra above the neurovascular frequency range, then the refined spatial maps and spectra would ex-

plain the unique variance of the voxel spectra. Despite the fact that there are additional sources above 0.2 Hz that we do not model for, we expected a reduction in the dual regression results $\tilde{R}_q \leq R_q$ as the shared variance will be removed, for example a shared variance between respiratory and cardiac spectra.

3.2.3.2 Age-related changes in the BOLD spectrum

We compared the fALFF in a group of younger and older people. Besides the standard fALFF we also calculated the cleaned cfALFF (Eq.3.11), that has the cardio-respiratory power regressed. We expected respiratory overlap in the low frequency range to be a confounding factor. Cardiac power in the low frequency range potentially correlates with age. Therefore we calculated the cfALFF for different stages of regression, i.e only regressing the baseline vs. regressing baseline and respiratory component vs. regressing baseline and cardio-respiratory components. Besides the low frequency range we also assessed the introduced CEM measure. All measures were calculated in different tissues using the same PVE-weighted approach as explained in the previous section, i.e.

$$\langle \mathrm{fALFF} \rangle = \sum_{\mathrm{PVE}(s)>0.7} \mathrm{fALFF}(s) \cdot \mathrm{PVE}(s) \Big/ \sum_{\mathrm{PVE}(s)>0.7} \mathrm{PVE}(s)\,. \qquad (3.17)$$

The tissue-specific CEM averages were only calculated from voxels that had a significant cardiac modulation (as derived from the GLM)

$$\langle \mathrm{CEM} \rangle = \sum_{\substack{\mathrm{PVE}(s)>0.7 \\ p_c(s)<0.01}} \mathrm{CEM}(s) \cdot \mathrm{PVE}(s) \Big/ \sum_{\substack{\mathrm{PVE}(s)>0.7 \\ p_c(s)<0.01}} \mathrm{PVE}(s)\,. \qquad (3.18)$$

We further compared the CEM measure with the recently proposed CPM of Makedonov et al. [138]. They calculate the CPM measure in eroded tissue masks and included all voxels (i.e. no effect significance threshold, like the p-value in our case). Therefore we also calculated a "modified CPM", that matches the calculation of our CEM and is derived from PVE-weighted values and is further masked by the cardiac p-value.
We used a two-sample t-test to test for group differences between the younger and older groups for the above described measures. The p-values of the t-test were further divided by the number of comparisons made, i.e. were "Bonferroni"-corrected.

3.3 Data and post-processing

3.3.1 MR data

21 healthy subjects were scanned at the *Max-Planck-Institute for Human Cognitive and Neuroscience* in Leipzig, Germany. The study was covered by the institutional ethics "Magnetresonanz-Untersuchung am Menschen bei 7 Tesla (Az.: 273-14-25082014)". Subjects were divided into a younger group of average age 23 ± 3 years (10 subjects) and an older group of average age 63 ± 9 years. The scans were acquired on a 7T whole-body scanner (MAGNETOM 7T, Siemens, Erlangen, Germany) using a 1 channel Tx/32 channel Rx head coil (Nova Medical, Wilmington, MA, USA). Physiological signals were measured throughout the scan session using a respiratory pad and a pulse-ox that was attached to the index finger. Signals were recorded at 1kHz (BioPac Systems, Goleta, CA, USA).

Tissue segmentation: MP2RAGE

An MP2RAGE [143] dataset was acquired with TR = 8250 ms, echo time; TE = 2.46 ms, inversion time; TI_1/TI_2 = 1000/3300 ms (non-selective inversion recovery), flip angles; $FA_1/FA_2 = 7°/5°$, voxel resolution = 0.8 mm isotropic, field of view; FOV_{read} = 210 mm, FOV_{phase} = 100%, phase partial Fourier = 6/8, 208 slices, acceleration factor; GRAPPA = 2, bandwidth; BW = 240 Hz/px. Scan time ≈ 14.5 mins.

rs-fMRI: EPI

A multiband EPI scan in the resting state was acquired with TR = 328 ms, TE = 26 ms, FA = 33°, voxel resolution = 3.0 mm isotropic, FOV_{read} = 200 mm, FOV_{phase} = 100%, phase partial Fourier = 7/8, 28 slices, multiband factor = 3, GRAPPA = 3, BW = 1994 Hz/px, inter-echo spacing; ESP = 0.68 ms, 2200 volumes. Scan time ≈ 12 mins. A separate field map was acquired for distortion correction. It is of note, that the resolution is comparably low for a 7T study, but is likely to be more weighted towards the "physiological noise regime" [144].

3.3.2 Post-processing

Tissue segmentation: MP2RAGE

The T1-weighted (T1w) scan was run through FSL's *fsl_anat* pipeline. It performs skull stripping and bias field correction (which is enhanced at 7T) and calculates PVE maps for tissue segmentation [145]. An arterial mask was created from the T1w scan using the inherent bright signal of fast arterial blood in the larger arteries. This inflow effect is enhanced at 7T since only a head coil is used for RF-excitation, in contrast to the conventional whole-

body transmission at 3T [65]. A threshold was chosen on a subject-by-subject basis to create a binary vessel mask. The EPI scan was registered to the T1w image and the inverse transformation was then applied to the PVE maps and the vessel mask for analysis in functional space.

rs-fMRI: EPI

The dataset was processed through FSL pipelines, including skull stripping, motion correction, field map correction and de-meaning. The data were not spatially smoothed. The processed data were then read into MATLAB, R2016a (Mathworks, Nattick, USA) to perform the GLM and dual regression analysis. Baseline α, respiratory β_r and cardiac β_c regressor maps of the initial GLM and refined maps $\tilde{\alpha}$, $\tilde{\beta}_c$, $\tilde{\beta}_r$ and refined physiological spectra $\tilde{\mathbf{1}}$, $\tilde{X}_c$, $\tilde{X}_r$ were calculated. Masks were thresholded by p-values and PVE-values as explained in the Methods[2].

3.4 Results

3.4.1 Initial vs. dual GLM

Figure 3.10 shows tissue-specific spectra from a representative subject. The low-frequency power in the GM mask (Figure 3.10a) is maximised compared to WM and the arteries, as expected from its large neuro-vascular component. The WM spectrum (Figure 3.10b) is generally "flatter", reflecting its negligible neuronal contributions and weaker cardiac component as WM is less vascularised. As expected the cardiac peak is particularly pronounced

[2]With the exception of the arterial masks which were thresholded at 0.1 because larger thresholds resulted in almost empty arterial masks, as the arteries are relatively small compared to the voxel size.

in the arterial mask (Figure 3.10c). The yellow and purple plots in Figure 3.10 are the error residuals after initial GLM and dual regression. The closer to zero, the better the model. The differences between the externally measured BioPac and the dual regressed spectra as (Eq. 3.14) are plotted for all three explanatory variables α, β_c, β_r in Figure 3.11 for the same subject as in Figure 3.10.

Noise baseline

An initial hypothesis of the GLM was that thermal noise is frequency independent and can be modelled by a constant offset. Looking at Figure 3.11a we conclude that this is a fair assumption. The dual regressed noise spectrum $\tilde{\mathbf{1}}$ (purple line) negligibly deviates from the initial constant value. Deviations occur in the respiratory and cardiac range and could be an indication that the cardio-respiratory explanatory variables are not "ideal". Note the peak at $f \approx 0.55\,\mathrm{Hz}$. This spike is present in all rs-fMRI spectra (see Figure 3.10), but is absent in any of the externally measured physiological spectra. It might be a hardware fluctuation, but we preclude the cold head frequency which is about one Hz.

Cardiac spectrum

The comparison of the refined and initial BioPac cardiac spectra for a representative subject in Figure 3.11b reveals a frequency-dependent enhancement and attenuation of certain cardiac power amplitudes in the brain. Figure 3.12 shows a zoomed presentation of these cardiac spectra. The power at the dominant frequencies is underestimated by the pulse-ox measurement, whereas the lower power frequencies of the cardiac peak are overestimated. Even more attenuated is the aliased second order harmonic at $\approx 0.85\,\mathrm{Hz}$.

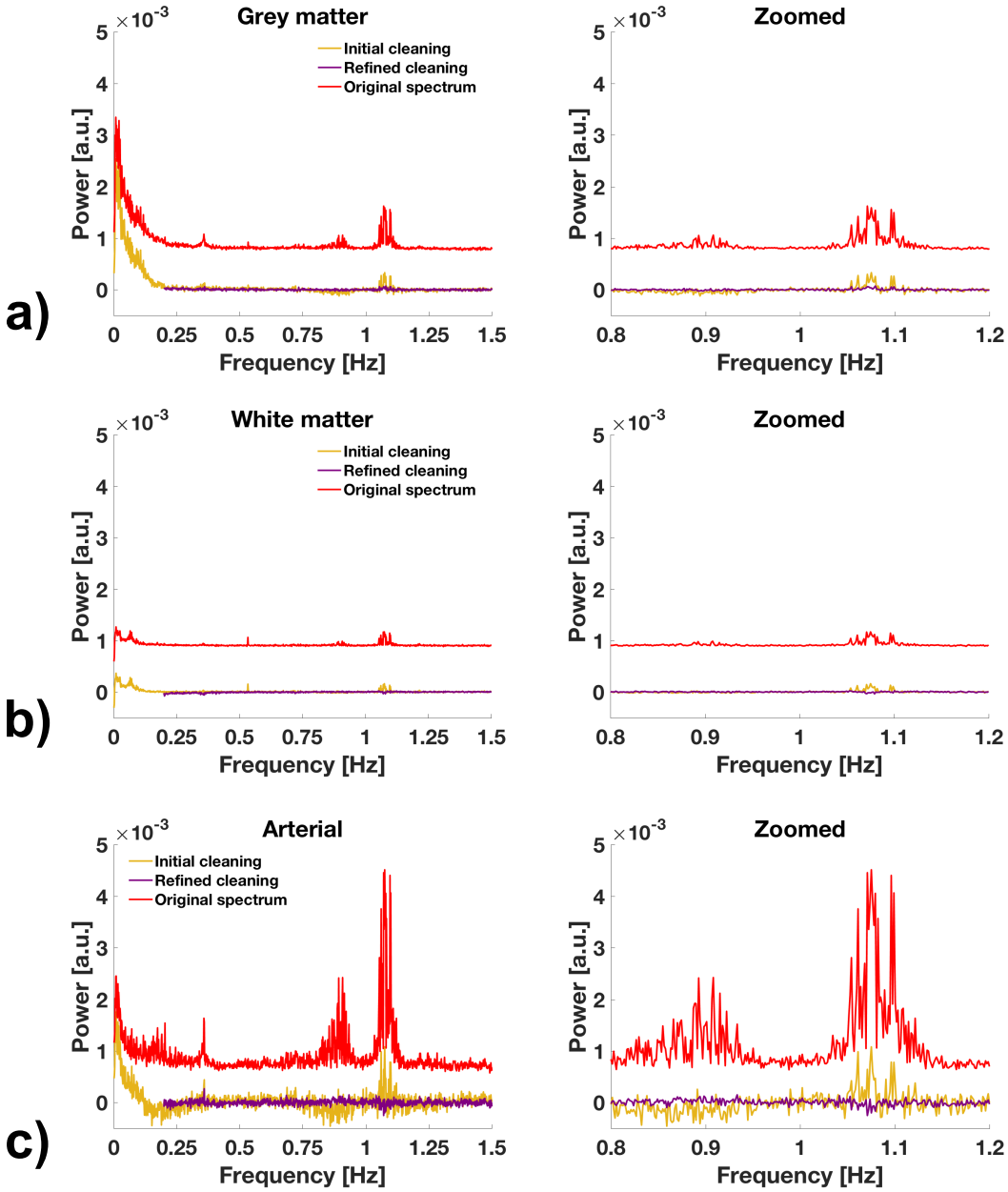


Figure 3.10: Example GM (a), WM (b) and arterial (c) EPI spectra. The left side displays the entire spectrum and the right zooms into the cardiac range. The red lines are the original EPI power spectra averaged within the specific tissue mask. It is to note, that the original spectra are all normalised (area under the red curve is 1). The yellow plots are the cleaned spectra, with regression of the baseline and cardio-respiratory regressors from the initial GLM. The purple line is the residual error when cleaned by the dual regression.

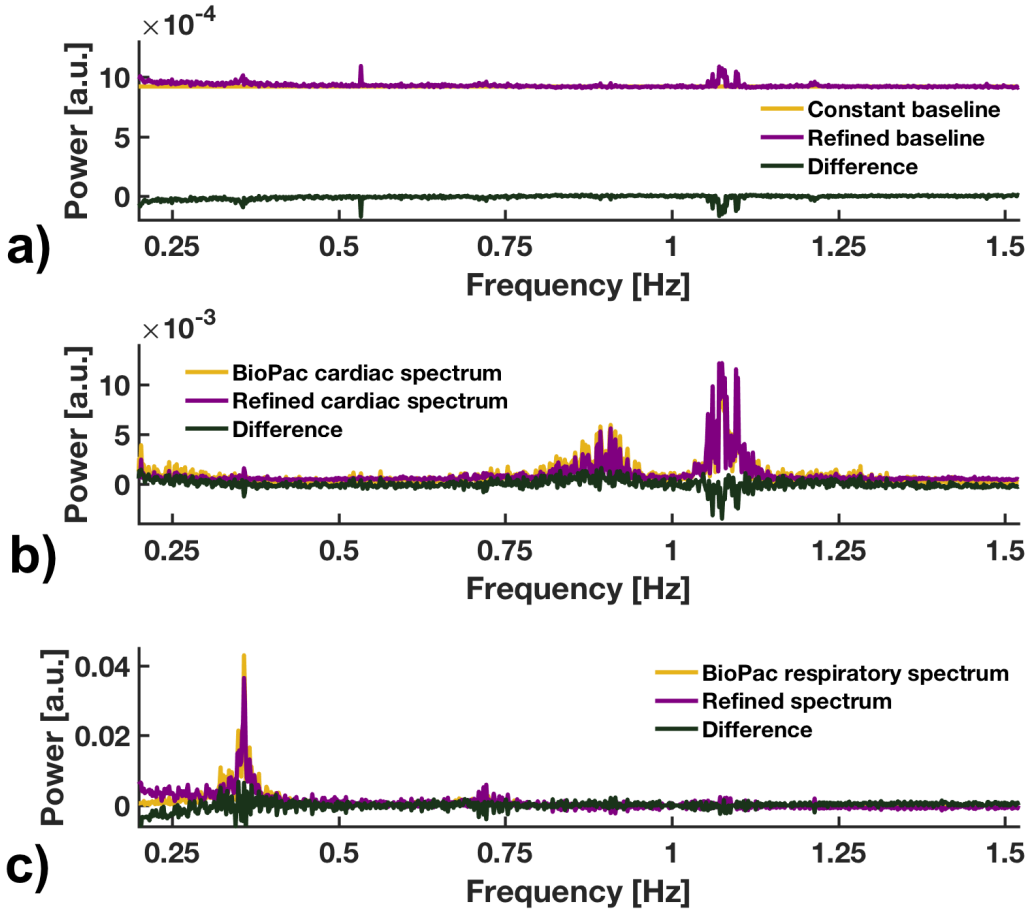


Figure 3.11: Comparison of the externally measured and progressively refined spectra from dual regression in a single subject. The yellow plots refer to the initial GLM explanatory variables, the purple plots are the refined spectra from the dual regression steps and the black lines are the differences between the two. **a)** baseline, **b)** cardiac, **c)** respiratory spectra.

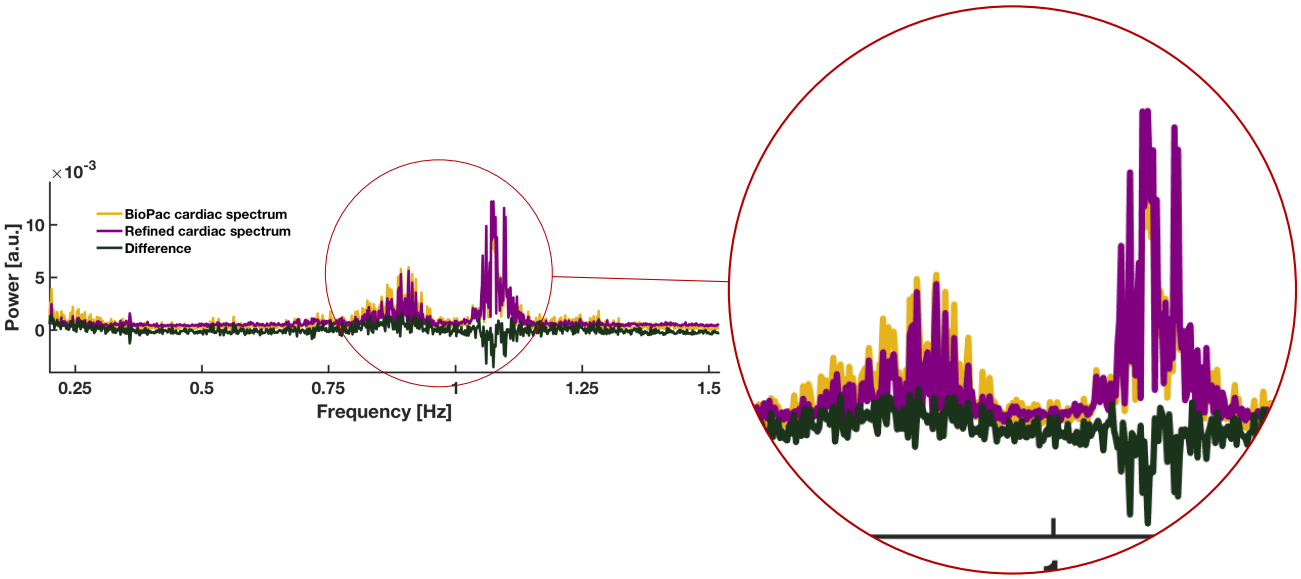


Figure 3.12: Zoom into Figure 3.11b), showing the amplification of the dominant cardiac frequencies in the brain-specific spectrum and the filtering of the aliased higher-order harmonic.

In all subjects we observed that the refined brain-specific cardiac spectrum, compared to the pulse-ox spectrum, distributes more power into fewer components (the dominant ones). Higher harmonics are attenuated. The same observation was made in subjects with slow heart beats ($< 0.75\,\mathrm{Hz}$) where the second harmonic was still temporally resolved. Therefore we conclude that the damping of higher harmonics is independent of the aliasing process and that this filtering effect is intrinsic to the brain physiology and not to the sampling.

Respiratory spectrum

The respiratory spectrum shows a reversed behaviour. We found that the dominant respiration power is overestimated by the external measurement, but lower frequency fluctuations tend to be underestimated. Compared to the baseline and cardiac spectra, the respiratory spectrum has higher error

residuals.

Regressor values

Table 3.1 lists the average regressor and fraction of significantly modulated tissue volume (Eqs. 3.15 and 3.16) for each tissue. There is no significant difference between initial and dual regressors in the thermal noise baseline. Thermal noise contribution is highest in WM, again this is explained by the minimal neuro-vascular, as well as cardiac contribution (recall that spectra are normalised). The fraction $\tilde{R}$ of voxels explained reduces in the dual regression as expected. The reduction in $\tilde{R}_r$ is higher than in $\tilde{R}_c$, with a decrease of $\approx 20\%$ in GM and WM, versus $\approx 10 - 15\%$ in the cardiac case. The cardiac regressor values and amount of significantly modulated voxels in the arterial mask differ the least between the initial and dual regression, i.e. the arterial spectra are the most similar to the pulse-ox spectra.

3.4.2 Age-related changes

3.4.2.1 Low frequencies: fALFF vs. cfALFF

fALFF and cfALFF results for the two age groups are displayed in Figure 3.13, with p-values highlighted in red if below $2.5 \cdot 10^{-3}$ (which is the 0.01 significance level after Bonferroni correction for four comparisons), and in green if below $1.25 \cdot 10^{-2}$ (which is the 0.05 significance level after Bonferroni correction for four comparisons). As expected from the literature there is a significant decline in low frequency power in GM. However, changes in other masks are not significant. The regression of the baseline (Figure 3.13b) does not alter the significance levels of the age effect. However, if the respiratory components are regressed from the data we find a reduction in the p-value in

	GM	**WM**	**Arterial mask**	**CSF**
Noise baseline				
Initial $\langle\alpha\rangle \pm \sigma$	0.794 ± 0.036	0.913 ± 0.032	0.649 ± 0.052	0.725 ± 0.058
Refined $\langle\tilde{\alpha}\rangle \pm \sigma$	0.794 ± 0.036	0.913 ± 0.032	0.650 ± 0.052	0.722 ± 0.058
Initial R_α	0.951 ± 0.023	0.978 ± 0.010	0.918 ± 0.045	0.950 ± 0.036
Refined $\tilde{R}_\alpha$	0.951 ± 0.023	0.978 ± 0.010	0.918 ± 0.045	0.950 ± 0.036
Cardiac				
Initial $\langle\beta_c\rangle \pm \sigma$	0.100 ± 0.020	0.077 ± 0.020	0.240 ± 0.049	0.143 ± 0.039
Refined $\langle\tilde{\beta}_c\rangle \pm \sigma$	0.105 ± 0.020	0.082 ± 0.020	0.246 ± 0.050	0.149 ± 0.041
Initial R_c	0.443 ± 0.105	0.197 ± 0.079	0.734 ± 0.119	0.595 ± 0.103
Refined $\tilde{R}_c$	0.402 ± 0.10	0.162 ± 0.065	0.714 ± 0.122	0.560 ± 0.102
Respiratory				
Initial $\langle\beta_r\rangle \pm \sigma$	0.046 ± 0.019	0.043 ± 0.018	0.048 ± 0.020	0.060 ± 0.024
Refined $\langle\tilde{\beta}_r\rangle \pm \sigma$	0.049 ± 0.020	0.047 ± 0.019	0.049 ± 0.021	0.065 ± 0.024
Initial R_r	0.439 ± 0.156	0.226 ± 0.177	0.409 ± 0.171	0.623 ± 0.144
Refined $\tilde{R}_r$	0.361 ± 0.146	0.158 ± 0.148	0.345 ± 0.159	0.590 ± 0.145

Table 3.1: Initial and refined baseline, cardiac and respiratory regressor values and the ratio of significantly modulated voxels in different tissue masks. Regressor values in each voxel were weighted by the PVE value and normalised by the total mask volume as described in Eq.3.15. The values are the averages over all 21 subjects.

GM by more than ten-fold (Figure 3.13c). The additional regression of the cardiac components (Figure 3.13d) does not improve significance, but rather a subtle increase in the GM p-value is observed. In summary we find an enhancement of the age-effect for the fALFF if baseline noise and respiration are regressed, but a slight weakening of the effect if further cardiac fluctuations are removed. This suggests that the fALFF reduction with ageing might carry a pure vascular component, besides a decline in neuronal components.

Regressor values and spatial extent

The group average results for the individual regressors in the GLM are shown in Figure 3.14. The average values and the fraction of significantly modulated voxels R might help to interpret the results we obtained for the fALFF. The thermal noise baseline regressor values do not differ significantly (Figure 3.14a) in any mask. Almost every voxel in each mask has a constant baseline offset (R_α is close to 1) and there is no difference between the age groups. This is consistent with the insignificant effect of thermal noise regression from the fALFF. Taking a closer look at the respiratory parameters in Figure 3.14b we find a higher variance and a larger fraction of affected voxels within the older group. This explains the enhancement of the fALFF group difference when corrected for respiration. Most significant are the group differences in cardiac regressors in Figure 3.14c. In all masks, except for the arterial mask we find a reduction in β_c, suggesting weaker cardiac-induced signal fluctuations in the EPI signal for the older cohort. Although the β_c values are reduced in the older group, their spatial extent is significantly increased in WM. The age-related decline and increased spatial extent of cardiac-induced EPI

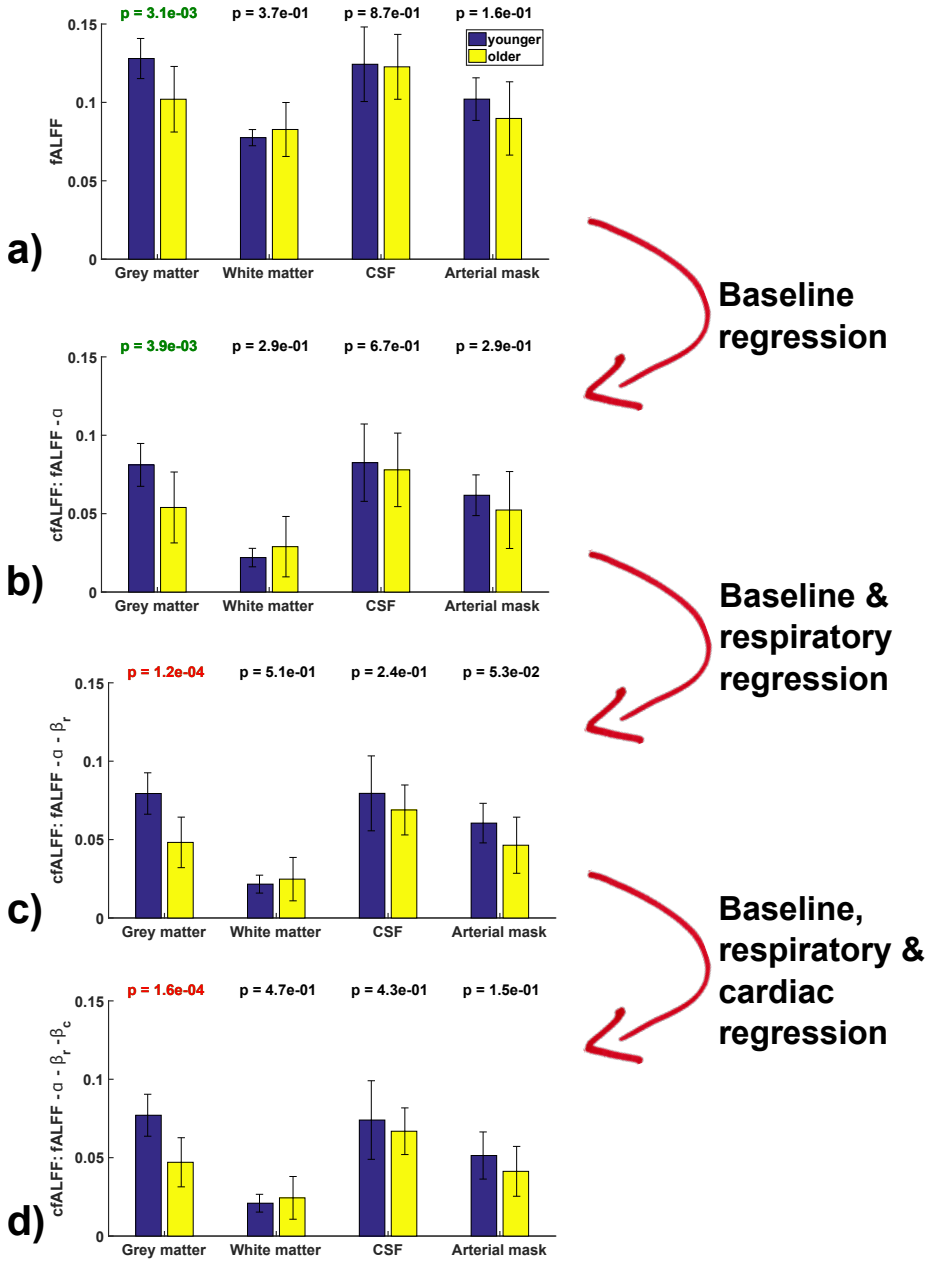


Figure 3.13: fALFF (a) and cfALFF results (b-d) in different tissues. The p-value refers to a two-sample t-test between the younger (blue) and older (yellow) age groups. Significant differences with $p < 1.25 \cdot 10^{-2}$ and with $p < 2.5 \cdot 10^{-3}$ are highlighted in green and red respectively, which are the Bonferroni-corrected 0.05 and 0.01 levels for four comparisons. a) "uncleaned" fALFF, **b)** cfALFF with noise baseline regression, **c)** cfALFF with baseline and respiratory component regression and **d)** cfALFF with a complete regression of all components.

fluctuations agrees with the cleaned fALFF results where a cardiac regression counteracted the age effect.

3.4.2.2 Cardiac frequencies: CEM and CPM

Figure 3.15 displays the results for the CEM measure. Recall that it is an efficiency measure, quantifying the amount of EPI power measured for a fixed amount of cardiac input power. Similar to the results for the cardiac regressor values β_c we find a reduced transmission of cardiac power with age. This is again significant in GM and WM and CSF, but not in the arterial mask.

Results for the CPM and modified CPM are displayed in Figure 3.16. Unfortunately we were not able to reproduce the results of Makedonov et al. [138]. They found a significant increase in CPM in WM which we cannot find in our data. However, we find a significant increase in CPM in the arterial mask in the older group, and the GM shows a trend with a p-value of 0.056. However, none of the p-values are significant against Bonferroni-corrected significance levels for the comparison in four masks. As already discussed in the Introduction and Methods, we suspect the CPM measure to dominantly reflect the width of the cardiac power spectrum, that is narrowed with age. This could explain why the CPM is in particular enhanced in the arterial mask with age. The average spectral power in the pulse-ox spectrum at the dominant frequency was almost doubled in the older group compared to the younger group ($0.6 \pm 0.2\%$ versus $0.33 \pm 0.08\%$). To further test for the effect we ran a partial correlation of the CPM versus age groups, while controlling for the power amplitude at the dominant frequency. In this analysis the CPM versus age effect is non-significant in any tissue mask.

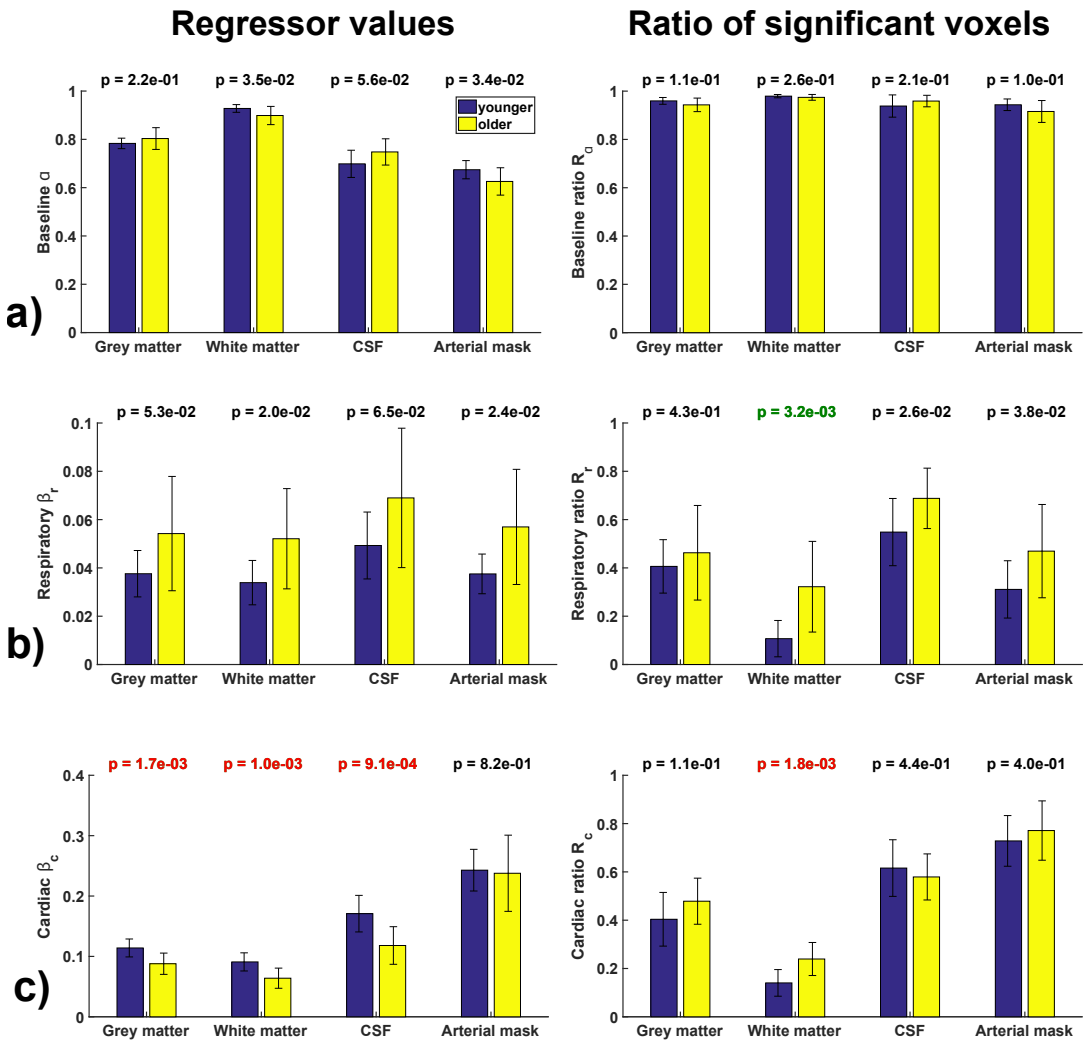


Figure 3.14: Group comparison of the GLM regressor values and the amount of significantly modulated voxels in different tissue masks. Significant differences with $p < 1.25 \cdot 10^{-2}$ and with $p < 2.5 \cdot 10^{-3}$ are highlighted in green and red respectively, which are the Bonferroni-corrected 0.05 and 0.01 levels for four comparisons. a) Noise baseline, **b)** respiratory regressor β_r and **c)** cardiac regressor β_c are plotted to the left and the corresponding fraction of affected voxels is displayed on the right.

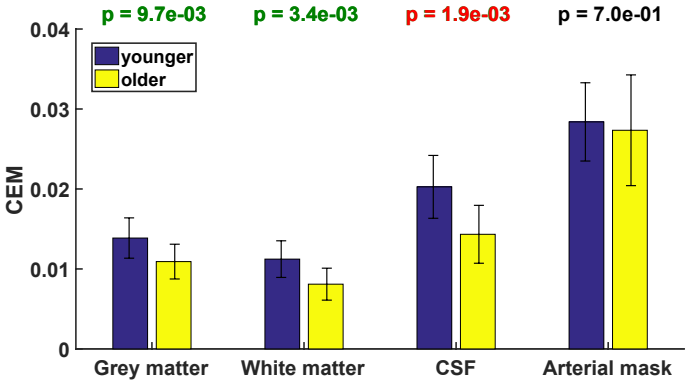


Figure 3.15: Tissue-specific CEM results for the younger (blue) and older (yellow) age groups. Significant differences with $p < 1.25 \cdot 10^{-2}$ and with $p < 2.5 \cdot 10^{-3}$ are highlighted in green and red respectively, which are the Bonferroni-corrected 0.05 and 0.01 levels for four comparisons.

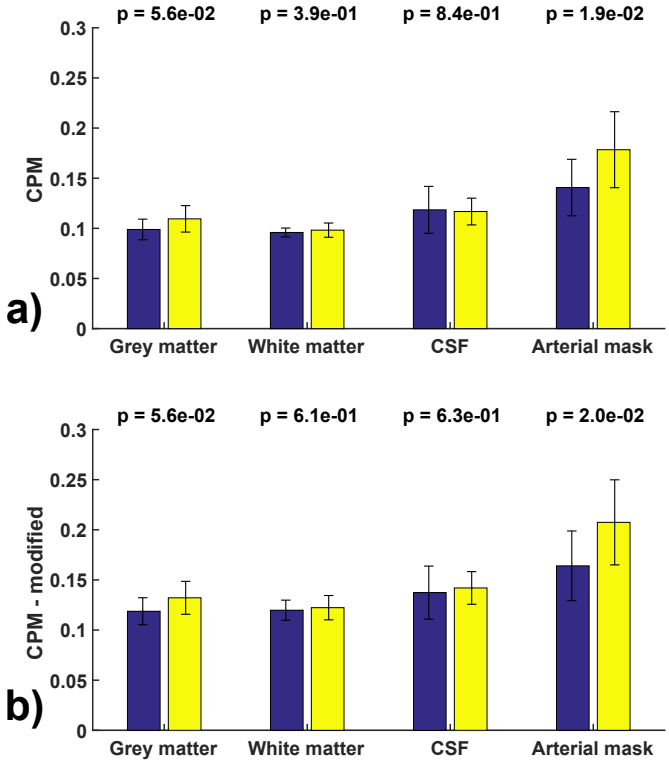


Figure 3.16: Tissue-specific CPM (a) and modified CPM (b) results for the younger (blue) and older (yellow) age groups. None of the group comparisons remained significant after Bonferroni-correction of the significance levels.

3.5 Discussion and conclusion

3.5.1 Initial vs. dual GLM

Summary of key findings.

- The cerebral cardiac spectrum has enhanced power at the dominant cardiac frequencies, but higher harmonics are filtered compared to an external pulse-ox spectrum measured at the finger tip.
- The cerebral respiratory spectrum amplifies low respiratory frequencies compared to the external spectrum. Chest expansion may not be an ideal representation of the multiple respiration-induced fluctuations.
- Dual regression cardio-respiratory maps are more sparse than maps of a simple GLM analysis.

We used a simple GLM and a refined dual regression to calculate baseline and cardio-respiratory regressor maps. The initial and refined baseline maps and spectra do not differ notably, affirming our model assumption of the frequency-independence of thermal noise. The spatial extent of the refined cardio-respiratory maps is reduced compared to the initial analysis. The reduction is likely due to voxels where variance is shared between explanatory variables in the initial GLM. The reduction in the ratio of respiratory modulated voxels is higher than for the cardiac case and dominant respiratory frequencies are downscaled and lower frequencies are scaled up. There are multiple uncertainties that make the respiratory spectrum from the BioPac

measurement not an ideal explanatory variable. The pad measures air pressure changes with chest expansion, but breathing variability induces local changes in B_0 and motion artefacts that are likely not linear. It has been shown that $PETCO_2$ -induced fluctuations in CBV and CBF account for unique variance in the BOLD fMRI signal (see also Introduction). These fluctuations are highly correlated with the respiratory rate and in particular the respiratory volume at each breathing cycle. An additional measurement of the $PETCO_2$ trace could be used to disentangle this effect which is currently picked-up indirectly by the respiratory belt. A spatial map of the $PETCO_2$ regressor (obtained for example with FSL Feat) could be plugged into the dual GLM (at the dual regression step), to remove the $PETCO_2$ component from the respiratory spectrum. The pulse-ox cardiac spectrum is similarly not an ideal template of cardiac frequency fluctuations in the brain and we found a gain in the refined spectrum at the dominant frequencies, and a filtering of lower power components and higher order harmonics. It is thought that cardiac pulsatility is filtered throughout the vascular tree, being a possible explanation of the reduced harmonics and lower power components.

3.5.2 Age-related changes

Low frequencies: fALFF vs. cfALFF

Summary of key findings.

- The fALFF is significantly reduced in GM with age.
- Thermal noise baselines do not show an age-dependence.
- The statistical significance of the fALFF decline with age is increased by more than an order of magnitude when respiratory components are regressed.
- The statistical significance of the fALFF decline is reduced slightly when cardiac components are regressed.
- Cardiac-induced fluctuations are significantly weaker in the older group. The spatial extent, however, is increased with age and significantly affects more voxels in WM.

The reduction in fALFF and cfALFF with age in GM is highly significant, but the fALFF does not offer a clear explanation of the underlying mechanisms. Neuronal or vascular decline could be the origin of the power reduction and it is likely a combination of both. However, the decrease in cardiac-induced EPI fluctuation power (β_c) suggests that a vascular component might be involved, linked to low frequency cardiac fluctuations such as heart rate variability or Meyer waves. We cannot deduce a difference in vasomotion from the data as the external cardiac spectrum should not pick up these fluctuations. We further found a significant increase in the respiratory-induced EPI magnitude with age. We cannot offer a physiological rationale

behind this observation besides the possibility that older subjects might move more during breathing.

Cardiac frequencies: CEM and CPM

Summary of key findings.

- The CEM results suggest an age-related efficiency reduction of cardiac power transmission into the brain. This observation was significant in all tissue types, except the arterial mask.
- The age-related increase in the CPM is likely to be explained by an age-dependent narrowing of the cardiac peak power width and not by vascular effect.

Compared to the fALFF, that has been used in the literature frequently, there is no compatible measure of cardiac power in the brain. To our knowledge, only the CPM measure from Makedonov et al. [138] has aimed to quantify cardiac pulsation in normal ageing. The CPM measures average cardiac power over a fixed frequency range. We suspected that this may not be the most appropriate measure to investigate the impact of age-related changes in cerebral pulsatility, given that cardiac spectra vary strongly with age. We therefore introduced the CEM that calculates the transmitted EPI power for a fixed input power and is an efficiency measure. For this measure we found a decrease with age in all tissues, except for the arterial mask.
The CEM results are in accordance with the β_c findings where we found a decline with age. Again, reduced blood flow, and changes in arterial wall properties could affect CBF and CBV pulsatility that cause the decline in cardiac EPI signal fluctuations with age.

Hypothesis on the age effects

Cerebrovascular properties are known to change with age, for example absolute CBF decreases with age [146, 147], however CBF pulsatility has been reported to increase [148], i.e. the relative blood flow velocity difference between systole and diastole is higher in the older population. Besides, the age-related change in CBF, a decrease in CBV pulsatility has been reported [149]. It is thought that age-related arterial stiffening alters the ability of the vasculature to dilate and constrict, causing a decrease in CBV fluctuation and hence an increase in CBF fluctuation. Here, we observed a reduction in the fALFF, the cardiac regressor β_c and the CEM with age. All of these three measures reflect changes in CBV and CBF. As all three variables declined we suspect that they mainly reflect CBV changes with neuronal activity in the case of the fALFF and cardiac-driven in case of the cardiac regressor value and the CEM. Besides the reduction in β_c with age we also observed an increase in the spatial extent of voxels that show a cardiac modulation in their EPI power spectra. With a hypothetical reduction in wall compliance we would expect the cardiac pressure wave to travel further down the arterial tree and potentially explaining this observation.

To test if the age-related changes we observed are a reflection of CBV pulsatility differences between the age groups it would be useful to run a CO_2 challenge in a cohort of similar aged younger subjects. CO_2 is a vasodilator and causes CBV changes. If there is a significant change in the cardiac regressor β_c and potentially in the spatial extent of the cardiac regressor maps it would be an indicator that they measure CBV pulsatility.

3.5.3 Critical points

The sample size of 21 subjects is too small to draw firm conclusions and results should be treated as indicators. RF-inhomogeneity is pronounced at 7T and could introduce subject-specific variations in the data. Further we used a rather large voxel size of $3 \times 3 \times 3$ mm^3 which leads to partial volume effects. We tried to mitigate this by weighting values by the PVE and disregarding mixed tissue voxels (thresholding at a PVE of 0.7). However, with increased atrophy GM masks of older subjects are smaller, introducing more uncertainty in the average values. The same holds for the arterial masks, which tend to be larger for the younger subjects.

3.5.3.1 Normalisation

A general weakness of the low frequency fALFF and cardiac CEM and CPM measures is a coupling effect between them. This is introduced by the normalisation of the power spectra. High cardiac regime power will suppress low frequency neurovascular power and vice versa. However, as discussed in the Introduction, a normalisation is needed in order to compare subjects. Here, we found an age-related reduction in both - the low frequency fALFF as well in the CEM. The noise baseline was not significantly different between the groups, but respiratory regressors were higher in the older group. As mentioned in the discussions above, there is to our knowledge no age-related respiratory phenomenon that could explain this difference. It is quite likely that it is the effect of the normalisation that causes an enhancement of the respiratory regressors in the older group.

Chapter 4

Origins and mechanisms of cardiac-frequency signal fluctuations in brain MRI time series data

This chapter is in large parts based on a manuscript submitted to the journal *NeuroImage* under the title "Origin and Mechanisms of Cardiac-Frequency Signal Fluctuations in Brain MRI Time Series Data" and is currently under review.

4.1 Introduction

4.1.1 The arterial pressure wave in the brain

A schematic picture of the arterial pressure wave over the course of the cardiac cycle is provided in Figure 4.1. The wave originates in the heart and is

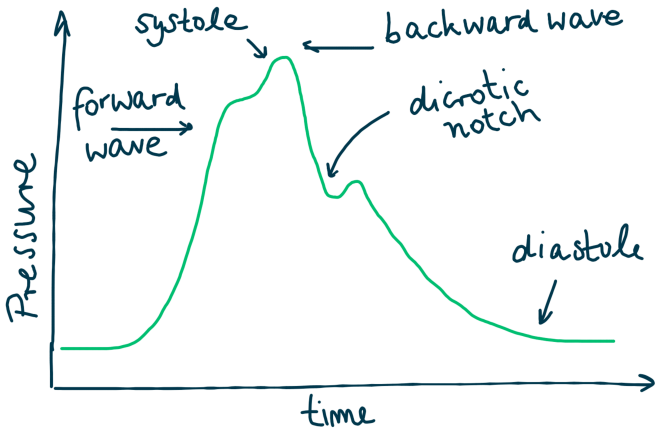


Figure 4.1: Schematic arterial pressure waveform. The forward travelling pressure wave is reflected through the vasculature and peaks at systole, followed by a decrease towards the lowest point at diastole. Backwards travelling waves create "dicrotic notch-like" dips in the waveform.

reflected through the vasculature. The ascending interval is the *systole* and maximum systolic pressure occurs at the point where forwards and backwards travelling waves meet. The trough in the waveform is the *diastole*. Dips occur between systole and diastole and either present the dicrotic notch (closure of the aortic valve) or reflected waves. The discernibility and timing of the dicrotic notch and reflected waves depend on which level of the vascular tree the waveform is measured at. The cardiac pressure wave propagation speed is reported to approximately follow the equation: velocity = $0.07 \times$ systolic pressure [mmHg] $+ 0.09 \times$ age $- 4.3\,\mathrm{m/s}$ [150]. This is a range of a few to 10 m/s in healthy adults. The spatial wave propagation in the brain can therefore be regarded as instantaneous in MRI as it is beyond the temporal resolution achievable. However, the pressure wave is coupled to local changes in CBF, CBV and CSF dynamics that can be measured with MRI [151]. Being confined by the skull the brain is termed a "low compliant system" compared to other organs, and in- and outflow and movement of tissue compartments must be tightly coupled. Compliance is defined as the pressure change induced by a given increase in volume [152]. The overall cerebral compliance is a combination of vascular compliance - the ability of

the arteries and veins to dilate and constrict through the systole-to-diastole cycle, tissue compliance and CSF dynamics. Often these terms are also alternatively referred to as vascular resistance and tissue resistance. Compliance transforms pulsatile arterial blood flow into a constant blood supply to the capillaries. The level of compliance will dictate how much cardiac pulsatility is transferred down the vascular bed and into tissue.

4.1.2 Means of measuring cerebral pulsatility

A direct measure of the arterial pressure wave can be achieved by intracranial pressure monitoring (ICP). It is an invasive technique whereby a pressure sensor is placed in the brain tissue, a CSF space or into an artery using a catheter-tip transducer [153, 154]. ICP does not yield further insights into differences in vascular and tissue compliance. Indirect measures of the arterial pressure wave are transcranial Doppler sonography (TCD) and MRI which are sensitive to flow changes. In TCD an ultrasound probe is placed in the temporal area (temporal window). This method provides the velocity profile over the cardiac cycle in the larger cerebral arteries accessible from that position, usually the MCA and the anterior and posterior cerebral arteries [155, 156]. A standard measure derived from the data is the pulsatility index (PI), which is the difference between the maximum (systolic) and minimum (diastolic) velocities, normalised by the mean velocity over the cardiac cycle. TCD is economically efficient and easy to perform, however MRI offers 3D information and a whole-brain coverage.

4.1.2.1 MR methods to study cerebral pulsatility

Quantitative velocity information with MRI is achieved by phase-contrast MRA (PC-MRA) sequences. PC-MRA applies two gradients of opposite

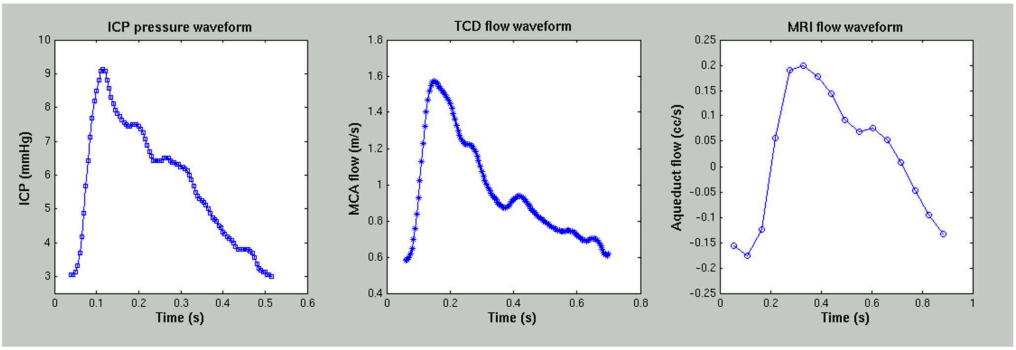


Figure 4.2: Comparison of the arterial waveforms as measured in ICP (left), TCD (middle) and PC-MRA (right). The ICP and TCD waveforms are measured over a single cardiac cycle, whereas the MR based waveform is the average over multiple cycles. Figure taken from Wagshul et al. [151] with permission.

amplitude twice to encode for velocity. Static tissue spins will acquire a zero net phase over the bi-polar gradients, whereas moving blood spins will have a non-zero phase that is directly proportionate to their velocity, up to a maximum velocity (known as venc) where phase aliasing occurs [57, 157]. The two phase images are subtracted to derive the absolute velocity from the phase change. Using cardiac gating strategies from cardiac cine-MRI, PC-MRA has already been used in the early 90s to measure CSF velocities at multiple points of the cardiac cycle [158, 159]. With 3D PC-MRA and stronger gradient systems being developed, 4D flow PC-MRA [160] has become a means of studying blood flow over the course of the cardiac cycle [161]. Figure 4.2 compares the waveforms obtained by the three standard measurement techniques ICP, TCD and PC-MRA [151]. The MRI based waveform is broader than the other two methods as it is an average over many cardiac cycles, whereas ICP and TCD are single-cycle measurements as they have significantly higher temporal resolution. Besides the phase contrast-based techniques there has, to our knowledge, only been three alternative MR methods applied to investigate cerebral pulsatility and compliance. Yan

et al. [162, 163] measured vascular compliance by definition as the change in CBV between systole and diastole, divided by the pressure difference. They used a dynamic SSFP-based arterial spin labelling sequence that was synchronized to the cardiac cycle and simultaneously measured blood pressure with an MR compatible cuff sphygmomanometer. More similar to our approach Bianciardi et al. used high-temporal resolution EPI with simultaneous cardiac signal recording [164]. They used a 2D-EPI sequence with TRs of a few tens of milliseconds, measuring a single slice time series over 20 seconds before stepping to the next slice. They define a compliance measure, termed the pulsatility volume index, as the signal difference during systole and diastole in an ROI in large arteries like the carotid. Warnert et al. used pulsed ASL with short inversion times (250-850 ms) to measured arterial blood volume over the course of the cardiac cycle in conjunction with an MR-compatible blood pressure measurement [165, 166]. This set up allows them to measure the arterial blood volume change for a given blood pressure change from systole to diastole.

4.1.3 Clinical relevance of cardiac pulsatility

Although absolute CBF is known to decrease with age [146, 147], CBF pulsatility increases [148]. It is thought that age-related arterial stiffness limits the ability of the vasculature to dilate and constrict, causing a decrease in CBV pulsatility and an increase in CBF pulsatility [149]. Webb et al. measured the PI in the MCA with TCD and white matter hyperintensities with MRI in a group of leukoaraiosis patients [167]. They found a positive correlation between MCA PI and the amount of white matter hyperintensities. This supports the theory of an enhanced transmission of arterial pulsatility causing downstream tissue damage if vascular stiffness is increased.

4.1.4 Scope of this work

EPI with multiband sampling achieves temporal resolution in the sub-second regime whilst maintaining a good slice coverage and spatial resolution [94–96]. In combination with improved SNR and contrast mechanisms at ultra-high magnetic field, these fast acquisition techniques facilitate the study of spatio-temporal phenomena at finer scales and higher frequencies [98]. The ability to depict higher frequency regimes without alias turns cardiac-induced fluctuations, typically recorded as nuisance signal in EPI time series [144, 168], from "physiological noise" into a valuable signal that may carry information about cerebrovascular mechanisms. So far, studies have addressed the spatial pattern of cardiac-related fluctuations in EPI data [107, 169, 170] and we investigated age-related variations in BOLD power at the cardiac frequency in the previous chapter. However, little is known about tissue-specific contrast mechanisms that produce the observed variations in the signal.

As mentioned above vascular and tissue compliance and CSF dynamics transform pulsatile arterial blood flow into a stable blood supply to the capillaries. These "pulsatility" mechanisms are likely to contribute to the observed EPI signal fluctuations. Whole-brain EPI offers the ability to study pulsatility not just in resolvable arteries, but also on a sub-voxel spatial scale, and could potentially provide insights into the hypothesised link between age-related vascular stiffening and the impact of pulsatility changes on tissue [149, 167]. A profound understanding of the underlying MR-mechanisms of the observed EPI signal fluctuations at the cardiac frequency is a first step towards that goal.

This work aims to investigate the mechanistic sources originating in the car-

diac waveform that lead to fluctuations in the EPI signal. When run as a gradient-recalled echo (GRE) sequence, EPI offers two variables for quantification: the "zero-echo time" signal, S_0, and the effective transverse decay constant, T_2^*.

We begin with a Theory section to discuss:

- If cardiac-induced shear waves are detected in our data.
- How cardiac pulsatility affects S_0 and T_2^* and estimate how large we expect these changes to be.
- How variations of S_0 and T_2^* over the cardiac cycle cause temporal shifts, i.e. a phase change, in the EPI signal.

We then describe our experimental and analysis methods in the Methods section to discuss:

- How single-echo multiband EPI data can be used to create cardiac phase maps.
- How multi-echo multiband EPI data can be used to quantify S_0 and T_2^* values over the cardiac cycle in different tissues and brain areas.
- A voxel model of dynamic partial volumes to simulate the measured T_2^* waveforms.

For the remainder of this text we will refer to "pulsatility" as the fluctuation of a variable (CBF, CBV, S_0, T_2^* etc.) around its mean value over the course of the cardiac period. We will further use the term "phase" exclusively to denote a position within the cardiac cycle of such fluctuations.

4.2 Theory

Differences in the relative phase offset of the EPI signal at two voxel locations, both of which are fluctuating at the cardiac frequency, can be caused by two scenarios: a temporal delay in the underlying mechanical phenomenon (pressure and shear wave) or differences in S_0 and T_2^* fluctuations.

4.2.1 Shear wave-induced displacement

As mentioned in the Introduction, the pressure wave propagation speed is beyond the temporal resolution of EPI time series. However, the pressure wave is followed by a slower planar shear wave that travels radially outwards from the pulsating vessel wall and could cause inter-voxel displacement. The shear wave propagation speed, c_s, can be approximated (for wave frequencies of a few Hertz) using the shear modulus, G, and the tissue density, D, via [171]

$$c_s \approx \sqrt{G/D} \tag{4.1}$$

Assuming two identical voxels (i.e. of the same tissue composition), spatially separated by a distance Δr, we can calculate a potential signal delay, Δt, between the voxels $\Delta t = \Delta r / c_s$. As G is load-dependent, we extrapolate measured values from Rashid et al. [172], who measured G for brain tissue specimens at rates of $30, 60$ and 90 Hz, to a typical heart beat frequency of 1 Hz. Assuming a tissue density of $10^3\,\mathrm{kg/m^3}$, we find $c_s \approx \sqrt{5.45 \cdot 10^3\,\mathrm{Pa}/(10^3\,\mathrm{kg\ m^{-3}})} \approx 2.33\,\mathrm{m/s}$. Expecting shear waves to occur over a distance of a few millimetres, for example $\Delta r = 1\,\mathrm{cm}$, this would lead to a temporal shift $\Delta t \approx 4\,\mathrm{ms}$. This is far beyond the Nyquist frequency for EPI acquisitions, that typically sample at a few hundred milliseconds. We there-

fore conclude that we cannot detect shear wave-induced displacements in current EPI time series. However, techniques such as MR-encephalography, might offer the needed sample rates to study this phenomenon [173].

4.2.2 S_0 and T_2^* fluctuations

Let τ_c be the systole-to-systole time period that spans the *cardiac unit cycle* τ with $\tau \in (0, ..., \tau_c]$. The EPI signal over this period is then given by

$$S(\tau) = S_0(\tau) \cdot \exp\left\{\frac{-\mathrm{TE}}{T_2^*(\tau)}\right\}, \tag{4.2}$$

with TE being the echo time. $S(\tau)$ pulsatility should be derivable by $S_0(\tau)$ and $T_2^*(\tau)$ pulsatility.

4.2.2.1 S_0

$S_0(\tau)$ depends on multiple factors, as recently described in the work of Bianciardi et al. [164], and can be written as $S_0(c(\tau), \nu(\tau), T_1, M_0, \mathrm{TR}, \alpha)$, with T_1 being the longitudinal relaxation constant, M_0 the equilibrium magnetisation, TR the repetition time and α the flip angle. Relevant here are $c(\tau)$ and $\nu(\tau)$. $c(\tau)$ is the amount of existing RF-excited spins being replaced with fresh ones and, therefore, depends on a combination of CBF and CBV pulsatility in the voxel. Here and for the remainder of the text we refer to CBF as the blood flow velocity in a voxel. CBF pulsatility will only affect $c(\tau)$, and hence $S_0(\tau)$, if the spins flowing at a velocity ν experience multiple RF-excitations. In a classical single-slice acquisition, the critical speed is given by the minimum speed to traverse the slice of thickness Δz within TR ($\nu < \nu_{crit} = \Delta z/\mathrm{TR}$). For multiband acquisitions, this simple linear relationship does not apply due to the slice acquisition order. A critical speed

cannot be defined and slower spins might experience fewer RF-pulses than faster ones if their position is out of synchrony with the slice order. A simulation of the experienced number of RF-excitation for different velocities and slice positions for the acquisition parameters used in our study (slice thickness of $\Delta z = 2.2$ mm, TR of 320 ms, MB = 4 and the associated slice timing) is provided in Figure 4.3. This simulation is oversimplified and realistically the blood spins travel with changing velocities through a complex vascular path through the imaging slab. We notice that for a velocity of $\nu > 10$cm/s only few velocities have been excited multiple times. Voxels with higher velocities will only have S_0 fluctuations due to changes in CBV, but not CBF. Vessels with lower velocities will show S_0 fluctuations that could arise from both CBV and CBF. Table 4.1 lists literature values for flow velocities at different levels of the cerebrovascular tree. From these values we expect S_0 pulsatility in the major arteries such as the MCA, and also the veins, to be exclusively induced by CBV changes as velocities are fast enough to escape the imaging slab within one TR. For the smaller arteries, arterioles and capillaries a mixed effect of CBV and CBF pulsatility is expected.

4.2.2.2 $\mathbf{T_2^*}$

The effective transverse decay constant T_2^* of a GRE signal

$$T_2^{*-1} = T_2^{-1} + T_2'^{-1} \tag{4.3}$$

is a combination of the spin-spin relaxation time T_2, which is an inherent tissue property and T_2' an additional decay caused by a dephasing effect in the presence of local field inhomogeneities [179]. As such T_2^* is sensitive to the BOLD effect, that was reported first by Ogawa et al. in 1990 [99].

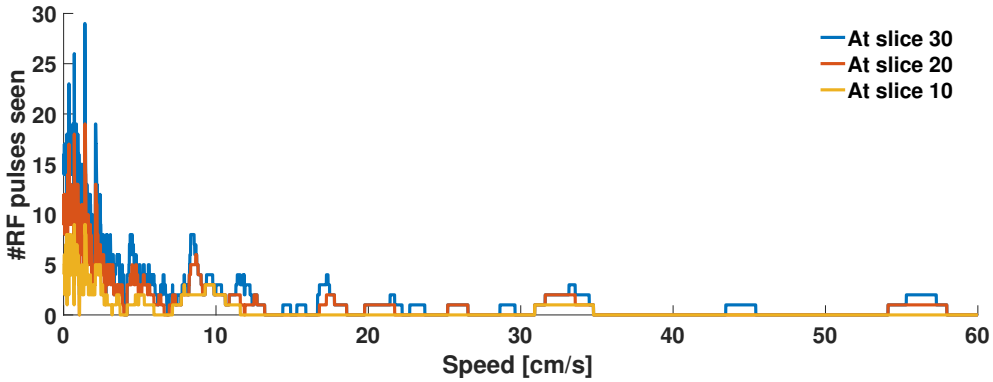


Figure 4.3: The number of RF-excitations experienced for a spin travelling at different speeds at different slice locations. This simulation refers to a slice thickness of 2.2 mm, an MB factor of 4 and the according slice timing and a TR of 320 ms. The simulation assumes a straight travelling path through the imaging slab, which is an oversimplification as realistically a blood spin travels at varying velocities through a complex vascular path through the imaging slab.

Vascular compartment	**flow velocity, systole (max)/ diastole (min) [cm/s]**
MCA [174]	56.2-115/38.3-44.7[a]
basilar artery [174]	35.1-77.0/25.9-56.0[a]
ICA [174]	38.4-72.0/20.9-43.0[a]
lenticulostriate arteries [175]	9.6/-
arteries in basal ganglia [176]	5.7/3.3
arteries in semioval centre [176]	0.82/0.44
sagittal sinus anterior [177]	16/-
sagittal sinus posterior [177]	31/-
CSF compartment	
Aqueduct of Silvius [72, 73]	4-5/-
3^{rd} ventricle [178]	0.37/-
4^{th} ventricle [178]	0.38/-

Table 4.1: Literature values for systolic and diastolic flow velocities from the major arteries to the veins and in CSF.
[a] Values vary significantly within the literature and here we quote the range of systolic (maximum) and diastolic (minimum) velocities that were summarised in the work of Bammer et al. [174].

The underlying mechanism is a structural change of the haemoglobin (Hb) molecule between the oxygenated and deoxygenated state. The susceptibility of Hb changes from diamagnetic to paramagnetic upon oxygen unbinding as an iron atom becomes unshielded.

Although we measure the voxel's GRE signal as a single-exponential decay (Eq. 4.2), its underpinning is a combination of intra- and extravascular signals. A multi-exponential model has been introduced for neuro-vascular signals by Obata et al. and refined by Uludag et al. [180,181]. We can adapt this model to incorporate the two mechanisms that could lead to a variation in $T_2^*(\tau)$: a variation in oxygen saturation Y and/or in the partial volumes v_i:

$$S_{multi}(\tau) = \sum_i v_i(\tau) \cdot \rho_i \cdot M_{z,i} \cdot \exp\left\{\frac{-\mathrm{TE}}{T^*_{2,i}(Y(\tau))}\right\}, \tag{4.4}$$

with i = parenchyma, arterioles, capillaries, venules, CSF. ρ_i and $M_{z,i}$ are the respective proton densities and longitudinal magnetisations.

- *Variations in oxygen saturation* $Y(\tau)$

  Arterial oxygen levels are close to 100%. Oxygen extraction during neuronal activation already commences to a minor degree at the arteriolar levels [181], but oxygen extraction, to satisfy the bulk of baseline metabolism, is thought to start in the capillaries. This view has recently been challenged by a two-photon microscopy study of partial O_2 levels in the rat cortical microvasculature by Sakadzic et al. [182] who found that about half of the baseline oxygen extraction occurs in parenchymal arterioles, in contrast to the dominant capillary extraction of oxygen upon neuronal activation. To estimate the magnitude of hypothetical

[0]The semioval centre is located in the white matter, underneath the cortex.

changes in Y, we calculated expected ΔT_2^* values at 7T arising from variations between Y=0.96 and Y=1. We extrapolated values obtained in a 3T study of arterial T_2^* [183] to typical hematocrit (Hct) levels of large arteries (Hct=0.41 [184]) and microvessels (Hct=0.36 [185]). Further we multiplied the values by 0.67 to account for the decrease in T_2^* from 3 to 7T as described previously [64]. We modelled a voxel entirely filled with arterial blood, as well as parenchyma voxels, where we used the multi-exponential signal model (Eq. 4.4). We assume that the measured mono-exponential signal S can be approximated as $S \approx S_{multi}$ to derive the voxel's apparent T_2^*. ΔT_2^* was estimated for voxels within the cortical grey matter (cGM), deep grey matter (dGM) and white matter (WM) using blood volume fractions of $v = 0.055/0.042/0.021$ respectively [186]. Assumed proton densities were $\rho_{blood} = 0.87$ [187], $\rho_{\mathrm{cGM}} = \rho_{\mathrm{dGM}} = 0.89$ and $\rho_{\mathrm{WM}} = 0.65$ [57]. $M_{z,i}$ were calculated as the steady-state signals of a spoiled GRE sequence with the flip angle and TR as in our multi-echo protocol ($\alpha = 90°$, TR = 405 ms, see protocol description in 4.3.4) and 7T values of $T_1 = 2562/2132/1220$ ms for blood, GM and WM respectively [31]. We used absolute T_2^* values of 29 ms (cGM and dGM) and 25 ms (WM), which are the measured values we found in our multi-echo experiments (see Results section, Table 4.4). The average TE from our experimental protocol (36.75 ms) was used in Eqs. 4.2 and 4.4.

The final estimated range of expected ΔT_2^* is provided in Table 4.2. Summarising the table we expect ΔT_2^* in a pure arterial voxel to be between $\approx 2.9 - 11.3\%$ for all possible fluctuations between $Y = 0.96 - 1.00$. For cGM this is $\approx 0.14 - 0.56\%$, for dGM $\approx 0.10 - 0.42\%$ and

Oxygenation variation $[Y_{min} - Y_{max}]$	**Estimated** $\mathbf{\Delta T_2^*}$[%]			
	Arterial blood	Cortical grey matter	Deep grey matter	White matter
0.96 – 1.00	11.34	0.56	0.42	0.19
0.97 – 1.00	8.59	0.41	0.32	0.14
0.98 – 1.00	5.78	0.27	0.21	0.09
0.99 – 1.00	2.92	0.14	0.10	0.05
0.96 – 0.99	8.67	0.42	0.32	0.14
0.97 – 0.99	5.84	0.28	0.21	0.09
0.98 – 0.99	2.95	0.14	0.11	0.05
0.96 – 0.98	5.89	0.28	0.21	0.09
0.97 – 0.98	2.98	0.14	0.11	0.05
0.96 – 0.97	3.00	0.14	0.11	0.05

Table 4.2: Estimates of oxygenation fluctuation-induced changes in T_2^* for a pure arterial voxel, grey matter, deep grey matter and white matter, extrapolated from reported values in a 3T study [183].

for WM $\approx 0.05 - 0.19\%$.

- *Variations in partial volume* $v_i(\tau)$

  $T_2^*(\tau)$ is most likely affected by variations in $v_i(\tau)$ due to CBV changes. A detailed model including $v_i(\tau)$ to simulate $T_2^*(\tau)$ is described in the Methods (see section 4.3.3).

4.2.2.3 Effect of S_0 and T_2^* fluctuations on the signal phase

Here we explore how variations in the magnitude and timing of $S_0(\tau)/T_2^*(\tau)$ might affect the signal. All simulations in this section were performed in MATLAB, R2016a (The MathWorks, Inc., Natick, MA, USA).

For simplicity, we assumed sinusoidal waveforms for $S_0(\tau)/T_2^*(\tau)$. While this does not capture all features of a realistic waveform, it allows us to derive some analytical expressions for a more intuitive understanding. We note that any continuous and periodic function can be expanded into a Fourier series, that is a realistic waveform can be decomposed into a sum of sine and cosine functions. These individual terms are well described by our simple model.

Thus, our results can be readily generalized by considering the superposition of the contributions from many sinusoidal fluctuations.

$$S_0(\tau) = \overline{S_0} \cdot \left\{ 1 + S_{0,p} \cdot \cos\left[\frac{2\pi}{\tau_c}(\tau - \tau_{max,S_0}) \right] \right\}, \tag{4.5}$$

$$T_2^*(\tau) = \overline{T_2^*} \cdot \left\{ 1 + T_{2,p}^* \cdot \cos\left[\frac{2\pi}{\tau_c}(\tau - \tau_{max,T_2^*}) \right] \right\}, \tag{4.6}$$

with $\overline{S_0}$, $\overline{T_2^*}$ being the mean values; $S_{0,p}$, $T_{2,p}^* \in [0, 1]$ being the maximum normalized amplitude of fluctuation (i.e. pulsatility) and τ_{max,S_0}, τ_{max,T_2^*} being the time point when the maximum amplitude of fluctuation is reached. Substituting the waveforms (Eqs. 4.5 and 4.6) into the EPI signal (Eq. 4.2), we find that only changes in the amplitude $\overline{S_0}$ conserve the signal phase. Taking the derivative of Eq. 4.2 w.r.t. $\overline{S_0}$, we get an amplitude scaling factor, but the period remains the same:

$$\frac{\mathrm{d}S(\tau)}{\mathrm{d}\overline{S_0}} = \frac{S(\tau)}{\overline{S_0}}. \tag{4.7}$$

As $S(\tau)$ has an exponential dependence on T_2^*, the same does not apply for variations in absolute $\overline{T_2^*}$ values:

$$\frac{\mathrm{d}S(\tau)}{\mathrm{d}\overline{T_2^*}} = S_0(\tau) \cdot \exp\left\{ \frac{-\mathrm{TE}}{T_2^*(\tau)} \right\} \cdot \frac{\mathrm{TE}}{T_2^*(\tau)^2} \cdot \frac{\mathrm{d}T_2^*(\tau)}{\mathrm{d}\overline{T_2^*}} = S(\tau) \frac{\mathrm{TE}}{\underbrace{T_2^*(\tau)}_{\text{shift}}\overline{T_2^*}}, \tag{4.8}$$

and two voxels with different T_2^* will produce temporally shifted GRE signals as simulated in Figure 4.4a for exemplar GM and WM T_2^* values of 29 vs. 25 ms (all other waveform variables in Eqs. 4.5 and 4.6 were kept constant). Another relevant case is a variation in pulsatility amplitude. The derivative

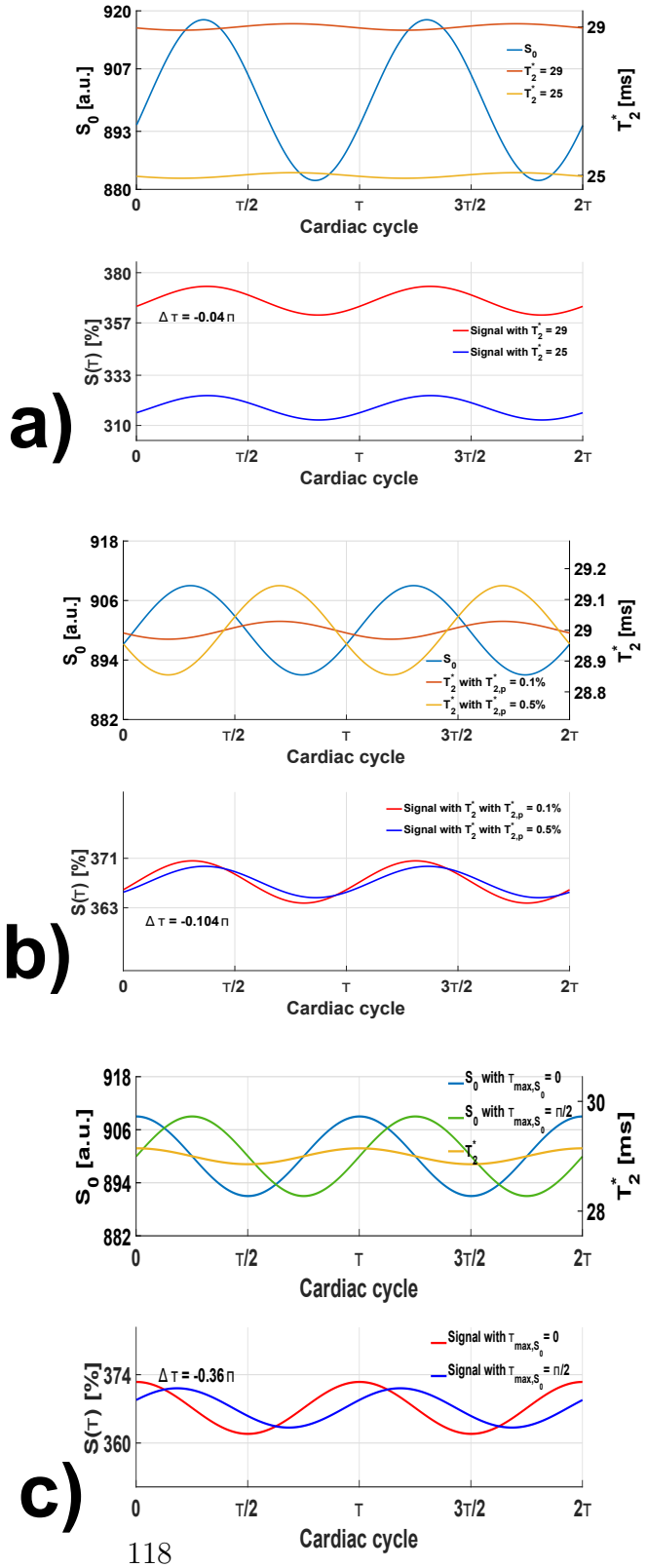


Figure 4.4: Simulated $S_0(\tau_c)$ and $T_2^*(\tau_c)$) waveforms (top) and their EPI signals (bottom). **a)** EPI signals for a constant $S_0(\tau_c)$, and two $T_2^*(\tau_c)$ that differ in their absolute T_2^* value (29 vs. 25 ms). **b)** EPI signals for the same $S_0(\tau_c)$ and two $T_2^*(\tau_c)$ that differ in their amount of fluctuations $T_{2,p}^*$ (0.5 vs. 0.1%). **c)** EPI signals for a variation in the timing of $S_0(\tau_c)$ and $T_2^*(\tau_c)$ relative to each other with $S_0(\tau_c)$ being shifted by $\pi/2$.

of Eq. 4.2 w.r.t. $T_{2,p}^*$ indicates phase shifts in the signal:

$$\frac{\mathrm{d}S(\tau)}{\mathrm{d}T_{2,p}^*} = S(\tau)\frac{\mathrm{TE}}{T_2^*(\tau)^2} \cdot \overline{T_2^*} \cdot \cos\left[\frac{2\pi}{\tau_c}(\tau - \tau_{max,T_2^*})\right]. \tag{4.9}$$

Figure 4.4b shows a simulation for the case of $T_{2,p}^* = 0.1\%$ vs. $T_{2,p}^* = 0.5\%$ where we notice a shift in the signal phases. The case of $S_{0,p}$ variations is similar and not further described here. Finally, a relative timing between S_0 and T_2^* also can lead to temporal shifts. The derivative of Eq. 4.2 w.r.t. τ_{max,S_0} is

$$\frac{\mathrm{d}S(\tau)}{\mathrm{d}\tau_{max,S_0}} = \overline{S_0} \cdot S_{0,p} \cdot \frac{2\pi}{\tau_c} \sin\left[\frac{2\pi}{\tau_c}(\tau - \tau_{max,S_0})\right] \cdot \exp\left\{\frac{-\mathrm{TE}}{T_2^*(\tau)}\right\} \tag{4.10}$$

as shown in Figure 4.4c where two signals are simulated once with T_2^* and S_0 in synchrony, and once with them shifted by a quarter of the cardiac cycle relative to one another. Note that the change in the phase relationship between $T_2^*(\tau)$ and $S_0(\tau)$ not only induces a temporal shift, but also impacts the absolute signal amplitude!

In summary, there is no simple bijective relation between the cardiac cycle-related signal phase and the parameters of the $S_0(\tau)/T_2^*(\tau)$ fluctuation waveforms. Further, the signal amplitude depends on the phase relationship between the $S_0(\tau)$ and $T_2^*(\tau)$ waveforms even if their mean values and pulsatility are identical. Vice versa, the phase of the EPI signal can be shifted by variations in the $S_0(\tau)/T_2^*(\tau)$ mean values and pulsatility even if the timing of both waveforms is the same (i.e. without a "delay").

4.3 Methods

4.3.1 Cardiac phase mapping

The phase of the EPI signal yields information about the relative timing of the signal with respect to a reference signal. We calculated each voxel's phase ϕ_c at the cardiac frequency f_c following these steps:

1. An external cardiac signal (e.g. pulse-oximetry) is measured during fMRI acquisition. It is down-sampled to TR and then Fourier-transformed to obtain the expected cardiac power spectrum. The cardiac frequency f_c is then defined as the component with the maximum power amplitude as shown in Figure 4.5.

2. The EPI time series $S(t)$ is Fourier-transformed into the frequency domain to yield $\tilde{S}(f)$.

3. An arbitrary voxel r is selected to serve as a fixed phase reference. The reference voxel can be chosen arbitrarily at this stage. In a later step the phases are referenced to a particular phase value from an arterial mask (see Post-processing for further details).

4. The phase $\phi_{c,i}$ at voxel i is calculated as the angle between the complex vectors:

$$\phi_{c,i} = \arctan\left[\frac{Im\{\tilde{S}_i(f_c)/\tilde{S}_r(f_c)\}}{Re\{\tilde{S}_i(f_c)/\tilde{S}_r(f_c)\}}\right] + \phi_{i,r} \tag{4.11}$$

   with

$$\phi_{i,r} = 2\pi f_c \, \Delta t_{i,r},$$

   where $\phi_{i,r}$ is the phase shift induced by the timing offset $\Delta t_{i,r}$ in the acquisition between the slices of voxel i and the reference voxel r. $\Delta t_{i,r}$

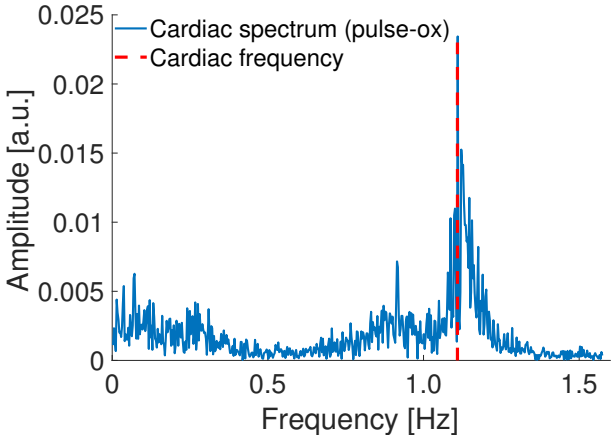


Figure 4.5: An example spectrum of the peripheral cardiac recording after downsampling to the TR interval. The cardiac frequency is the component with the highest power amplitude (red dashed line).

can be looked up in the DICOM header's slice timing information under "RefAcqTimes". Slice timing correction can already be performed automatically in FSL FEAT, however we chose to implement the correction ourselves in the frequency domain as the FSL implementation interpolates the time series. We found this interpolation to produce high frequency ringing artefacts that make the phase calculation at f_c unreliable.

All steps were performed in MATLAB. We used simulated data first to test the phase mapping code, in particular to guarantee a correct re-shift of the multiband-induced phase offsets $\phi_{i,r}$. Simulated data were used first to test the phase mapping code as described in the following subsection.

4.3.1.1 Simulation of cardiac phase data

The phase calculation outlined above was tested with random and real time series data. All simulations were implemented in MATLAB.

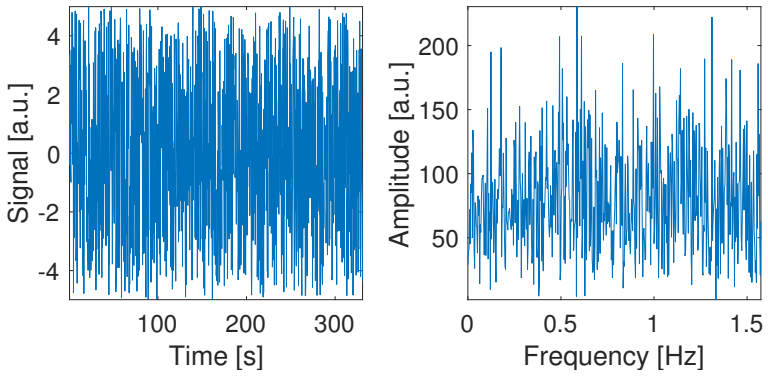


Figure 4.6: An example random time series (left) and the corresponding random frequency power spectrum (right).

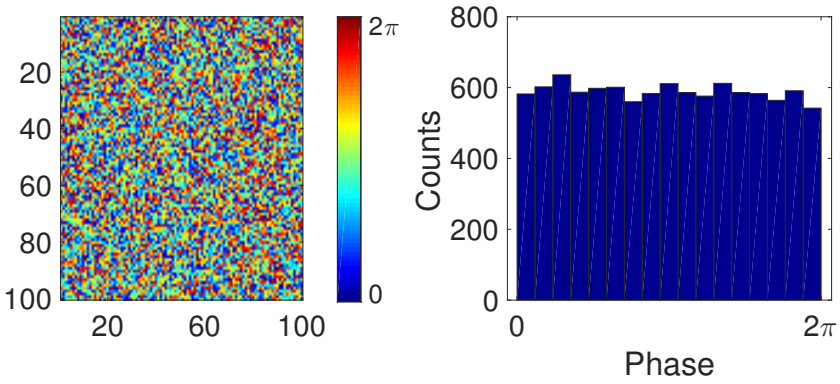


Figure 4.7: A phase map of randomly fluctuating voxels (left) exhibits a uniform phase histogram distribution (right).

Random data test

Random time series with zero mean were simulated, an example is given in Figure 4.6 together with its frequency-independent power spectrum. We set up a 2D slice of $90 \times 90 \times 24$ voxels with these random time series to simulate a noise scan. As desired this results in a random phase map and a uniform phase distribution when run through the phase mapping algorithm, see Figure 4.7.

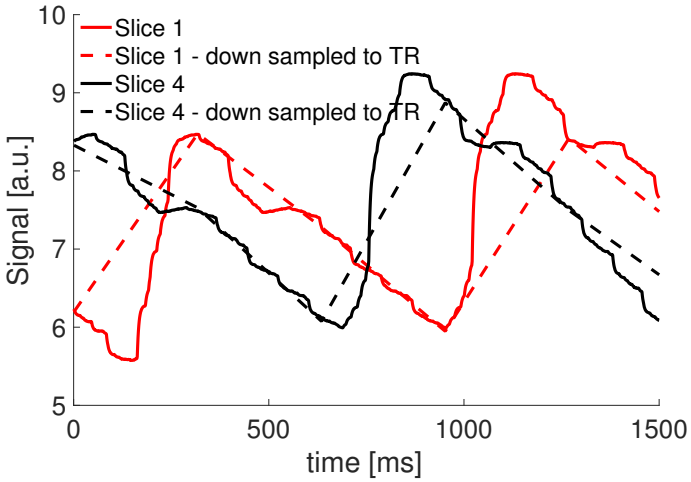


Figure 4.8: The cardiac time series from a pulse-oximetry measurement that was used for code testing. The black solid line is the original data (sampled at 1kHz) and the red line is shifted by 265 ms, to represent the signal at a different slice in the multiband acquisition order. The dotted lines are the same signals down-sampled to a typical TR of 320 ms.

Multiband phase correction test

To test the multiband phase correction approach in Eq. 4.11 we used a pulse-oximetry cardiac signal as an example non-random time series. To simulate the case of instantaneous transmission (no phase differences) we set up an imaging volume of $90\times90\times24$ voxels with this time series. We further added a random noise fluctuation on top of each voxel's signal for a typical SNR of 50. A TR of 320 ms was chosen to down-sample the time series to a realistic temporal resolution. To introduce a multiband acquisition slice timing we shifted the time series along the slice direction by $[0; 160; 52.5; 265; 107.5; 212.5]$ ms, which would be a realistic timing for a multiband factor of 4 and 24 slices. Figure 4.8 shows the time series at slices 1 and 4. We then ran the phase mapping code with and without phase correction on this artificial 4D dataset. Figure 4.9 shows the phase map along the in-plane and slice dimension (equivalent to a sagittal or coronal view). The stripes in the phase map correspond

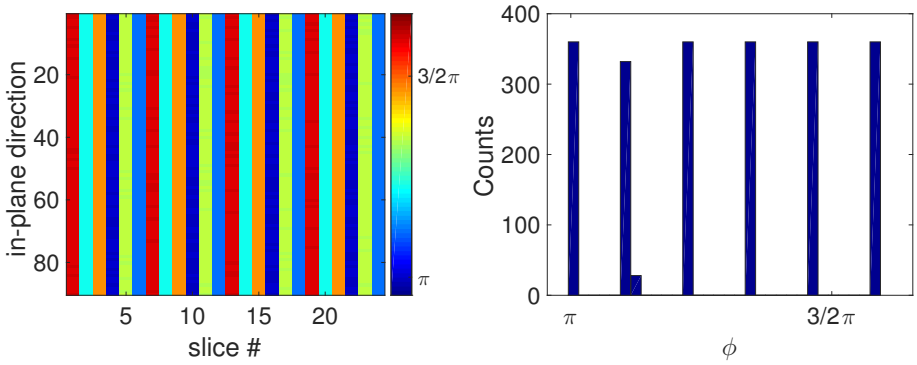


Figure 4.9: Simulated time series that is instantaneously transmitted over 24 slices and sampled with a multiband factor of 4. The phase map (left) and phase distribution (right) show the 6 phase stripes introduced by the acquisition timing.

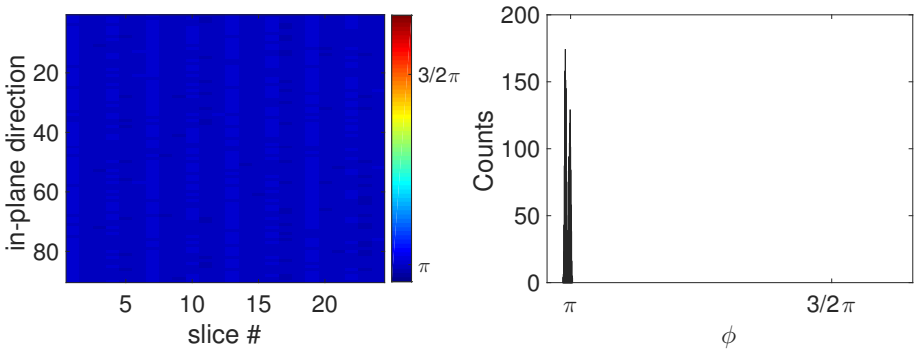


Figure 4.10: The same simulated data as in Figure 4.9, but with phase correction along the slice dimension. The phase distribution is only affected by signal differences that are introduced by noise and the TR down-sampling.

to the uncorrected shifts in the time domain. The phase distribution has 6 discrete phase bands as expected for 24 slices and a multiband factor of 4. Figure 4.10 shows the same dataset being phase mapped with phase correction. The phase differences are negligible and revert to the added noise (SNR) and down-sampling noise.

As a final verification of the phase mapping code we tested if a temporal delay in the signals at different voxel locations was correctly reflected in the calculated phase difference. We added a time delay of 100 ms to every even slice and ran the phase mapping code, including the multiband phase

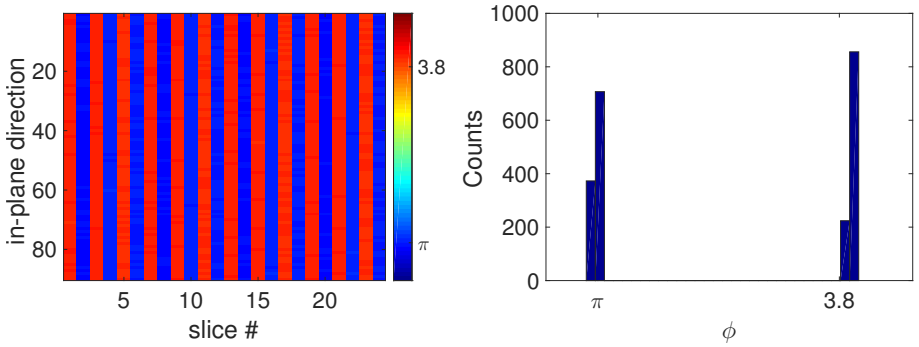


Figure 4.11: A time delay of 100 ms between even and odd slices was added. The pattern can be seen in the phase map and the phase distribution. The expected phase difference between signals is 0.7 radians.

correction. The dominant cardiac frequency at which the phase maps were calculated was $f_c \approx 1.1$ Hz for this particular time series. The expected phase shift between slices is then $\Delta\phi = 2\pi f_c \Delta t \approx 0.7$ radians as is indeed shown in the phase distribution in Figure 4.11.

4.3.2 S_0 and T_2^* mapping

To investigate the mechanisms of cardiac signal fluctuations, we calculated $T_2^*(\tau)$ and $S_0(\tau)$ fluctuation maps. The approach is based on the assumption that the cardiac-induced fluctuations are independent of the absolute cycle duration, but nevertheless have a fixed phase relationship to the unit cycle. This idea was already applied by Hu et al. in the 90s [188] who mapped the k-space signal magnitude and phase over the cardiac cycle to correct for physiological noise. A simultaneous external recording of the cardiac waveform during the fMRI acquisition facilitates the unit cycle mapping. We discretized the EPI signal from Eq. 4.2 by splitting τ into a fixed number, n,

of equidistant bins:

$$S(\tau_j) = S_0(\tau_j) \cdot \exp\left\{\frac{-\mathrm{TE}}{T_2^*(\tau_j)}\right\} \qquad \text{with} \qquad j = 1, 2, ..., n. \tag{4.12}$$

A trigger signal sent from the scanner at each RF-excitation allows a post-ordering of measurement points to their appropriate acquisition bin. A widely used approach for S_0/T_2^* mapping is fitting of dual-echo or multi-echo data to Eq. 4.12 [164,189]. A first-order polynomial is fitted to its linearised form:

$$\ln\Big[S(\tau_j)\Big] = \ln\Big[S_0(\tau_j)\Big] - \frac{\mathrm{TE}}{T_2^*(\tau_j)}\,. \tag{4.13}$$

The data were fitted first and then ordered. S_0 values were assigned into the bin closest to the time of the RF-trigger ("zero-echo time"). T_2^* values were assigned to the bin closest to the mean echo time $(\mathrm{TE}_1 + \mathrm{TE}_2)/2$. This procedure adds a systematic phase variation, but should be affordable here as the time between the trigger and the inter-echo time of approximately 30 ms is smaller than the actual bin size of approximately 100 ms (for an average cardiac frequency of 1Hz). Again, the multiband-specific timing needs to be taken into account for data ordering. An example timing scenario for a dual-echo multiband dataset is provided in Figure 4.12. With $T_2^*(\tau)$ and $S_0(\tau)$ fluctuation maps calculated, we quantified pulsatility in a voxel as the maximum fluctuation amplitude around the mean in percent

$$S_{0,p} := \frac{\max[S_0(\tau_j)] - \min[S_0(\tau_j)]}{\overline{S_0(\tau_j)}} \times 100\%\,. \tag{4.14}$$

$T_{2,p}^*$ was defined similarly.

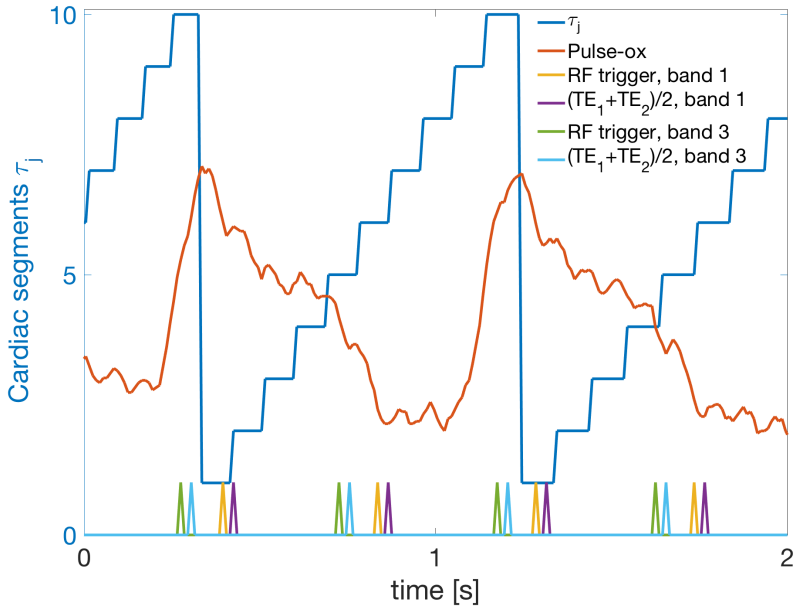


Figure 4.12: Cardiac cycle segmentation and timing of a dual-echo multiband sequence. Timings are shown for band 1 and 3. The pulse-ox signal (orange) marks the systole-to-systole period τ_c of the cardiac unit cycle that is segmented into equidistant bins τ_j (dark blue). The yellow and purple spikes label the timing of the RF-trigger and the mean echo time for the slices in the first multiband; the green and light blue spikes refer to the timing of the third multiband. The S_0 fit results are assigned to the bins of the RF-trigger and the T_2^* values count towards the bins of the mean echo time.

4.3.3 $\mathbf{T_2^*(\tau)}$ simulations

With the $S_0(\tau_j)/T_2^*(\tau_j)$ calculated from the data we aimed to simulate the plausible effects that could lead to the measured $T_2^*(\tau_j)$ taking into account partial volume fluctuations $v_i(\tau_j)$.

Our model implies the following assumptions:

1. The arteriolar dilation/constriction is synchronous with the inflow effect $S_0(\tau)$ and is multiplied by a scaling factor d:

$$v_{art}(\tau) = d \cdot S_0(\tau) \tag{4.15}$$

2. For simplicity capillaries and venules are combined to a single compartment v_{cap}. The cardiac wave is reflected backwards at the end-arteriole level (with arterioles accounting for $\approx$ 20%, capillaries for $\approx$ 70% and venules for $\approx$ 10% of microvascular resistance [190]). The effective delay τ_d in the dilation in the capillaries/venules is unknown and we simulated for all possible shifts:

$$v_{cap}(\tau) = v_{art}(\tau + \tau_d) \qquad \text{with} \qquad \tau_d = (0, ..., \tau_c]. \tag{4.16}$$

3. According to the Monro-Kellie doctrine the total voxel volume must be conserved, but the cranial compartments should be incompressible [191]. Hence, we hypothesize CSF to move in and out of the voxel to fulfil

$$\sum_i v_i(\tau) = 1\,. \tag{4.17}$$

We simulated $S_{multi}(\tau_j)$ (Eq. 4.4) for a GM voxel at the dominant arterial phase (this term will be explained in the Results), taking the measured $S_0(\tau_j)$ as input for Eq. 4.15. Similar to the partial volume estimate (PVE) threshold we used for tissue masking (see next paragraph), we set the average GM

volume fraction to $\bar{v}_{\mathrm{GM}} = 0.93$. Assuming a ratio of arterioles to capillaries and venules of 1:2 [190] and a total blood volume fraction of 0.055, we set $\bar{v}_{art} = 1/3 \times 0.055$ and $\bar{v}_{cap} = 2/3 \times 0.055$. We used $T^*_{2,GM} = 29$ ms (from our data), $T^*_{2,art} = 49$ ms (interpolation from [183]) $T^*_{2,cap} = 15$ ms (assuming $Y = 0.8$ in [192]), and $T^*_{2,CSF} = 300$ ms. Spin densities were set to $\rho_{\mathrm{GM}} = 0.89$, $\rho_{blood} = 0.87$ [187] and $\rho_{\mathrm{CSF}} = 1$. $M_{z,i}$ were calculated as described in the Theory section for 7T values of $T_1 = 2132/2587/4425$ ms for GM, blood compartments and CSF, respectively [31].

As argued above, parenchyma is thought to be incompressible (Monro-Kellie hypothesis), however, tissue could still be moving in and out of the voxel so we ran simulations for the two scenarios:

i Dynamic CSF volume conserves the voxel volume.

ii Parenchymal volume fluctuations conserve the voxel volume.

To quantify the goodness of fit between the modelled $T^*_{2,\mathrm{sim}}(\tau_j)$ and the measured data $T^*_2(\tau_j)$, we calculated the χ^2 value

$$\chi^2 = \sum_{j=1}^{n} \frac{[T^*_{2,\mathrm{sim}}(\tau_j) - T^*_2(\tau_j)]^2}{\sigma^2_{T^*_2(\tau_j)}}\,. \tag{4.18}$$

In our case we have 10 sample points (see Post-processing) and vary two parameters in the fitted model (the delay τ_d and the scaling factor d). As a result we have $10 - 2 = 8$ degrees of freedom to calculate the appropriate χ^2 probability density distribution for. More information on the the χ^2 statistics and a distribution plot is given in Appendix B. From the χ^2 value we determine which τ_d and d yield the highest goodness of fit for scenario i and ii.

4.3.4 MR data and post-processing

We scanned 8 healthy subjects (age range: 23-34 ys) under institutional ethical approval. The scans were acquired on a 7T whole-body scanner (MAGNETOM 7T, Siemens, Erlangen, Germany) using a 1 channel Tx/32 channel Rx head coil (Nova Medical, Wilmington, MA, USA). Physiological signals were measured throughout the scans using a respiratory belt and a pulse-oximetry finger clip, recorded at 1 kHz (BioPac Systems, Goleta, CA, USA). The following scans were acquired during the session:

Tissue segmentation: T_1-MPRAGE and susceptibility-weighted imaging (SWI)

T_1-MPRAGE: TR = 2200 ms; inversion time, TI = 1050 ms; TE = 2.96 ms; flip angle, $\alpha = 7°$; nominal resolution: $0.7 \times 0.7 \times 0.7\,\text{mm}^3$; bandwidth, BW = 240 Hz/px; GRAPPA factor = 2; field of view, FOV_{read} = 224 mm (read direction), FOV_{phase} = 100% (phase direction), slices = 256, scan time ≈ 6 mins. SWI: TR = 22 ms; TE = 15 ms; $\alpha = 15°$; flow compensation on; no GRAPPA; BW = 120 Hz/px; nominal resolution: $0.5 \times 0.5 \times 2.0\,\text{mm}^3$; FOV_{read} = 220 mm; FOV_{phase} = 81.3%; phase partial Fourier factor = 6/8; slices = 56; scan time ≈ 6.5 mins.

Cardiac phase mapping: single-echo EPI

Multiband EPI [95, 96, 193]: TR = 334 ms; TE = 26 ms; inter-echo spacing = 0.68 ms; $\alpha = 33°$; multiband factor = 6; GRAPPA factor = 2; BW = 1852 Hz/px; nominal resolution: $2.2 \times 2.2 \times 2.2\,\text{mm}^3$; FOV_{read} = 200 mm; FOV_{phase} = 100%; no partial Fourier acquisition; slices = 40; volumes = 2200; scan time ≈ 12 mins.

S_0 and T_2^* mapping: dual-echo EPI

Multiband EPI [95, 96, 193]: TR = 405 ms; TE_1/TE_2 = 21.4/52.1 ms; inter-echo spacing = 0.65 ms; $\alpha = 90°$; multiband factor = 3; GRAPPA factor = 2; BW = 2085 Hz/px; nominal resolution: $2.2 \times 2.2 \times 2.2\,mm^3$; FOV_{read} = 200 mm; FOV_{phase} = 100%; no partial Fourier acquisition; slices = 15; volumes = 500; scan time $\approx$ 3.3 mins. Note, that the double-echo EPI scans were acquired with a flip angle of 90° in order to maximise the sensitivity to inflow effects and maximise our ability to measure S_0 pulsatility.

4.3.4.1 Cardiac phase mapping: single-echo EPI

The data set was processed through FSL FEAT, including skull stripping, motion correction, field map correction, de-meaning and registration to the T_1w structural and to MNI standard space. Appropriate transformations were applied to the PVE maps and the arterial and venous masks for analysis in EPI space. The processed data set was read into MATLAB to perform cardiac phase mapping as described in the Methods. In order to solely include voxels with sufficient cardiac modulation in our analysis we created a cardiac binary mask. This cardiac mask was derived with the GLM approach from the previous chapter, rejecting voxels with p-values above 0.05. PVE maps were binarised at a value of 0.9 to create tissue masks. Finally the cardiac phase map was multiplied by the binary cardiac and tissue masks to produce tissue-specific cardiac phase distributions. We further created two "arterial envelope" masks to study the phase values in the vicinity of large arterial structures. The first envelope mask consists of neighbouring voxels of the arterial mask, and the second envelope mask is the outer voxel layer of the first envelope. Figure 4.13 shows an example colour-coded mask for a representative subject.

The absolute phase value between subjects is arbitrary. We therefore shifted each subject's phases such that the predominant phase value in the arterial mask distribution matched $-\pi/2$ (see Fig. 4.14 in the Results). For the remainder we will refer to this peak as the "dominant arterial phase peak". This phase synchronisation allowed us to combine the phase data across subjects.

In addition to the tissue-specific analysis we evaluated phase values in different brain structures. To achieve this, we warped the phase maps and the cardiac binary masks into MNI space. Brain area masks from the Harvard-Oxford atlases (included in FSL) were thresholded at a probability of 0.5 and mean phases were calculated in those masks. The mean phase in an MNI voxel was calculated by converting the phase value to Cartesian coordinates, summing over each Cartesian component and reconverting to polar coordinates: $\overline{\phi} = atan2\left[\sum_s sin\,\phi_s, \sum_s cos\,\phi_s\right]$, where s is the number of values per voxel to average over.

4.3.4.2 S_0 and T_2^* mapping: dual-echo EPI

Only the first echo was run through motion correction (McFLIRT, FSL) as the contrast in the second echo was not optimal. The correction was then applied to the second echo as motion during the inter-echo time ($\approx$ 30 ms) should be negligible. The data were read into MATLAB and $S_0(\tau_j)$ and $T_2^*(\tau_j)$ maps were calculated as described in the Methods. The first 10 TRs were omitted to account for non-steady state effects. We segmented the cardiac unit cycle into 10 bins (average of 49 data points per bin). Registration to the single-echo EPI was performed and the transformation was applied to the $S_0(\tau_j)/T_2^*(\tau_j)$ maps. To synchronize cycles τ_j across subjects for data combination, we shifted each subject's τ_j such that the minimum S_0 in the

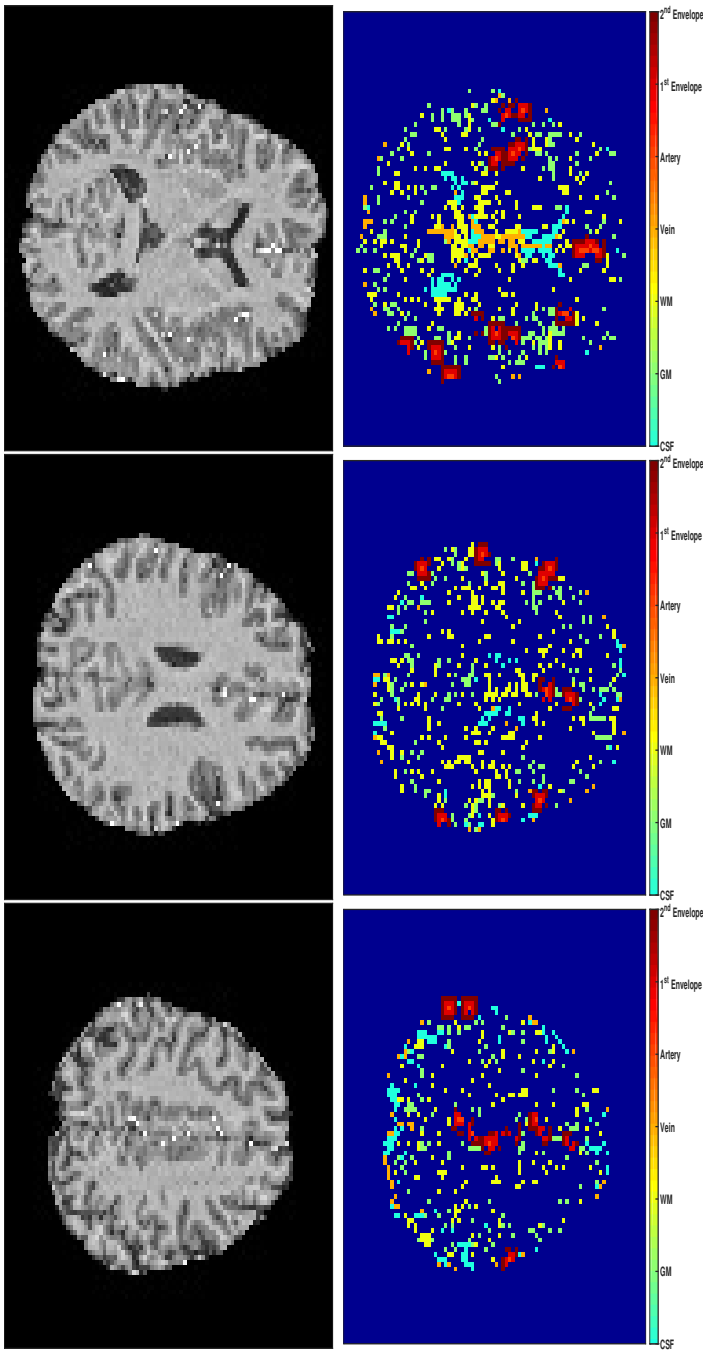


Figure 4.13: Cardiac-thresholded tissue masks (right) and the anatomical reference (left) in an example subject. All coloured voxels refer to a specific tissue with a PVE> 0.9 and a cardiac modulation with a p-value > 0.05, except for the arterial and venous masks that were derived from signal level thresholds in the T1w and SWI scans. The arterial envelopes are the neighbouring contours of the arterial mask. Note that the arterial envelopes not always form continuous circles as not all voxels (in particular in the 2^{nd} envelope) necessarily show a significant cardiac modulation.

arterial mask ($\min[S_0(\tau_j)]$) occurred in the first bin ($j = 1$).

4.4 Results

4.4.1 Cardiac phase mapping

4.4.1.1 Tissue-specific results in EPI space

A representative subject's phase distribution in the different tissue compartments is displayed in Figure 4.14a, and the average distribution over all subjects is given in Figure 4.14b. Comparing the single subject and group average figures we note that the cardiac phases are similarly distributed across all subjects. The dominant peak, originating in the arteries at $\phi_c = -\pi/2$, is present in the surrounding voxels (1^{st} and 2^{nd} envelope masks), in CSF and in GM. A second major phase at $\phi_c \approx \pi/2$ can be found in all tissue compartments. A control distribution, derived from a low-power frequency component, shows a flat random distribution (bottom row to the right in Fig. 4.14), as expected.

4.4.1.2 Area-specific phase distributions in standard space

The tissue-specific distributions do not yield any information about spatial variations in the shifts. We therefore calculated the phase distributions in MNI space for the cortex and subcortical areas. Figure 4.15 shows the tissue-specific grey matter phase distribution split into the area-specific distributions in the cortex, putamen, caudate, thalamus and pallidum (all histograms are displayed normalised). The distribution in the cortex (red) shows a single peak slightly shifted to the left of the dominant arterial phase value of $-\pi/2$ but the second bi-phasal peak from the overall grey matter distribution (light

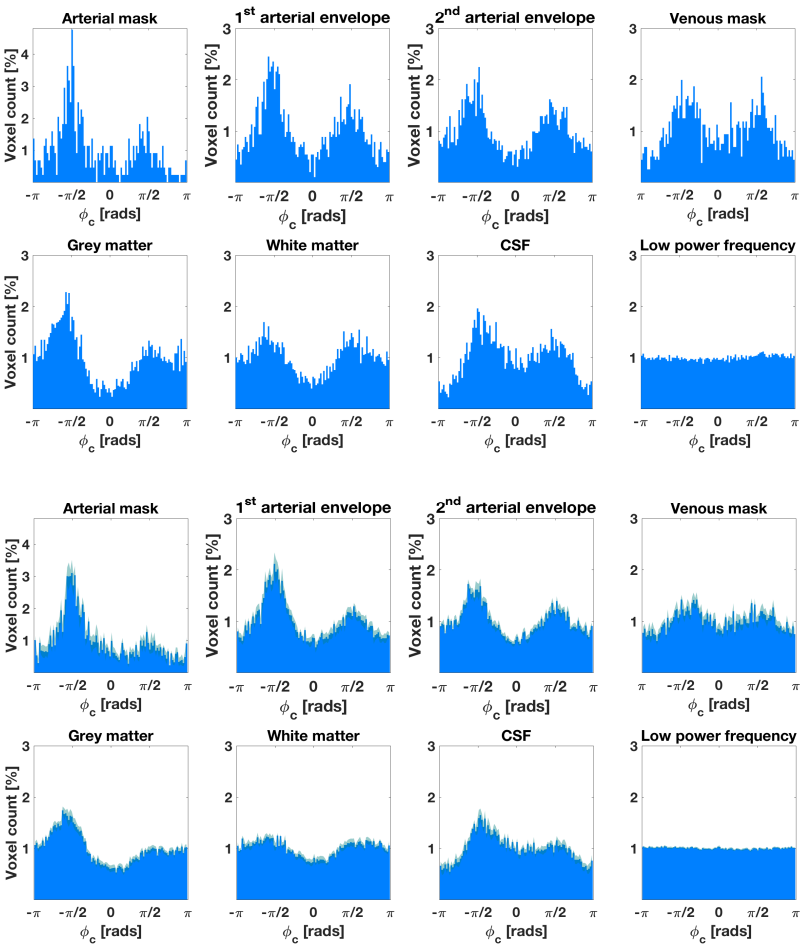


Figure 4.14: Phase distributions (dark Oxford blue) in different tissue compartments. The bottom row distribution to the right is a control distribution derived from all voxels' phases at a low power frequency. **a)** is a single representative subject and **b)** is the group average with the standard error of the mean (light Cambridge blue) plotted on top of the distribution.

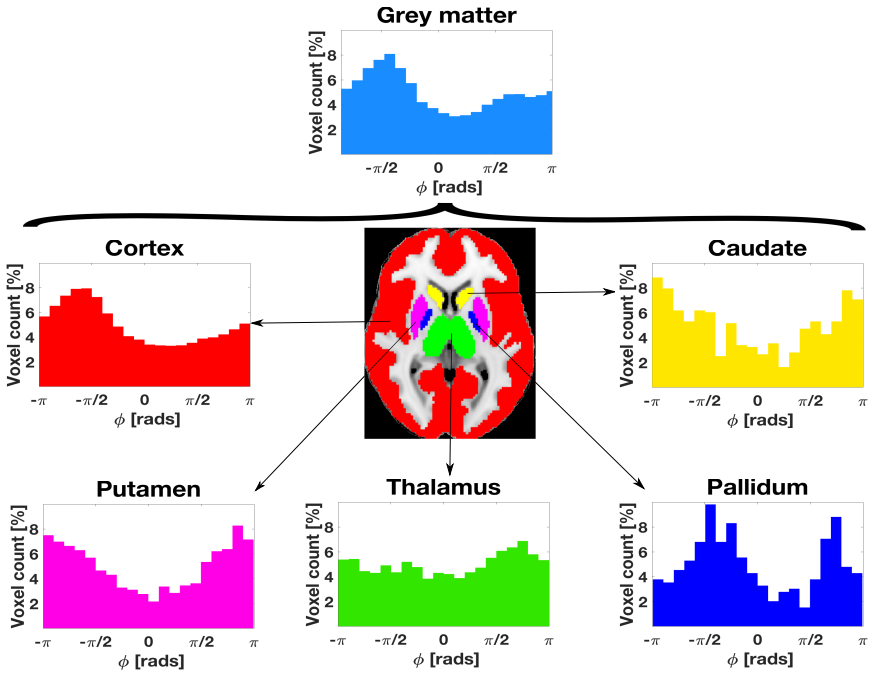


Figure 4.15: Area-specific distribution of cardiac phase values in MNI space. The light blue distribution on the top is the overall grey matter phase distribution that can be split into the cortical (red), putamen (pink), caudate (yellow), thalamus (green) and pallidum (dark blue) distributions. The peak in the cortical distribution is slightly shifted to the left of the dominant arterial phase peak at $-\pi/2$. Subcortical areas' peaks are shifted further apart. Each distribution histogram is displayed normalised to itself.

blue) is absent. However, the subcortical areas show distinct shifts away from the dominant arterial phase, indicating that the cardiac cycle- induced signals in these areas have offset timings to the signals in the arterial regions and the cortex. In summary Figure 4.15 shows how the overall bi-modal grey matter phase distribution is the sum of area-specific shifted single-peak distributions.

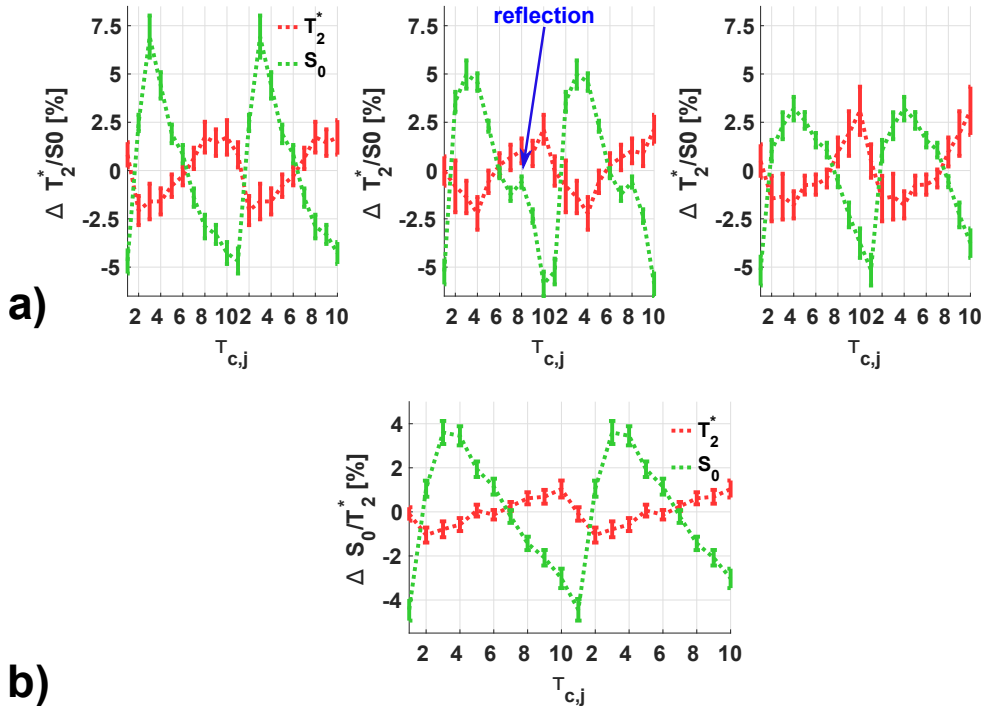


Figure 4.16: Cardiac unit cycle fluctuations of S_0 (green) and T_2^* (red) at the dominant phase $\phi_c = -\pi/2 \pm 0.3$ rad in the arterial mask. The unit cycle is plotted twice for a better visibility of the waveforms. **a)** Three single subjects, **b)** average over all subjects. The dips in the single-subject S_0 waveforms are potentially reflected waves.

4.4.2 S_0 and T_2^* mapping

Figure 4.16a shows single-subject examples of $S_0(\tau_j)$ and $T_2^*(\tau_j)$ fluctuations at the dominant phase of $\phi_c = -\pi/2 \pm 0.3$ rad in the arterial mask, and Figure 4.16b provides the group-averaged waveforms. The $S_0(\tau_j)$ waveform shows a strong similarity to the arterial pressure waveform - compare with the waveforms measured with ICP, TCD and cine-MRI in Figure 4.2. A steep rise of S_0 to systole is followed by a slower decrease and, most remarkably, "dicrotic notch-like" features are discernible in the single subject plots. These dips are even more distinguishable in the GM waveforms in Figure

4.17. If these dips were instances of the dicrotic notch we would expect them to be more pronounced in the arterial mask, so we assume that these are instances of backwards travelling waves from end-arteriolar reflections and not from the heart. However, this is a speculative interpretation and the "dip" in the waveforms is on the size of the error bars. The T_2^* waveform in the arteries follows an inverted form of the S_0 waveform, with a slow rise in T_2^* that is followed by a steep decline. This is expected, assuming that arteries are surrounded by CSF spaces, and CBV increase in the voxel is likely to push out CSF spins ($T^*_{2,\mathrm{blood}} \ll T^*_{2,\mathrm{CSF}}$). However, the waveforms are particularly anti-cyclic in the arterial mask and there is likely an enhancement of the effect that is caused by an inverse coupling of T_2^* changes into the S_0 component as a result of the fitting procedure. The GM $T_2^*(\tau_j)$ waveform behaves less intuitively. We would have expected to observe an increase in T_2^* in synchrony with S_0 when CBV increases as $T^*_{2,\mathrm{GM}} \ll T^*_{2,\mathrm{blood}}$. If brain motion caused a signal decline during systole we would expect T_2^* to be π radians asynchronous to S_0. However, $T_2^*(\tau_j)$ waveforms are shifted further and show a mirroring slope to $S_0(\tau_j)$.

$S_{0,p}$ and $T^*_{2,p}$ pulsatility values were calculated after Eq. 4.14 for the dominant arterial phase and the second phase peak. The results for all tissues are summarised in Table 4.3.

$S_0(\tau_j)$ and $T_2^*(\tau_j)$ vary strongly within a given tissue and cause the distribution in the phases as discussed in detail in the Theory. However, it renders a comparison between tissues using tables and figures cumbersome. For a more approachable overview we provide animations in Figures 4.18–4.22 for the arterial, GM, WM, CSF and venous masks. The top panel of each tissue animation shows the peak-to-peak pulsatility values $S_{0,p}$ and $T^*_{2,p}$

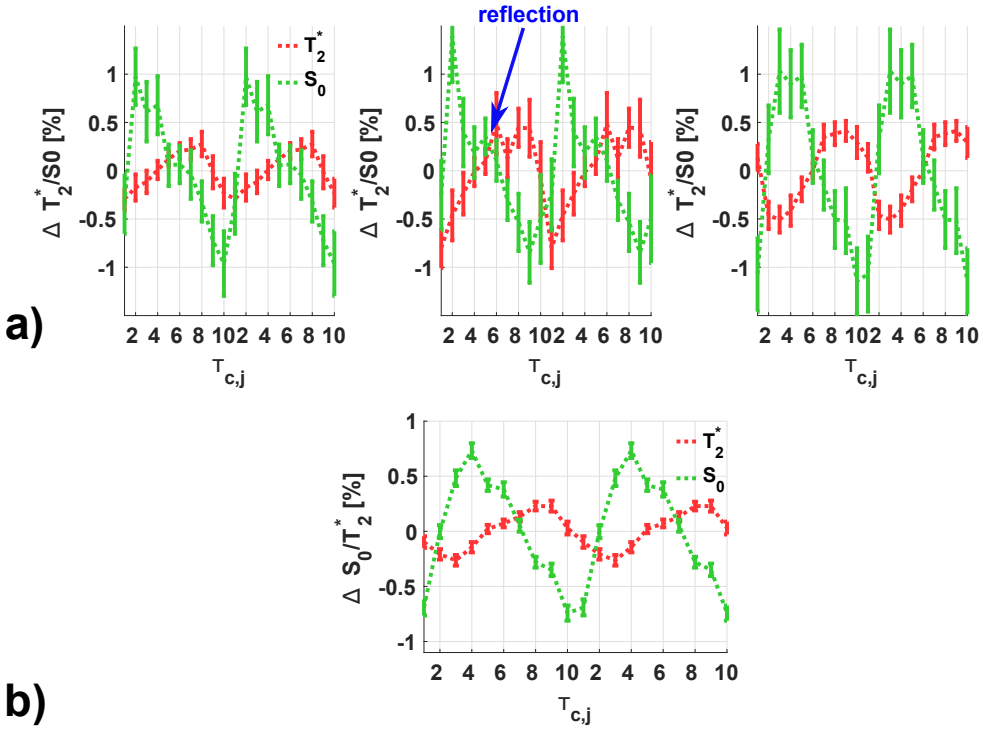


Figure 4.17: Cardiac unit cycle fluctuations of S_0 (green) and T_2^* (red) at the dominant phase $\phi_c = -\pi/2 \pm 0.3\,\text{rad}$ in GM. The unit cycle is plotted twice for a better visibility of the waveforms. **a)** Three single subjects, **b)** average over all subjects. The dips in the S_0 waveforms are potentially reflected waves.

Tissue type	**Dominant arterial peak** ($\phi_c = -\pi/2 \pm 0.3\,\text{rad}$)		**Second peak** ($\phi_c = \pi/2 \pm 0.3\,\text{rad}$)	
	$\mathbf{S_{0,p} \pm SEM}[\%]$	$\mathbf{T^*_{2,p} \pm SEM}[\%]$	$\mathbf{S_{0,p} \pm SEM}[\%]$	$\mathbf{T^*_{2,p} \pm SEM}[\%]$
Arterial mask	7.98 ± 0.39	2.09 ± 0.29	4.69 ± 0.77	1.81 ± 0.93
Venous mask	2.03 ± 0.36	1.14 ± 0.40	1.77 ± 0.48	1.39 ± 0.46
GM	1.44 ± 0.06	0.49 ± 0.04	0.26 ± 0.08	0.32 ± 0.06
WM	0.49 ± 0.06	0.15 ± 0.03	0.34 ± 0.06	0.21 ± 0.04
CSF	3.81 ± 0.16	1.28 ± 0.16	1.23 ± 0.22	1.30 ± 0.30

Table 4.3: Peak-to-peak percentage fluctuation $S_{0,p}$, $T^*_{2,p}$ and the standard error of the mean (SEM) at the dominant arterial phase peak and at the second major peak around $\pi/2$ (see Figure 4.14).

overlaid onto the phase distribution. The bottom panel sweeps through the $S_0(\tau_j)/T^*_2(\tau_j)$ waveforms of the entire phase range. Flicking through the animations, we summarise our key observations for each tissue type.

- *Arterial mask (Figure 4.18)*

  $S_{0,p}$ is maximised at the dominant peak and is highest in the arterial mask compared to any other tissue. The arterial mask was derived from major arteries (MCA and its early perforators), and the inverse relation between S_0 and T^*_2 is likely due to a partial voluming with surrounding CSF. The systolic increase in CBV is likely to push CSF ($T^*_{2,\text{blood}} \ll T^*_{2,\text{CSF}}$) out of the voxel (on the whole brain level compensating CSF volume is known to leave the cranium during systole via pathways along the dural venous sinuses [194]).

- *Grey matter mask (Figure 4.19)*

  $S_0(\tau_j)$ varies in amplitude over different phases. $T^*_2(\tau_j)$ changes shape slightly for different phase ranges, but appears to have a stable timing and amplitude for all phases with peak-to-peak fluctuations that range from$T^*_{2,p} = 0.33 \pm 0.04\%$ to $0.5 \pm 0.06\%$. The slope of the $T^*_2(\tau)$ waveform

tends to mirror the slope of $S_0(\tau)$.

- *White matter mask (Figure 4.20)*

  White matter has the smallest $S_{0,p}$ and $T^*_{2,p}$ pulsatility compared to the arterial and GM masks. This is likely due to WM being sparsely vascularised. $S_0(\tau_j)$ has an altered shape and timing, which could be due to a delay in the actual CBF/CBV pulsatility or variations in reflections of the pressure wave. T^*_2 pulsatility is not as stable as in GM and peak-to-peak fluctuations that range from $T^*_{2,p} = 0.05 \pm 0.03\%$ to $0.23 \pm 0.04\%$. Error bars are high and WM results should be interpreted with caution.

- *CSF mask (Figure 4.21)*

  There is a strong $S_{0,p}$ pulsatility at the dominant arterial phase which likely arises from narrow CSF spaces with faster flow, for example around arterial vessels. This is also the phase range that we suspect to be dominantly located in the subarachnoid spaces around the cortex. $S_{0,p}$ drops towards positive phase values. From our area-specific analysis of the phase distribution we concluded that this range is predominantly situated in the ventricles where directional flow might be minimal and only a movement effect causes T^*_2 fluctuations. In most cases, we find T^*_2 fluctuations to be asynchronous with S_0. It might be an inflow of arterial spins or movement of boundary GM spins, both with lower T^*_2 than CSF, that underlie this effect.

- *Venous mask (Figure 4.22)*

  The inflow effect is not as pronounced as in the other masks. S_0 and T^*_2 fluctuate π radians out of phase for negative cardiac phases and slightly asynchronous for higher phase regimes. Error bars are high

compared to other tissue masks and likely revert to the smaller overall size of the venous mask compared to other tissue masks and high partial volume effects (recall that the venous mask is not based on a PVE threshold, but only on a signal level threshold from the SWI scan). The S_0 and T_2^* waveform π-asynchrony could be a partial volume effect with surrounding CSF.

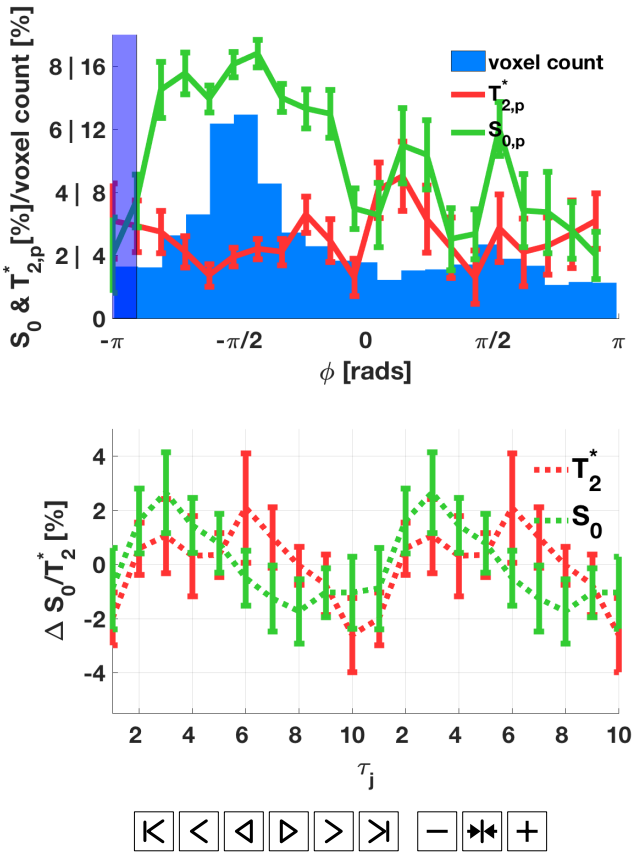


Figure 4.18: Arterial mask pulsatility in S_0 and T_2^* for all phase ranges. Top row: The phase distribution (blue) with the corresponding peak-to-peak pulsatility $S_{0,p}$, $T^*_{2,p}$ at different phases ranges (binned to increments of 0.6 rad). Bottom row: The cardiac unit cycle waveforms $S_0(\tau_j)/T_2^*(\tau_j)$ within the phase range indicated by the blue bar on the phase distribution plot. The unit cycle is plotted twice for a better visibility of the waveforms. **A separate movie file "ArterialAnimated.mp4" is provided in the supplementary material uploaded in the digital submission.**

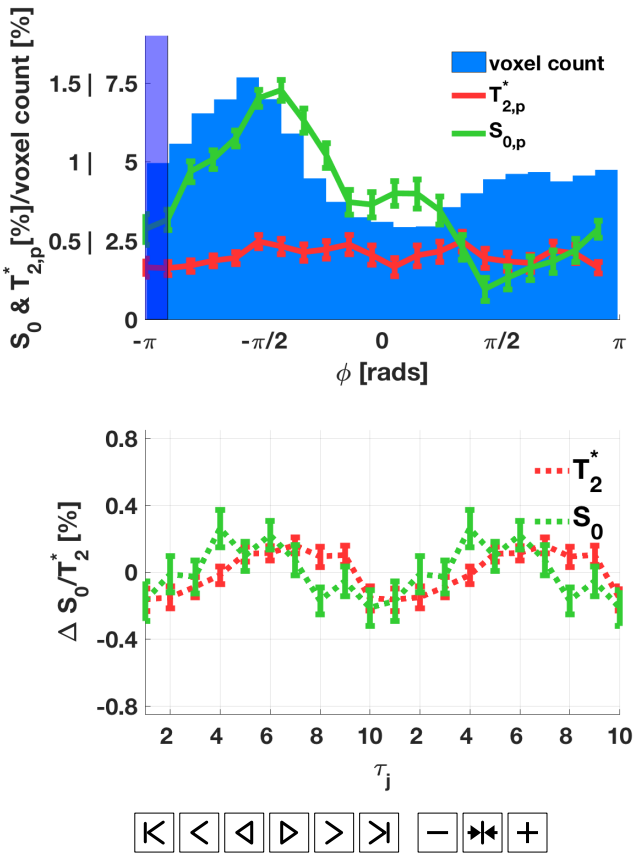


Figure 4.19: Grey matter pulsatility in S_0 and T_2^* for all phase ranges. The unit cycle is plotted twice for a better visibility of the waveforms. **A separate movie file is provided in the supplementary material uploaded in the digital submission.**

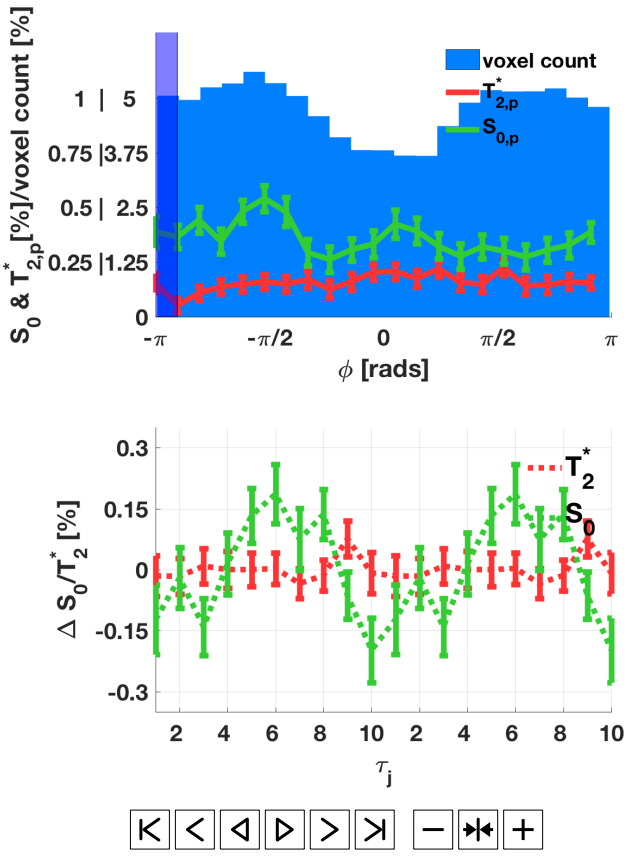


Figure 4.20: White matter pulsatility in S_0 and T_2^* for all phase ranges. The unit cycle is plotted twice for a better visibility of the waveforms. **A separate movie file is provided in the supplementary material uploaded in the digital submission.**

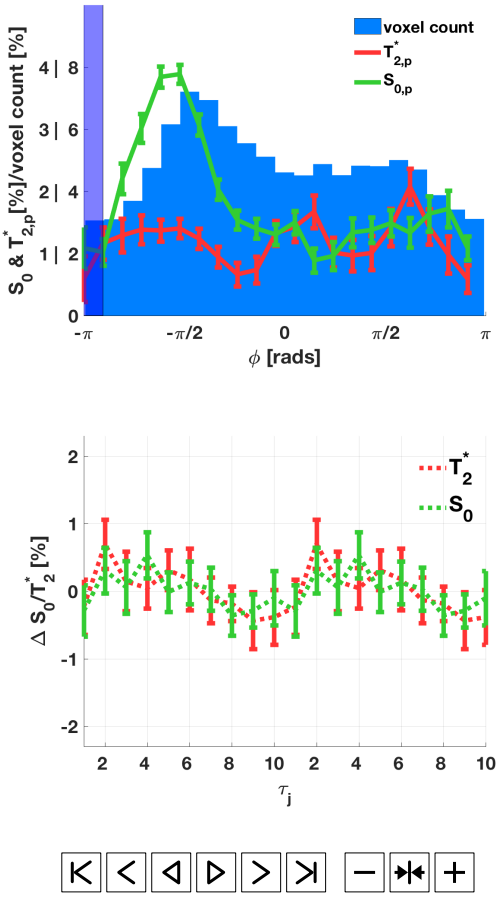


Figure 4.21: CSF pulsatility in S_0 and T_2^* for all phase ranges. The unit cycle is plotted twice for a better visibility of the waveforms. **A separate movie file is provided in the supplementary material uploaded in the digital submission.**

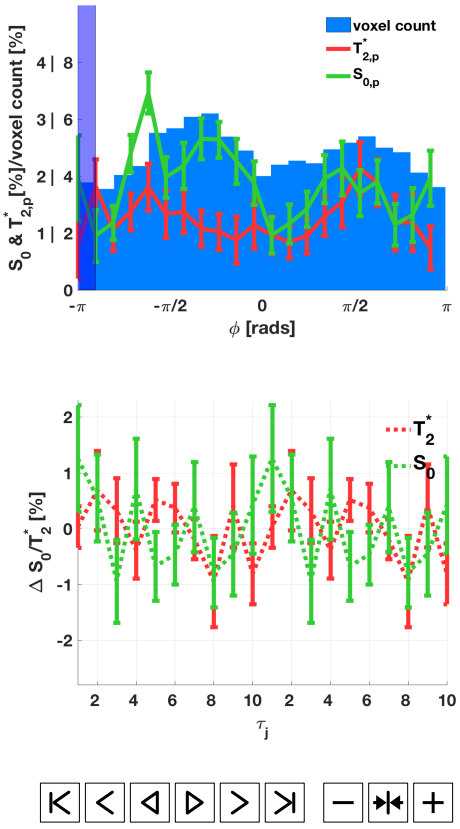


Figure 4.22: Venous pulsatility in S_0 and T_2^* for all phase ranges. The unit cycle is plotted twice for a better visibility of the waveforms. **A separate movie file is provided in the supplementary material uploaded in the digital submission.**

4.4.2.1 Absolute T_2^* values

To determine the T_2^* values that we used in section 4.2 for the estimate of ΔT_2^* due to oxygenation and partial volume fluctuations, we listed the average T_2^* values in the different tissue from our data in table 4.4. The values are derived from the masks that we used in the tissue-specific phase and pulsatility analysis and refer to a PVE threshold of 0.9. Our GM values of 29.22 ± 1.3 ms are in good accordance with reported values in the literature, for example with Uludag et al.'s 27.8 ms [181]. The value for the venous compartment is overestimated, most likely due to partial volume effects, and further we used echo times that are too long to capture the short venous T_2^* reliably. The CSF values are also not trustworthy. In the CSF case the experimental echo times are too short to measure the long T_2^* value. This is the reason why we only used our GM and WM T_2^* values in the estimates and simulations and took venous and CSF values from the literature.

Tissue type	$\langle \mathbf{T_2^*} \rangle \pm \boldsymbol{\sigma}$**[ms]**
Arterial mask	33.7 ± 6.7
Venous mask	29.6 ± 5.0
Grey matter	29.2 ± 1.3
White matter	24.9 ± 1.4
CSF	59.5 ± 14.3

Table 4.4: Average T_2^* values in different tissue.

4.4.3 $T_2^*(\tau)$ simulations

4.4.3.1 Dynamic CSF volume model

As described in the Methods section, we expect the voxel volume during a cardiac-induced CBV change to be conserved by dynamic CSF partial volume changes. The best agreement between simulations and measured $T_2^*(\tau_j)$ waveforms was obtained for a scaling factor of $d = 11.95$ and a delay between arteriolar and capillary blood volume fluctuations of $\tau_d = 0.8 \times \tau_c$. For this fit the χ^2 was minimsied to a value of 0.405 which is associated with a high confidence level of 0.999 (see the red dotted line in Appendix B, Figure B.2) that the model is a good fit to the data. However, this high value is likely due to the fact that the measurement error (the σ_j^2 variance terms in Eq. 4.18) is large compared to the measured change in T_2^*, i.e. the data is very noisy. The simulation for this scaling factor and all possible delays is plotted in the animated Figure 4.23. A delay of $\tau_d = 0.8 \times \tau_c$ is approximately 800 ms for an average heart rate of 1 Hz. The scaling factor of $d = 11.95$ between $v_{art}(\tau_j)$ and $S_0(\tau_j)$ (see Eq. 4.15) translates into an arteriolar blood volume fluctuation of +8.64% to −8.13% (relative to the blood volume fraction and not the overall voxel volume) from systole to diastole. To put this into context: the arteriolar CBV increase during visual stimulation in the human visual cortex has been reported in one study as 16.6% [195].

4.4.3.2 Parenchymal volume fluctuation model

Figure 4.24 shows the simulation results for parenchymal volume fluctuations. Here, it was impossible to match simulations to an acceptable error and the

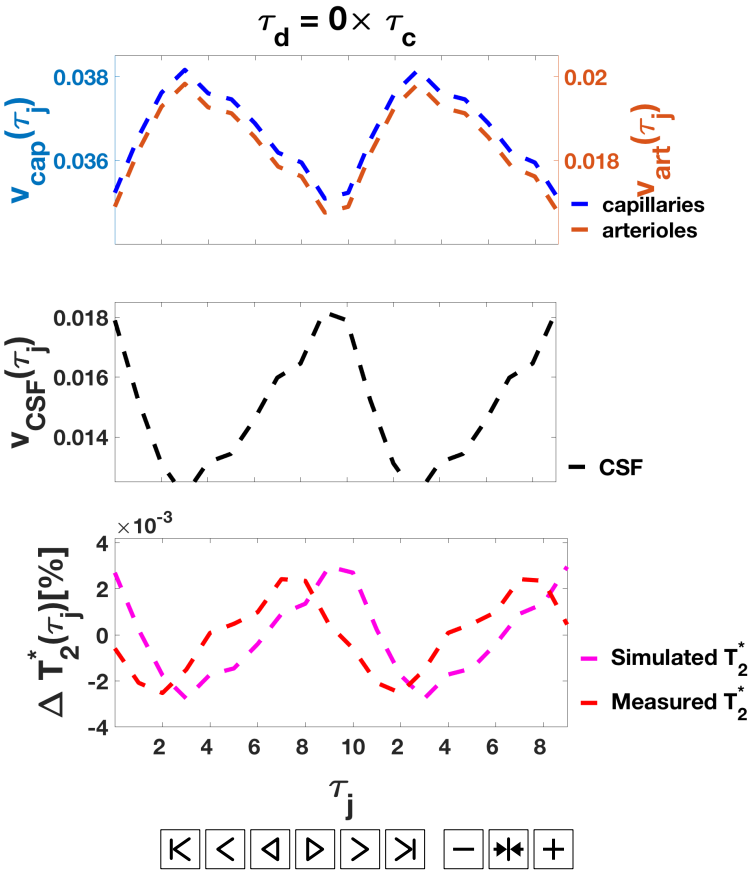


Figure 4.23: Simulation of the measured $T_2^*(\tau_j)$ with dynamic CSF. Top plot: the arteriolar blood volume fluctuation (orange) is fixed and the capillary/venule volume fluctuation (blue) is shifted w.r.t to it for all bins $\tau_d = 0...0.9 \times \tau_c$. Middle plot: CSF volume dynamically changes to conserve the voxel volume. Bottom plot: The resulting $T_2^*(\tau_j)$ waveform for all shifts (pink) is plotted against the measured waveform (red). The simulated waveform approximated the amplitude and slope of the measured waveform for a shift of $\tau_d \approx 0.8 \times \tau_c$. **A separate movie file is provided in the supplementary material uploaded in the digital submission.**

fit with the smallest χ^2 value of 4.69 was achieved with a scaling factor of $d = 30$. However, this χ^2 is associated with an $\alpha = 0.81$ value which indicates a much lower level of goodness of fit between the model and the data than the CSF partial volume model (see the green dotted line in Appendix B, Figure B.2). Further a scaling factor of $d = 30$ translates into an arteriolar CBV fluctuation of$+21.7\%$ to -20.4%, which is on the order of CBV changes during neuronal activation. We conclude that the dynamic parenchymal volume model is unlikely as expected from the Monro-Kellie doctrine on the incompressibility of intracranial tissue.

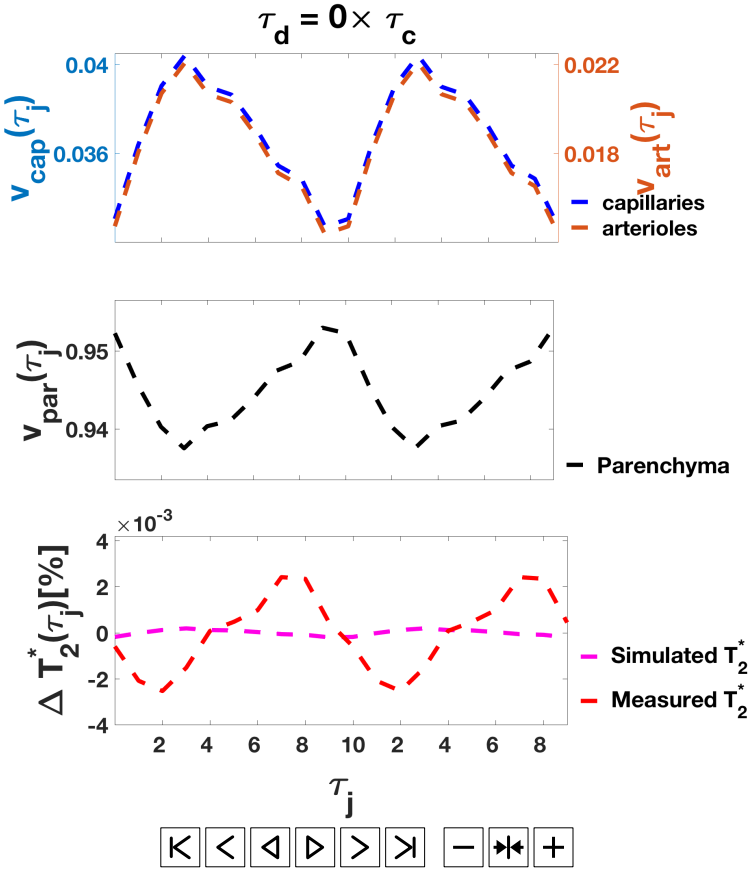


Figure 4.24: Simulation of the measured $T_2^*(\tau_j)$ with parenchymal volume fluctuations. Top plot: the arteriolar blood volume fluctuation (orange) is fixed and the capillary/venule volume fluctuation (blue) is shifted w.r.t to it for all delays $\tau_d = 0...0.9 \times \tau_c$. Middle plot: Parenchymal volume changes to conserve the voxel volume. Bottom plot: The resulting $T_2^*(\tau_j)$ waveform for all shifts (pink) is plotted against the measured waveform (red). The simulated waveform cannot approximate the measured waveform. **A separate movie file is provided in the supplementary material uploaded in the digital submission.**

4.5 Discussion and conclusion

Summary of key findings.

- The distribution of EPI signal phases at the cardiac frequency is tissue-specific.
- A dominant phase originates in the arterial structures and shifts throughout the tissue.
- Phases vary with different brain areas, with a particular shift between the cortical and deep GM phases. The overall bi-modal distribution in grey matter is a result of single-peak distributions in different areas that are shifted.
- Phase variations do not necessarily relate to a temporal delay in S_0 (i.e. CBV and CBF), but are caused by a variation in the magnitude of $S_0(\tau)$ and $T_2^*(\tau)$ waveforms and the relative timing of both waveforms to each other.
- $S_0(\tau)$ waveforms resemble features of the arterial pressure wave, with "dicrotic notch-like" characteristics that are potentially end-arteriolar reflected waves.
- Peak-to-peak $T_{2,p}^*$ fluctuation ranges are between $0.33\% - 0.5\%$ in GM and between $0.05\% - 0.25\%$ in WM.
- $T_2^*(\tau)$ waveforms tend to mirror $S_0(\tau)$, particularly in GM.

- A partial volume model, assuming a dynamic CSF compartment and a temporal delay between arteriolar and capillary CBV fluctuations is presented to simulate the measured $T_2^*(\tau_j)$ waveforms. The best match is achieved for a model of a systole-to-diastole arteriolar CBV fluctuation of +8.64% to −8.13% that is delayed by $0.8 \times \tau_c$ ($\approx 800\,\text{ms}$). However, the simulation is rather indicative as the p-value associated with the fit was 0.07, which is not significant.
- The hypothesised arteriolar CBV change is about half of what has been reported for neuronal activity-induced changes.

4.5.1 Critical points and limitations

Multiple factors may introduce inaccuracies into our results. This work entirely neglects the angular dependence of the signal. Variations in the orientation of vessels to the external B_0-field, particularly introduced by cortical folding, have been shown to introduce signal variations of up to 40% for the perpendicular case [196]. We further neglected T_1 effects which should change the longitudinal magnetisation $M_{z,i}$ in our models. T_1 variations will happen with partial volume as well as oxygenation variations. Further inaccuracies in the S_0 waveforms are introduced by the fitting process that assumes a mono-exponential decay. T_2^* fluctuations will cause a coupling into the S_0 intercept in the linearised model that was used for fitting and T_2^* and S_0 variations will be inversely correlated. Not all S_0 and T_2^* waveforms were anti-cyclic, but particularly the arterial mask showed an anti-cyclic behaviour that is likely enhanced by this effect. Additional inaccuracies are produced by the

unit cycle binning and temporal synchronisation of individual $S_0(\tau_j)/T_2^*(\tau_j)$ waveforms. This could introduce an underestimation of effects when all subjects' waveforms are averaged. The echo times ($TE_1/TE_2 = 21/52\,ms$) used in the scan protocol were a trade-off between slice coverage and producing enough contrast for GM and WM T_2^* fitting. Blood and CSF T_2^* values might be more inaccurate, particularly $T_{2,CSF}^*$ which is on the order of hundreds of milliseconds.

4.5.2 Cardiac-related phase distribution and S_0/T_2^* fluctuations

We found that the EPI signal at the cardiac frequency has a dominant phase that originates in the larger arterial structures. This phase disperses through tissue, and a second peak of approximate opposite phase evolves. The cortical phase distribution is closer to the arterial distribution, whereas deep GM structures, in particular the thalamus, shift away from the dominant arterial peak. The combination of the $S_0(\tau_j)/T_2^*(\tau_j)$ maps and the cardiac phase map gives an insight into the underlying cardiac cycle-related S_0 and T_2^* waveforms that we hypothesised to be the driver of the phase distribution. We found a strong S_0 pulsatility at the dominant arterial peak and a decline towards dispersing phases. This overall pattern fits well with the vascular architecture. The cortical surface is covered by the pial vessels and penetrating arterioles, both are immersed in CSF (the latter lying in the Virchow-Robin spaces) and have relatively fast flow (high $S_{0,p}$). Deeper structures are supplied by parenchymal arterioles, that are much slower in flow (low $S_{0,p}$) and are mainly surrounded by the astrocytic end-feet [197].

Intuitively, it is thought that a phase shift in the signal is caused by a delayed inflow, but we examined in the Theory section how both changes in

$S_{0,p}/T^*_{2,p}$ pulsatility as well as relative timing of $S_0(\tau)$ and $T^*_2(\tau)$ to one other can cause temporal signal shifts. In GM, we found the $S_0(\tau_j)$ waveform to peak in the fourth bin (out of ten) over the entire phase distribution, indicating a synchronous CBV/CBF fluctuation in this tissue and the phase shifts could be explained by a changing combination of S_0 and T^*_2. Interestingly, we found a strong variation in S_0 peak location over the phases in the WM. This could be an actual delay in inflow or a different behaviour in end-arteriolar reflected waves.

4.5.3 On the $\mathbf{T^*_2(\tau)}$ waveform

Even small increases in intracranial pressure pose severe health risks [198] and the question of how neuronal activity-induced CBV changes can be compensated for has been discussed by Turner et al. [199] and Krieger et al. [200] who proposed an exchange of water between the capillaries and the endothelium via permeable capillary walls. Here, we used a similar question - how is volume conserved during cardiac-induced CBV changes? - to explain the stable $T^*_2(\tau_j)$ waveforms that we measured in tissue. A dynamic partial volume model suggests an exchange of CSF during arteriolar dilation/constriction from systole to diastole, assuming a delay in blood volume fluctuations on the capillary side. The simulations indicate this delay to be approximately 800 ms (assuming an average cardiac frequency of 1 Hz). This delay between the arteriolar and capillary and venous blood volumes could potentially reflect transit times between both compartments. Arterial, as well as capillary transit times have been reported to be extremely heterogeneous in the brain. Chen et al. [201] report a microvascular transit times of about 1444 ms in humans using ASL measurements. A recent study by Larsson et al. [202] reports capillary transit times on the order of 900 ms.

Further our data suggest a baseline arteriolar CBV change of approximately +8.6% to −8.1% over the cardiac cycle. Arteriolar blood volume changes in grey matter have been reported by Huber et al. using VASO-fmri to be on the order of +16% during neuronal activation [195]. Further Warnert et al. [165] found the compliance in the major arteries of the Circle of Willis to be between 0.4% and 1.1% per mmHg. They calculated arterial compliance as $100\% \times [aCBV_{sys} - aCBVdia]/[aCBV_{dia} \times (P_{sys} - P_{dia})]$. We did not measure the blood pressure of our subjects. However, if we assume a change in blood pressure from systole to diastole of 60 mmHg, we find for the grey matter values stated above $100 * ((1.086 - 0.919)/(0.919 * 60) \approx 0.302\%/\text{mmHg}$. This value is as such smaller than in the study of Warnert et al. but compliance in the grey matter arteriovasculature is likely reduced.

It is noteworthy that not only partial volume changes with CSF, but any compartment with a long T_2^* (e.g. interstitial fluid) could lead to this observation. Recent glymphatic system research in the murine brain has shown CSF to enter the brain via the spaces surrounding the penetrating arteries [203], moving down paravascular pathways driven by cardiac pulsation [204]. A change in CSF partial volume during hypercapnia [205] and neuronal activation [206] has further been reported in VASO-fMRI data. Parenchymal volume fluctuations are unrealistic according to the Monro-Kellie doctrine of incompressible intercranial compartments. Our simulations support this hypothesis.

A complex interplay of cardiac-related changes in volume and flow, decreasing oxygenation levels down the microvascular network and variable transit times could also be the source of the measured $T_2^*(\tau_j)$ waveforms and our estimates of oxygen level variation-induced T_2^* changes were on the order of the observed fluctuations. In particular, in the deeper structures no CSF

should be assumed to contribute to the latter mechanism. Ultimately, a higher resolution study is needed to clarify these open questions.

4.5.4 Clinical relevance

There is a clinical interest in studying cerebral pulsatility. MRI could potentially study cerebrovascular and tissue-specific compliance pathways. Here, we were able to resolve distinct features in the single-subject S_0 waveform that might be a direct representative of arterial pulse wave patterns, such as the reflected backwards travelling wave. These patterns are known to vary along the vascular tree [207] and are markers of arterial stiffenning and vascular disease [208, 209]. As such, we hope that this study might ultimately contribute to methods that offer a clinical insight into cerebrovascular disease processes.

4.5.5 Brief summary of results

Cardiac cycle- induced EPI signals are temporally shifted from the cortex, that has a close matching in timing with the signals in arterial structures, towards subcortical areas that appear delayed. This is potentially of interest in physiological cleaning methods for fmri studies. These shifts are associated with different inflow S_0 and apparent T_2^* pulsatility over the course of the cardiac cycle. S_0 pulsatility is highest in areas that are more vascularised, like the cortex that is close to the arterial pial vasculature, compared to the subcortical areas that have a lower vascular densities and slower blood flow velocities. T_2^* fluctuations appear in grey as well as white matter and are likely a result of partial volume fluctuations between blood and CSF or interstitial fluid volumes. Blood volume changes over the course of the cardiac

cycle are of interest in research into cerebrovascular compliance, but more research is needed to understand the cardiac cycle-induced T_2^* fluctuations.

Chapter 5

Future work

5.1 DANTE for vessel-wall imaging at 7T

5.1.1 Motion correction and scan efficiency

We showed the feasibility of VWI at 7T using the DANTE-SPACE sequence in healthy volunteers and an exemplar patient. However, it is questionable if our VWI sequence could be robust in an elderly patient population that is more prone to subject movement. The two major points of concern are motion between TRs and during the readout echo train itself. A solution to between-TR motion could be the implementation of navigators for a prospective motion correction or a real-time encoding update. The TR used in our protocol was 2620 ms, but the DANTE module and SPACE readout only sum up to 300×1.6 ms+345ms = 825 ms, i.e. a dead time of 1795 ms is available. Gallichan et al. [210] recently presented 3D navigators that use fat-selective excitations (FatNavs) and implemented 3D FatNavs of about 1120 ms duration in a TSE sequence. This method has the advantage that the navigator excitation mitigates the disturbance of the water magnetisation.

Motion during a readout segment (within TR) renders the k-space data inconsistent and produces blurring and ghosting artefacts. Navigators have been used for 3D anatomical sequences [211] and 2D vessel-encoded arterial spin labeling [212] to detect and flag corrupted TRs for reacquisition. However, this would further prolong the already long scan time of our protocol ($\approx$ ten minutes).

To increase scan efficiency, it is of note that higher k-space acceleration factors (higher GRAPPA factor) will not lead to significant TR reductions. Higher GRAPPA factors will reduced the number of refocussing pulses that will reduce the overall SAR and allow for a reduction in TR. However our experience is that the reduction is not significant and image quality suffers with a further increase in parallel imaging. Developments in parallel transmission might ease this in the upcoming years.

Even if subject bulk movement could be addressed in a perfect manner the effect of physiological movement within the brain remains. Cardiac-induced brain motion and potentially pulsatile motion of the large intracranial vessels causes signal loss when motion-sensitizing preparations, such as DANTE, are used. Cardiac gating strategies, such as triggering to the cardiac cycle, could be an option to minimise unwanted signal loss [213]. The DANTE module could be triggered on the descending slope of the cardiac cycle to avoid DANTE preparation during systole. Again, this would prolong the already lengthy protocol and could cause signal level variations due to inconsistent recovery times between TRs. It remains questionable if DANTE, being a motion-sensitizing technique, is the ideal tool to tackle high resolution VWI as the structures of interest move which renders this technique inherently non-robust, especially if higher resolution is the aim. However, it might still be a sensible method for VWI in the neck and to image the carotid artery

wall which is thicker. The inversion strategies presented in Chapter 1 are more likely to avoid this effect and may be more promising.

Joint neck and head transmit coil arrays might become available in the future, giving a more extensive B_1 transmit field coverage, and it could be worth re-attempting DANTE-FLASH for intracranial VWI when such coil exists.

5.2 Cardiac-induced fluctuations in EPI time series

5.2.1 Methodologies

5.2.1.1 GLM approach to map cardiac fluctuations

We presented a GLM/ dual GLM in the frequency domain to identify significantly cardiac-modulated voxels. We did not compare this to the method of independant component analysis (ICA) [214, 215]. ICA decomposes the 4D fMRI data set into a subset of independent non-Gaussian sources with each component being a combination of a time course and an associated spatial map [216]. Single-subject cardiac components could be identified manually as recently outlined by Griffanti et al. [217, 218]. ICA can, for example, distinguish components in the ventricles from components in the arteries and it could be interesting to compare the cardiac ICA components with the refined spatial maps obtained with our dual GLM when run in specific tissue masks or brain areas.

5.2.1.2 Cardiac phase mapping

The temporal resolution of the multiband EPI used in our experiments is two orders of magnitude away from the critical Nyquist sampling rate to capture hypothetical signal fluctuations from pressure and shear wave-induced tissue displacement. In Chapter 4 we estimated that shear waves might travel one centimetre over the time of four milliseconds. Hence, at least a TR of two milliseconds is needed to detect phase changes over a few voxels. MR-encephalography (MREG) might have the potential to provide the needed sample rates. Whole brain sample rates of 23 ms at 2 mm in-plane resolution, using an undersampled rosette trajectory, have been reported [219]. A C2P package is available for Siemens' VB17, VD11 and VD13 platforms. The cardiac phase mapping algorithm could be applied to MREG data to test if a phase dispersion is detectable (recall that the minimum phase resolution is inversely proportional to the maximum resolvable frequency). However, the phase offset correction from the acquisition timing (Eq. 4.11) for a 3D rosette sampling scheme would need more thought.

5.2.1.3 Mapping MR variables over the cardiac cycle

In Chapter 4 we used GRE signals and a multi-echo contrast to study S_0 and T_2^* waveforms over the cardiac cycle, but any MR signal (and derived variable) could be mapped, given a cardiac trigger is measured during the acquisition (an intrinsic reference, such as a CSF ROI in the cererbal aqueaduct, or a vessel in the scalp may even be sufficient). Particularly relevant are inversion-prepared sequences that allow the nulling of specific tissue compartments. A mapping of a CSF-nulled EPI would make a good starting point to further investigate the dynamic partial volume models we proposed. Renvall et al. [220, 221] developed a multi-inversion EPI that has been used

to image each slice at multiple TIs. It could also be used to guarantee an identical TI for all slices, accounting for the acquisition timing at readout. Besides using it for CSF-nulling it may offer the possibility to quantify T_1 changes over the cardiac cycle. The effective nulling time of a voxel should be altered by oxygen or partial volume induced fluctuations in T_1. A scan with the TI of GM could be acquired to plot the signal variations over the cardiac cycle.

5.2.2 Neuroscientifically relevant ideas

A more profound knowledge of vascular baseline fluctuations is a requisite for future research into changes with disease or ageing. Our estimate of baseline CBV fluctuations from systole to diastole (Chapter 4) should be investigated further with higher resolution experiments. Higher resolution is likely to change the narrative of our data interpretation as it reduces partial volume effects. Increased spatial resolution could be achieved by restricting the coverage. In chapter 4 we used the experimentally measured S_0 waveforms to simulate potential changes in partial volumes that explain the T_2^*-waveforms. However, this simulation was restricted to the voxels that showed an EPI signal fluctuation at the dominant arterial phase value as S_0 was maximised in this regime. Areas have negligible or no significant S_0 waveforms over the cardiac cycle cannot be modelled. The S_0 detectability is reduced in the deeper structures where flow velocities decline and a reduced slice coverage should improve the inflow effect. Depending on the area of interest, imaging volumes could be tilted perpendicular to the expected vessel orientation or even multiple scans with rotated slice orientations could be acquired.

5.2.2.1 Glymphatic system theory

In the Discussion of Chapter 4 we hypothesised a link between the cardiac-related T_2^* waveforms and glymphatic system mechanisms. This should be addressed in future work. The reverse modelling of the measured T_2^* waveforms suggests dynamic volume fluctuations with the driving mechanism in the arterial volume pulsation. The detectability of T_2^* waveforms in the deeper structures and white matter, where no CSF should be located, implies another interchangeable component with a longer T_2^* than GM. Interstitial fluid (ISF) would be a possible candidate. ISF and the extracelluar matrix make up $15\% - 20\%$ of the total brain volume [222]. ISF movement has gathered enormous research attention throughout the last decade and is thought to be involved in waste removal and drainage pathways in the brain's deeper GM structures and in WM (see Lei et al. for a comprehensive and recent review [222]). Again, higher spatial resolution and fewer slices covering only deeper structures could help to investigate if we can actually measure this phenomenon.

Simulated hypothesis

High-resolution data with more inflow effect is desirable. As a starting point, and complementary to such experimental data, we can use the multi-exponential voxel model to "dig" for the MR-properties of a hypothetically exchanging compartment. In Chapter 4 we restricted our simulations to estimated MR-parameters of CSF. In the deeper cortical layers and in particular deep GM and WM we expect ISF to act as the mobile compartment, and could search the parameter space for the best fit to the measured $T_2^*(\tau_j)$

waveforms simulating

$$S_{multi}(\tau_j) = \sum_i v_i(\tau_j)\,\rho_i\,M_{z,i}{\cdot}exp\left\{\frac{-\mathrm{TE}}{T^*_{2,i}}\right\} + v_{\mathrm{ISF}}(\tau_j)\;\underbrace{\rho_{\mathrm{ISF}}}_{?}\;\underbrace{M_{z,\mathrm{ISF}}}_{?}\cdot exp\left\{\frac{\mathrm{TE}}{\underbrace{T^*_{2,\mathrm{ISF}}}_{?}}\right\} \tag{5.1}$$

where "?" marks the parameters to test for (it should be noted that $M_{z,\mathrm{ISF}}$ will actually be varied by varying T_1 values).

To pilot this idea we ran simulations with the GM data, using the $S_0(\tau_j)$ waveform at the dominant cardiac frequency $\phi_c = -\pi/2 \pm 0.3$ rad (recall that the $S_0(\tau_j)$ at larger ϕ_c was not reliably detected) to find the three parameters $[\rho, T_1, T_2^*]$ that give the best match with the measured $T_2^*(\tau_j)$ at different phase values. Here, we present the results for $\phi_c = 0 \pm 0.3$ rad and $\phi_c = +\pi/2 \pm 0.3$ rad (frames 10 and 16 in the animated Figure 4.19 of Chapter 4).

Figure 5.1a) shows the best matching simulated $T_2^*(\tau_j)$, plotted with the measured waveform for the phase range of $\phi_c = 0 \pm 0.3$ rad. The gof from Eq. 4.18 was used to quantify the goodness of fit (the closer to zero, the better the match). The best match has a gof of 0.4. The shift between arteriolar and capillary CBV fluctuation is $0.7 \times \tau_c$ (which is about ≈ 700 ms for the average subject) and the scaling factor translates to a systole-to-diastole arteriolar CBV change of +12.5% to −11.6%. The parameters of the best matching dynamic volume compartment are $\rho = 1$, $T_2^* = 60$ ms and $T_1 = 3100$ ms.

Figure 5.1b) shows the best matching simulated $T_2^*(\tau_j)$, plotted with the measured waveform for the phase range of $\phi_c \approx \pi/2 \pm 0.3$ rads. Here, the gof is 0.51. The shift between arteriolar and capillary CBV fluctuation is $0.6 \times \tau_c$

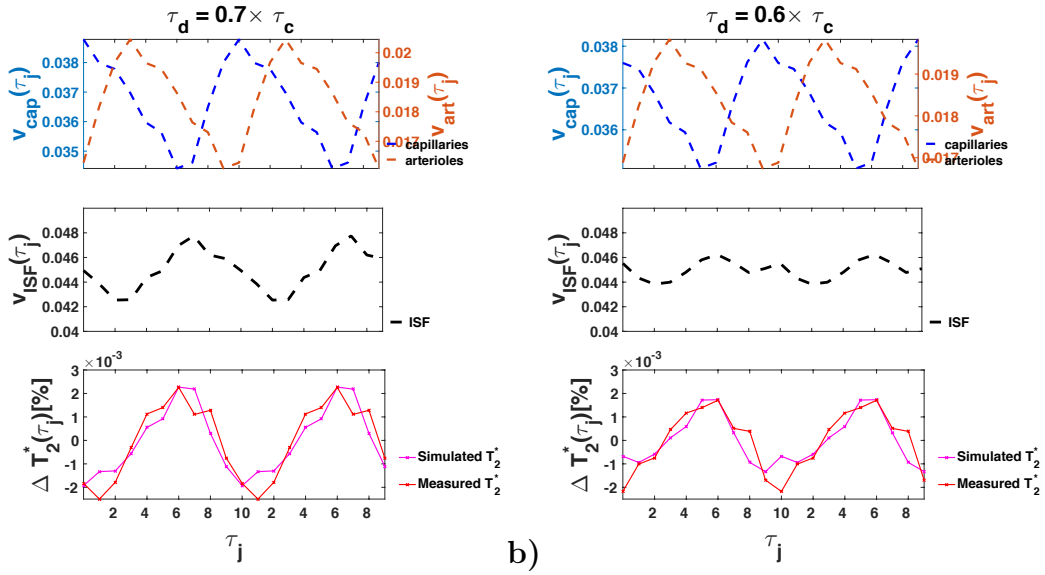


Figure 5.1: Simulation of $T_2^*(\tau_j)$ at the cardiac phase values of $\phi_c = 0 \pm 0.3$rad (a) and $\phi_c = \pi/2 \pm 0.3$ rad (b). The simulated $T_2^*(\tau_j)$ (pink) refer to the "best match" (minimal gof). The MR-parameters of the dynamic ISF compartment (ρ, T_1, T_2^*) of this best match are described in the text.

(which is about $\approx$ 600 ms for the average subject) and the scaling factor relates to a systole-to-diastole arteriolar CBV change of +8.68% to −8.16%. The parameters of the dynamic volume compartment are $\rho = 0.8$, $T_2^* = 220$ ms and $T_1 = 4300$ ms. The error between simulation and data is not satisfying and the above simulation results should be regarded as indicators only. However, the values obtained hint towards a dynamic compartment with longer T_2^* and T_1 values than GM itself. As such, the hypothesis of dynamic ISF might not be too far fetched.

5.2.2.2 Vascular anatomical network model to simulate cardiac-induced MR signals

An ambitious future project could be the modeling of area- or layer-specific cardiac-induced GRE signals (and spin-echo as well). Markuerkiaga et al.

[223] recently presented modeling work of layer-specific BOLD PSFs. In analogy to this work the multi-compartment model from Chapter 4 could be used to simulate the cardiac-induced GRE signals in voxels of different tissue composition. Vessel size and density distributions could be taken from vascular anatomical network models (VANs) as measured in animal studies [190, 224]. VANs have been used to disentangle the microvascular dynamics of the BOLD HRF to predict macroscopic BOLD responses. The impressive predictive power of this BOLD VAN has been demonstrated by estimations of the variation of the human BOLD response with cortical folding (vessel orientation to B_0) [196]. Although basically nothing is known about the cerebral CBV and CBF dynamics at the cardiac frequency (except for our estimates) this uncertain parameter space could be explored in simulations and validated against experimental data, as discussed in the previous section. As a challenging project a cerebral VAN model to simulate cardiac-induced MR signals would be enormously powerful. If such a model existed it could guide clinically relevant questions where changes in vascular architecture and elasticity are implied.

5.2.3 Clinically relevant ideas

If future research could reproduce and validate our estimates of arteriolar CBV changes it could be a potential means to study arteriolar and capillary resistance. Cerebral compliance is a topic of interest in normal ageing and vascular diseases where wall stiffening is implied. The end-arteriolar reflections that we observed particularly in GM suggest that it is feasible to study cerebrovascular resistance *in-vivo* with regional specificity. Current methods comprise ultrasound, cine-MRI, finger photoplethysmography and pressure transducers [225], all of which are either not applicable to the brain at all or

are limited in spatial specificity.

A potential first step would be a study into the intra- and inter-subject variability of the magnitude of fluctuations ($S_{0,p}$ and $T^*_{2,p}$) and also the variation in the "dicrotic-notch-like" structures of the waveforms (timing within cardiac unit cycle, tissue specificity etc.). This should be conducted in healthy subjects and matching age. Once more knowledge is gained on the natural variability of these observations a subsequent step could involve a vascular intervention, ideally a controlled CO_2-challenge (e.g. with a Respiract system). CO_2 is a vasodilator and increases CBV and CBF [226, 227]. The hypercapnic state should reduce the ability of the vasculature to dilate and contract and shift the location of reflections along the $S_0(\tau_c)$ waveform towards systole as the wave should be reflected earlier. Further, CBV and CBF pulsatility should be decreased. It would be interesting to test if there was an increase in detectable $S_{0,p}$ in white matter and subcortical areas where flow is too slow during normocapnia, but increased during hypercapnia. The hypercapnic state could be regarded as a model of vascular stiffness where vessel elasticity and pulsatility is reduced, but pulsatility is expected to travel further down the vascular tree and a shift in the timing of the reflections in the waveforms could be induced. This would be interesting with regard to our findings from Chapter 3, where the older study population showed decreased BOLD power in WM, but an overall larger extent of detectable fluctuations.

Bibliography

[1] J Weinberger. Diagnosis and prevention of atherosclerotic cerebral infarction. *CNS spectrums*, 10(07):553–566, 2005.

[2] D W Paquette, N Brodala, and T C Nichols. Cardiovascular disease, inflammation, and periodontal infection. *Periodontology 2000*, 44(1):113–126, 2007.

[3] Z A Fayad and V Fuster. Clinical imaging of the high-risk or vulnerable atherosclerotic plaque. *Circulation Research*, 89(4):305–316, 2001.

[4] T Saam, T S Hatsukami, N Takaya, B Chu, H Underhill, W S Kerwin, J Cai, M S Ferguson, and C Yuan. The vulnerable, or high-risk, atherosclerotic plaque: Noninvasive mr imaging for characterization and assessment 1. *Radiology*, 244(1):64–77, 2007.

[5] French Study of Aortic Plaques in Stroke Group et al. Atherosclerotic disease of the aortic arch as a risk factor for recurrent ischemic stroke. *N Engl j Med*, 1996(334):1216–1221, 1996.

[6] A Cohen, C Tzourio, B Bertrand, C Chauvel, M-G Bousser, and P Amarenco. Aortic plaque morphology and vascular events. *Circulation*, 96(11):3838–3841, 1997.

[7] Zahi A. Fayad, Valentin Fuster, Konstantin Nikolaou, and Christoph Becker. Computed tomography and magnetic resonance imaging for noninvasive coronary angiography and plaque imaging: Current and potential future concepts. *Circulation*, 106(15):2026–2034, 2002.

[8] Met R, Bipat S, Legemate D A, Reekers J A, and Koelemay M W. Diagnostic performance of computed tomography angiography in peripheral arterial disease: A systematic review and meta-analysis. *JAMA*, 301(4):415–424, 2009.

[9] F Prati, E Regar, G S Mintz, E Arbustini, C Di Mario, I K Jang, T Akasaka, M Costa, G Guagliumi, E Grube, Y Ozaki, F Pinto, and P W J Serruys. Expert review document on methodology, terminology, and clinical applications of optical coherence tomography: Physical principles, methodology of image acquisition, and clinical application for assessment of coronary arteries and atherosclerosis. *European Heart Journal*, 31(4):401–415, 2010.

[10] A Wahle, J J. Lopez, M E. Olszewski, S C. Vigmostad, K B. Chandran, J D. Rossen, and M Sonka. Plaque development, vessel curvature, and wall shear stress in coronary arteries assessed by x-ray angiography and intravascular ultrasound. *Medical Image Analysis*, 10(4):615 – 631, 2006. Special Issue on Functional Imaging and Modelling of the Heart (FIMH 2005).

[11] P Pignoli, E Tremoli, a Poli, P Oreste, and R Paoletti. Intimal plus medial thickness of the arterial wall: a direct measurement with ultrasound imaging. *Circulation*, 74(6):1399–1406, 1986.

[12] S E. Nissen and P Yock. Intravascular ultrasound. *Circulation*, 103(4):604–616, 2001.

[13] Z A Fayad, V Fuster, J T Fallon, T Jayasundera, S G Worthley, G Helft, J G Aguinaldo, J J Badimon, and S K Sharma. Noninvasive In Vivo Human Coronary Artery Lumen and Wall Imaging Using Black-Blood Magnetic Resonance Imaging. *Circulation*, 102(5):506–510, 2000.

[14] M Naghavi, P Libby, E Falk, S W Casscells, S Litovsky, J Rumberger, J J Badimon, C Stefanadis, P Moreno, G Pasterkamp, Z Fayad, P H Stone, S Waxman, P Raggi, M Madjid, A Zarrabi, A Burke, C Yuan, P J Fitzgerald, D S Siscovick, C L de Korte, M Aikawa, K E Juhani Airaksinen, G Assmann, C R Becker, J H Chesebro, A Farb, Z S Galis, C Jackson, I-K Jang, W Koenig, R A Lodder, K March, J Demirovic, M Navab, S G Priori, M D Rekhter, R Bahr, S M Grundy, R Mehran, A Colombo, E Boerwinkle, C Ballantyne, W Insull, R S Schwartz, R Vogel, P W Serruys, G K Hansson, D P Faxon, S Kaul, H Drexler, P Greenland, J E Muller, R Virmani, P M Ridker, D P Zipes, P K Shah, and J T Willerson. From vulnerable plaque to vulnerable patient. *Circulation*, 108(14):1664–1672, 2003.

[15] R H Swartz, S S Bhuta, R I Farb, R Agid, R A Willinsky, K G, J Butany, B A Wasserman, D M Johnstone, F L Silver, and D J Mikulis. Intracranial arterial wall imaging using high-resolution 3-tesla contrast-enhanced MRI. *American Academy of Neurology*, 72(7):627–634, 2009.

[16] A Millon, L Boussel, M Brevet, J-L Mathevet, E Canet-Soulas, J-Y Mory, Cand Scoazec, and P Douek. Clinical and histological significance of gadolinium enhancement in carotid atherosclerotic plaque. *Stroke*, 43(11):3023–3028, 2012.

[17] C Calcagno, V Mani, S Ramachandran, and Z A. Fayad. Dynamic contrast enhanced (dce) magnetic resonance imaging (mri) of atherosclerotic plaque angiogenesis. *Angiogenesis*, 13(2):87–99, 2010.

[18] C Calcagno, S Ramachandran, A Millon, P M Robson, V Mani, and Z Fayad. Gadolinium-based contrast agents for vessel wall magnetic resonance imaging (mri) of atherosclerosis. *Current cardiovascular imaging reports*, 6(1):11–24, 2013.

[19] S Kelle, K Schlendorf, G A Hirsch, G Gerstenblith, E Fleck, R G Weiss, and M Stuber. Gadolinium enhanced mr coronary vessel wall imaging at 3.0 tesla. *Cardiology research and practice*, 2010.

[20] C M Fisher. The arterial lesions underlying lacunes. *Acta Neuropathologica*, 12(1):1–15, 1969.

[21] E L. Bailey, C Smith, C L M Sudlow, and J M Wardlaw. Pathology of lacunar ischemic stroke in humans - A systematic review. *Brain Pathology*, 22(5):583–591, 2012.

[22] N Dieleman, A G van der Kolk, S J van Veluw, C JM Frijns, A A Harteveld, P R Luijten, and J Hendrikse. Patterns of intracranial vessel wall changes in relation to ischemic infarcts. *Neurology*, 83(15):1316–1320, 2014.

[23] N Dieleman, A G van der Kolk, J J M Zwanenburg, A Harteveld, G J Biessels, P R Luijten, and J Hendrikse. Imaging intracranial vessel wall pathology with magnetic resonance imaging: current prospects and future directions. *Circulation*, 130(2):192–201, 2014.

[24] M D Alexander, C Yuan, A Rutman, D L Tirschwell, G Palagallo, D Gandhi, L N Sekhar, and M Mossa-Basha. High-resolution intracranial vessel wall imaging: imaging beyond the lumen. *Journal of Neurology, Neurosurgery & Psychiatry*, 87(6):589–597, 2016.

[25] M Kontzialis and B A Wasserman. Intracranial vessel wall imaging: current applications and clinical implications. *Neurovascular Imaging*, pages 2–7, 2016.

[26] P Benjamin, O Viessmann, A D MacKinnon, P Jezzard, and H S Markus. 7 tesla mri in cerebral small vessel disease. *International Journal of Stroke*, 10(5):659–664, 2015.

[27] M Mossa-Basha, M Alexander, S Gaddikeri, C Yuan, and D Gandhi. Vessel wall imaging for intracranial vascular disease evaluation. *Journal of neurointerventional surgery*, 8(11):1154–1159, 2016.

[28] E Moser, F Stahlberg, M E Ladd, and S Trattnig. 7-T MR–from research to clinical applications? *NMR in biomedicine*, 25(5):695–716, 2012.

[29] R R Edelman, D Chien, and D Kim. Fast Selective Black Blood MR Imaging. *Radiology*, 181:655–660, 1991.

[30] H K Song, A C Wright, R L Wolf, and F W Wehrli. Multislice Double Inversion Pulse Sequence for Efficient Black-Blood MRI. *Magnetic Resonance in Medicine*, 620(3):616–620, 2002.

[31] W D Rooney, G Johnson, X Li, E R Cohen, S-G Kim, K Ugurbil, and C S Springer. Magnetic field and tissue dependencies of human brain longitudinal 1H2O relaxation in vivo. *Magnetic Resonance in Medicine*, 57(2):308–18, 2007.

[32] B Simon, S Schmidt, C Lukas, J Gieseke, F Träber, D L Knol, WA Willinek, J Geurts, H Schild, and F Barkhof. Improved in vivo detection of cortical lesions in multiple sclerosis using double inversion recovery mr imaging at 3 tesla. *European radiology*, 20(7):1675–1683, 2010.

[33] J Wang, V L Yarnykh, T Hatsukami, Baocheng Chu, Niranjan Balu, and Chun Yuan. Improved Suppression of Plaque-Mimicking Artifacts in Black-Blood Carotid Atherosclerosis Imaging Using a Turbo Spin-Echo (TSE) Sequence. *Magnetic Resonance in Medicine*, 58(5):973–981, 2007.

[34] T Yoshiura, A Hiwatashi, M Obara, K Yamashita, H Kamano, Y Takayama, and K Kobayashi. Sensitized Driven-Equilibrium Preparation for Detection of Brain Metastases on 3T MR Imaging. *American Journal of Neurology*, 85:113–127, 2011.

[35] M Obara, K Kuroda, J Wang, M Honda, M Yoneyama, Y Imai, and M Van Cauteren. Comparison between two types of improved motion-sensitized driven-equilibrium (iMSDE) for intracranial black-blood imaging at 3.0 tesla. *Journal of magnetic resonance imaging*, 40(4):824–31, 2014.

[36] DW McRobbie. Occupational exposure in mri. *The British journal of radiology*, 85:293–312, 2012.

[37] L Alexander, H R Buswell, Y Sun, B E Chapman, J S Tsuruda, and D L Parker. Intracranial black-blood MR angiography with high-resolution 3D fast spin echo. *Magnetic Resonance in Medicine*, 40(2):298–310, 1998.

[38] M Yoneyama, M Nakamura, T Tabuchi, A Takemura, and M Obara. Optimization of 3d-variable refocusing flip angle rare imaging for high-resolution volumetric black-blood angiography. *Radiological physics and technology*, 5(2):270–276, 2012.

[39] J W Grinstead, W Rooney, and G Laub. The origins of bright blood MPRAGE at 7 Tesla and a simultaneous method for T1 imaging and non-contrast MRA. *Proceedings of the International Society of Magnetic Resonance in Medicine*, 18:1429, 2010.

[40] F Visser, J J M Zwanenburg, J M Hoogduin, and P R Luijten. High-resolution magnetization-prepared 3D-FLAIR imaging at 7.0 Tesla. *Magnetic Resonance in Medicine*, 64(1):194–202, 2010.

[41] J P Mugler. Signal and Contrast Properties of Very-Long Spin-Echo Trains for 3D T2-weighted Turbo-Spin-Echo Imaging. *Proceedings of the International Society of Magnetic Resonance in Medicine*, page 1716, 2007.

[42] R F Busse, H Hariharan, A Vu, and J H Brittain. Fast spin echo sequences with very long echo trains: design of variable refocusing flip angle schedules and generation of clinical T2 contrast. *Magnetic Resonance in Medicine*, 55(5):1030–7, 2006.

[43] R F Busse, A C S Brau, A Vu, C R Michelich, E Bayram, R Kijowski, S B Reeder, and H Rowley. Effects of refocusing flip angle modulation and view ordering in 3D fast spin echo. *Magnetic Resonance in Medicine*, 60(3):640–9, 2008.

[44] Y Qiao, D Steinman, Q Qin, M Etesami, M Schär, B C Astor, and B Wasserman. Intracranial arterial wall imaging using three-dimensional high isotropic resolution black blood MRI at 3.0 Tesla. *Journal of magnetic resonance imaging*, 34(1):22–30, 2011.

[45] M P Lichy, B Wietek, J P Mugler Iii, W Horger, M Menzel, K Siegmann, P Martirosian, and B Kiefer. Whole-body applications of isotropic high-resolution T2-weighted MRI with a single slab 3D-TSE based sequence optimized for high sampling efficiency , called SPACE – initial clinical experiences . *Proceedings of the International Society of Magnetic Resonance in Medicine*, page 794, 2005.

[46] G a Morris and R Freeman. Selective excitation in Fourier transform nuclear magnetic resonance. 1978. *Journal of magnetic resonance (San Diego, Calif. : 1997)*, 213(2):214–43, 2011.

[47] T J Mosher and Smith B. A Dante Tagging Sequenced for the Evaluation of Translation Sample Motion. *Magnetic Resonance in Medicine*, 15:334–339, 1990.

[48] ES H Ibrahim. Myocardial tagging by cardiovascular magnetic resonance: evolution of techniques–pulse sequences, analysis algorithms, and applications. *Journal of Cardiovascular Magnetic Resonance*, 13(1):36, 2011.

[49] L Li, K L Miller, and P Jezzard. DANTE-prepared pulse trains: a novel approach to motion-sensitized and motion-suppressed quantitative magnetic resonance imaging. *Magnetic Resonance in Medicine*, 68(5):1423–38, 2012.

[50] M Markl, M T Alley, C J Elkins, and N J Pelc. Flow Effects in Balanced Steady State Free Precession Imaging. *Magnetic Resonance in Medicine*, 50(5):892–903, 2003.

[51] L Li, J T Chai, L Biasiolli, M D Robson, R P Choudhury, A I Handa, J Near, and P Jezzard. Black-Blood Multicontrast Imaging of Carotid Arteries with DANTE-prepared 2D and 3D MR Imaging. *Radiology*, 273(2):560–9, 2014.

[52] Y Xie, Q Yang, G Xie, J Pang, Z Fan, and D Li. Improved black-blood imaging using dante-space for simultaneous carotid and intracranial vessel wall evaluation. *Magnetic resonance in medicine*, 75(6):2286–2294, 2016.

[53] L Li, Y Kong, Y Zaitsu, L Matthews, J Palace, and P Jezzard. Structural imaging of the cervical spinal cord with suppressed csf signal using dante pulse trains. *Magnetic resonance in medicine*, 74(4):971–977, 2015.

[54] J Wang, M Helle, Z Zhou, P Börnert, T S Hatsukami, and C Yuan. Joint blood and cerebrospinal fluid suppression for intracranial vessel wall mri. *Magnetic resonance in medicine*, 75(2):831–838, 2016.

[55] S G van der Kolk, J J M Zwanenburg, M Brundel, G-J Jan Biessels, F Visser, P R Luijten, and J Hendrikse. Intracranial vessel wall imaging at 7.0-T MRI. *Stroke*, 42(9):2478–84, 2011.

[56] A G van der Kolk, J Hendrikse, M Brundel, G J Biessels, E J Smit, F Visser, P R Luijten, and J J M Zwanenburg. Multi-sequence whole-brain intracranial vessel wall imaging at 7.0 tesla. *European radiology*, 23(11):2996–3004, 2013.

[57] E M Haacke, R W Brown, M R Thompson, and R Venkatesan. *Magnetic Resonance Imaging: Physical Principles and Pulse Sequence Design*. John Wiley & Son, New York, 1999.

[58] RM Henkelman, GJ Stanisz, and SJ Graham. Magnetization transfer in mri: a review. *NMR in Biomedicine*, 14(2):57–64, 2001.

[59] O Bieri and K Scheffler. On the origin of apparent low tissue signals in balanced SSFP. *Magnetic Resonance in Medicine*, 56(5):1067–74, 2006.

[60] G J Stanisz, E E Odrobina, J Pun, M Escaravage, S J Graham, M J Bronskill, and R M Henkelman. T1, T2 relaxation and magnetization transfer in tissue at 3T. *Magnetic Resonance in Medicine*, 54(3):507–12, 2005.

[61] SL Talagala, TQ Li, H Merkle, S Wang, J Bodurka, P Van Gelderen, and J Duyn. Comparison of continuous arterial spin labeling perfusion mri at 7t and 3t. *Proceedings of the 16th Annual Meeting of ISMRM*, page 1916, 2008.

[62] W M Luh, S L Talagala, T Q Li, and P A Bandettini. Pseudo-continuous arterial spin labeling at 7 T for human brain: Estimation and correction for off-resonance effects using a Prescan. *Magnetic Resonance in Medicine*, 69(2):402–410, 2013.

[63] S Trattnig, E Springer, W Bogner, G Hangel, B Strasser, B Dymerska, P L Cardoso, and S D Robinson. Key clinical benefits of neuroimaging at 7T. *NeuroImage*, 2016.

[64] O Viessmann, L Li, P Benjamin, and P Jezzard. T2-Weighted intracranial vessel wall imaging at 7 Tesla using a DANTE-prepared variable flip angle turbo spin echo readout (DANTE-SPACE). *Magnetic Resonance in Medicine*, 77(2):655–663, 2017.

[65] Grinstead J W, O Speck, D Paul, L Silbert, L amd Perkins, and Rooney W. Whole-Brain FLAIR using 3D TSE with Variable Flip Angle Readouts Optimized for 7 Tesla. *Proceedings of the International Society of Magnetic Resonance in Medicine*, page 3034, 2010.

[66] J P Mugler, B Kiefer, and J R Brookeman. Three-Dimensional T2-Weighted Imaging of the Brain Using Very Long Spin-Echo Trains. *Proceedings of the International Society of Magnetic Resonance in Medicine*, page 35142, 2000.

[67] E F Cox and P Gowland. Simultaneous quantification of T2 and T2' using a combined gradient echo-spin echo sequence at ultrahigh field. *Magnetic Resonance in Medicine*, 64(5):1441–1446, 2010.

[68] E Cox and P Gowland. Measuring T2 and T2' in the brain at 1.5T, 3T and 7T using a hybrid gradient echo-spin echo sequence and EPI. *Proceedings 16th Scientific Meeting, International Society for Magnetic Resonance in Medicine*, Toronto:1411, 2008.

[69] R Sarkar. *Measurement of T 1 in the Vessel Wall Using MRI*. PhD thesis, University of Toronto, 2011.

[70] L Biasiolli, A C Lindsay, J T Chai, R P Choudhury, and M D Robson. In-vivo quantitative T2 mapping of carotid arteries in atherosclerotic patients: segmentation and T2 measurement of plaque components. *Journal of cardiovascular magnetic resonance : official journal of the Society for Cardiovascular Magnetic Resonance*, 15(1):69, 2013.

[71] W Koning, A a.J. de Rotte, J J Bluemink, T van der Velden, P R Luijten, D W J Klomp, and J J M Zwanenburg. MRI of the carotid artery at 7 Tesla: Quantitative comparison with 3 Tesla. *Journal of Magnetic Resonance Imaging*, 780:773–780, 2013.

[72] H K Lee, J K Kim, H J Kim, and J K Park. CSF Flow Quantification of the Cerebral Phase Contrast Cine MR Imaging. *Korean Journal of Radiology*, 5(June):81–86, 2004.

[73] M Kolbitsch, I Schocke, C Lorenz, F Kremser, K Zschiegner, S Pfeiffer, F Felberg, C Aichner, and A Hoermann. Phase-contrast MRI Measurements of Systolic Cerebrospinal Fluid Peak Velocity (CSFV peak) in the Aqueduct of Sylvius. *Anesthesiology*, 90:1546–50, 1999.

[74] C Wu, S Prabhakaran, T Carroll, P Vakil, N Chatterjee, A Honarmand, S Ansari, J Carr, and M Markl. Comprehensive Hemodynamic Evaluation of Intracranial Atherosclerotic Disease with 4D Flow MR Imaging. *Proceedings of the International Society of Magnetic Resonance in Medicine*, 22:516, 2014.

[75] M Wyss, T Kirchner, A Ringenbach, K Prüssmann, and A Henning. Relaxation parameter mapping adapted for 7t and validation against optimized single voxel mrs. *Proceedings of the 21st Annual Meeting of ISMRM, Salt Lake City, USA*, page 2464, 2013.

[76] J C Rane and S Gore. NIH Public Access. *NIH Public Access*, 29(6):997–1003, 2012.

[77] R Wirestam, R Wirestam, D Greitz, D Greitz, M B E Olsson, M B E Olsson, F Stahlberg, F Stahlberg, and S Brockstedt. Theoretical and Experimental Evaluation of Phase-Dispersion Effects Caused by Brain Motion in Diffusion and Perfusion MR Imaging. *Journal of magnetic resonance imaging*, 6(14):348–355, 1996.

[78] D Greitz, R Wirestam, A Franck, B Nordell, C Thomsen, and N Stahlberg. Pulsatile brain movement and associated hydrodynamics studied by magnetic resonance phase imaging. The Monoro-Kellie doctrine revisited. *Neuroradiology*, 34:370–380, 1992.

[79] P M Robson, A K Grant, A J Madhuranthakam, R Lattanzi, D K Sodickson, and C Mckenzie. Comprehensive Quantification of SNR Ratio and g-Factor for Image-Based and k-space Based Parallel Imaging Reconstructions. *Magnetic Resonance in Medicine*, 60(4):895–907, 2010.

[80] M Jenkinson, P Bannister, M Brady, and S Smith. Improved optimization for the robust and accurate linear registration and motion correction of brain images. *NeuroImage*, 17(2):825–841, 2002.

[81] J L R Andersson, M Jenkinson, S Smith, et al. Non-linear registration, aka spatial normalisation fmrib technical report tr07ja2. *FMRIB Analysis Group of the University of Oxford*, 2, 2007.

[82] F Eggenschwiler, K R O'Brien, R Gruetter, and J P Marques. Improving T2-weighted imaging at high field through the use of kT-points. *Magnetic Resonance in Medicine*, 71(4):1478–1488, 2014.

[83] K Setsompop, V Alagappan, B Gagoski, T Witzel, J R Polimeni, A Potthast, F Hebrank, U Fontius, F Schmitt, L L Wald, et al. Slice-selective rf pulses for in vivo b 1+ inhomogeneity mitigation at 7 tesla using parallel rf excitation with a 16-element coil. *Magnetic resonance in medicine*, 60(6):1422–1432, 2008.

[84] B B Biswal, M Mennes, X-N Zuo, S Gohel, C Kelly, S M Smith, C F Beckmann, Jo S Adelstein, R L Buckner, S Colcombe, A-M Dogonowski, M Ernst, D Fair, M Hampson, M J Hoptman, J S Hyde, V J Kiviniemi, R Kötter, S-J Li, C-P Lin, M J Lowe, C Mackay, D J Madden, K H Madsen, D S Margulies, H S Mayberg, K McMahon, C S Monk, S H Mostofsky, B J Nagel, J J Pekar, S J Peltier, S E Petersen, V Riedl, S A R B Rombouts, B Rypma, B L Schlaggar, S Schmidt, R D Seidler, G J Siegle, C Sorg, G-J Teng, J Veijola, A Villringer, M Walter, L Wang, X-C Weng, S Whitfield-Gabrieli, P Williamson, C Windischberger, Y-F Zang, H-Y Zhang, F X Castellanos, and M P Milham. Toward discovery science of human brain function. *Proceedings of the National Academy of Sciences of the United States of America*, 107(10):4734–4739, 2010.

[85] M D Greicius, B Krasnow, A L Reiss, and V Menon. Functional connectivity in the resting brain: a network analysis of the default mode hypothesis. *Proceedings of the National Academy of Sciences of the United States of America*, 100(1):253–8, 2003.

[86] J S Damoiseaux, S Rombouts, F Barkhof, P Scheltens, C J Stam, S M Smith, and C F Beckmann. Consistent resting-state networks. *Proceedings of the National Academy of Sciences of the United States of America*, 2006.

[87] M D Greicius, K Supekar, V Menon, and R F Dougherty. Resting-state functional connectivity reflects structural connectivity in the default mode network. *Cerebral Cortex*, 19(1):72–78, 2009.

[88] N Gaab, J D E Gabrieli, and G H Glover. Resting in peace or noise: Scanner background noise suppresses default-mode network. *Human Brain Mapping*, 29(7):858–867, 2008.

[89] W Edelstein, G Glover, C Hardy, and R Redington. The intrinsic signal-to-noise ration in NMR imaging. *Magnetic Resonance in Medicine*, 3:604–618, 1986.

[90] R M Birn. The role of physiological noise in resting-state functional connectivity. *NeuroImage*, 62(2):864–870, 2012.

[91] K Murphy, R M Birn, and P Bandettini. Resting-state fMRI confounds and cleanup. *NeuroImage*, 80:349–359, 2013.

[92] M A Griswold, P M Jakob, R M Heidemann, M Nittka, V Jellus, J Wang, B Kiefer, and A Haase. Generalized Autocalibrating Partially Parallel Acquisitions (GRAPPA). *Magnetic Resonance in Medicine*, 47(6):1202–1210, 2002.

[93] K P Pruessmann, M Weiger, M B Scheidegger, and P Boesiger. SENSE: Sensitivity encoding for fast MRI. *Magnetic Resonance in Medicine*, 42(5):952–962, 1999.

[94] Feinberg, D and Setsompop, K. Ultra-Fast MRI of the Human Brain with Simultaneous Multi-Slice Imaging. *Journal of Magnetic Resonance*, 18(9):1199–1216, 2013.

[95] D A Feinberg, S Moeller, S M Smith, E Auerbach, S Ramanna, M F Glasser, K L Miller, K Ugurbil, and E Yacoub. Multiplexed Echo Planar Imaging for Sub-Second Whole Brain FMRI and Fast Diffusion Imaging. *PLoS ONE*, 5(12):157–167, 2010.

[96] S Moeller, E Yacoub, C a. Olman, E Auerbach, J Strupp, N Harel, and K Uğurbil. Multiband multislice GE-EPI at 7 tesla, with 16-fold acceleration using partial parallel imaging with application to high spatial and temporal whole-brain FMRI. *Magnetic Resonance in Medicine*, 63(5):1144–1153, 2010.

[97] K Setsompop, B A Gagoski, J R Polimeni, T Witzel, V J Wedeen, and L L Wald. Blipped-controlled aliasing in parallel imaging for simultaneous multislice echo planar imaging with reduced g-factor penalty. *Magnetic Resonance in Medicine*, 67(5):1210–24, 2012.

[98] K Setsompop, D A Feinberg, and J R Polimeni. Rapid brain MRI acquisition techniques at ultra-high fields. *NMR in Biomedicine*, 29(9):1198–1221, 2016.

[99] S Ogawa, T M Lee, A R Kay, and D W Tank. Brain magnetic resonance imaging with contrast dependent on blood oxygenation. *Proceedings of the National Academy of Sciences of the United States of America*, 87(24):9868–72, 1990.

[100] R B Buxton, K Uludağ, D J Dubowitz, and T T Liu. Modeling the hemodynamic response to brain activation. *NeuroImage*, 23:220–233, 2004.

[101] A Puckett, K M Aquino, P Robinson, M Breakspear, and MM Schira. The 3D hemodynamic response function for depth-dependent fMRI of human cortex. *NeuroImage*, 139:240–248, 2016.

[102] L D Lewis, K Setsompop, B R Rosen, and J R Polimeni. Fast fMRI can detect oscillatory neural activity in humans. *Proceedings of the National Academy of Sciences*, 113(43):6679–6685, 2016.

[103] D Mantini, M G Perrucci, C Del Gratta, G L Romani, and M Corbetta. Electrophysiological signatures of resting state networks in the human brain. *Proceedings of the National Academy of Sciences*, 104(32):13170–13175, 2007.

[104] K Nizar, H Uhlirova, P Tian, P A Saisan, Q Cheng, L Reznichenko, K L Weldy, T C Steed, V B Sridhar, C L MacDonald, J Cui, S L Gratiy, S Sakadzic, D A Boas, T I Beka, G T Einevoll, J Chen, E Masliah, A M Dale, G A Silva, and A Devor. In vivo Stimulus-Induced Vasodilation Occurs without IP3 Receptor Activation and May Precede Astrocytic Calcium Increase. *Journal of Neuroscience*, 33(19):8411–8422, 2013.

[105] H Nilsson and C Aalkjaer. Vasomotion: Mechanisms and physiological importance. *Molecular Interventions*, 3(2):79–89, 2003.

[106] C Aalkjaer, D Boedtkjer, and V Matchkov. Vasomotion - what is currently thought? *Acta Physiologica*, 202(3):253–269, 2011.

[107] V Kiviniemi, X Wang, V Korhonen, T Keinänen, T Tuovinen, J Autio, P LeVan, S Keilholz, Y Zang, and J Hennig. Ultra-fast magnetic resonance encephalography of physiological brain activity–glymphatic pulsation mechanisms? *Journal of Cerebral Blood Flow & Metabolism*, 36(6):1033–1045, 2016.

[108] H Obrig, M Neufang, R Wenzel, M Kohl, J Steinbrink, K Einhäupl, and A Villringer. Spontaneous Low Frequency Oscillations of Cerebral Hemodynamics and Metabolism in Human Adults. *NeuroImage*, 12(6):623–639, 2000.

[109] J E Mayhew, S Askew, Y Zheng, J Porrill, G W Westby, P Redgrave, D M Rector, and R M Harper. Cerebral vasomotion: a 0.1-Hz oscillation in reflected light imaging of neural activity. *NeuroImage*, 4:183–93, 1996.

[110] P Patel, A J Kennerley, L Boorman, M Jones, and J Berwick. Does vasomotion alter functional connectivity? A multi-modal study using Optical Imaging Spectroscopy and BOLD fMRI. *Proceedings of the International Society of Magnetic Resonance in Medicine*, page 49, 2015.

[111] Mayer S. Studien zur physiologie des herzens und der blutgefässe.ueber spontane blutdruckschwankungen. *Kaiserliche Akademie der Wissenschaften Wien.*, 74:281–307, 1876.

[112] C Julien. The enigma of Mayer waves: Facts and models. *Cardiovascular Research*, 70(1):12–21, 2006.

[113] M Modarreszadeh and E N Bruce. Ventilatory variability induced by spontaneous variations of PaCO2 in humans. *Journal of Applied Physiology*, 76(6):2765 – 2775, 1994.

[114] R G Wise, K Ide, M J Poulin, and I Tracey. Resting fluctuations in arterial carbon dioxide induce significant low frequency variations in BOLD signal. *NeuroImage*, 21(4):1652–1664, 2004.

[115] A M Golestani, C Chang, J B Kwinta, Y B Khatamian, and J Jean Chen. Mapping the end-tidal CO2 response function in the resting-state BOLD fMRI signal: Spatial specificity, test-retest reliability and effect of fMRI sampling rate. *NeuroImage*, 104:266–277, 2015.

[116] S J Vannesjo, B J Wilm, Y Duerst, S Gross, D O Brunner, B E Dietrich, T Schmid, C Barmet, and K P Pruessmann. Retrospective correction of physiological field fluctuations in high-field brain mri using concurrent field monitoring. *Magnetic resonance in medicine*, 73(5):1833–1843, 2015.

[117] P-F Van de Moortele, J Pfeuffer, G H Glover, K Ugurbil, and X Hu. Respiration-induced B0 fluctuations and their spatial distribution in the human brain at 7 Tesla. *Magnetic Resonance in Medicine*, 47(5):888–895, 2002.

[118] C Windischberger, H Langenberger, T Sycha, E M Tschernko, G Fuchsjäger-Mayerl, L Schmetterer, and E Moser. On the origin of respiratory artifacts in BOLD-EPI of the human brain. *Magnetic Resonance Imaging*, 20(8):575–582, 2002.

[119] B P Poncelet, V J Wedeen, R M Weisskoff, and M S Cohen. Brain parenchyma motion: measurement with cine echo-planar MR imaging. *Radiology*, 185:645–651, 1992.

[120] S Akselrod, D Gordon, F F A Ubel, D D C Shannon, A Berger, R Cohen, A Clifford-Barger, R Cohen, A Berger, and R Cohen. Power spectrum analysis of heart rate fluctuation: a quantitative probe of beat-to-beat cardiovascular control. *Science*, 213:220–22, 1981.

[121] K Shmueli, P van Gelderen, J de Zwart, S G Horovitz, M Fukunaga, J M Jansma, and J H Duyn. Low-frequency fluctuations in the cardiac rate as a source of variance in the resting-state fMRI BOLD signal. *NeuroImage*, 38:306–320, 2007.

[122] A M Smith, B K Lewis, U E Ruttimann, F Q Ye, T M Sinnwell, Y Yang, J H Duyn, and J A Frank. Investigation of low frequency drift in fMRI signal. *Neuroimage*, 9(5):526–33, 1999.

[123] G K Aguirre, E Zarahn, and M D'esposito. The variability of human, bold hemodynamic responses. *Neuroimage*, 8(4):360–369, 1998.

[124] A M Puckett, K M Aquino, P A Robinson, M Breakspear, and M M Schira. The spatiotemporal hemodynamic response function for depth-dependent functional imaging of human cortex. *NeuroImage*, 139:240–248, 2016.

[125] N Vigneau-Roy, M Bernier, M Descoteaux, and K Whittingstall. Regional variations in vascular density correlate with resting-state and task-evoked blood oxygen level-dependent signal amplitude. *Human brain mapping*, 35(5):1906–1920, 2014.

[126] Clarisse I Mark, Erin L Mazerolle, and J Jean Chen. Metabolic and vascular origins of the bold effect: Implications for imaging pathology and resting-state brain function. *Journal of Magnetic Resonance Imaging*, 42(2):231–246, 2015.

[127] S M Kazan, S Mohammadi, M F Callaghan, G Flandin, L Huber, R Leech, A Kennerley, C Windischberger, and N Weiskopf. Vascular autorescaling of fMRI (VasA fMRI) improves sensitivity of population studies: A pilot study. *NeuroImage*, 124:794–805, 2015.

[128] H Yang, X Y Long, Y Yang, H Yan, C Z Zhu, X P Zhou, Y F Zang, and Q Y Gong. Amplitude of low frequency fluctuation within visual areas revealed by resting-state functional MRI. *NeuroImage*, 36(1):144–152, 2007.

[129] D Mao, Z Ding, W Jia, W Liao, X Li, H Huang, J Yuan, Y-F Zang, and H Zhang. Low-Frequency Fluctuations of the Resting Brain: High Magnitude Does Not Equal High Reliability. *Plos One*, 10(6):108–117, 2015.

[130] Q H Zou, C Z Zhu, Y Yang, X N Zuo, X Y Long, Q J Cao, Y F Wang, and Y F Zang. An improved approach to detection of amplitude of low-frequency fluctuation (ALFF) for resting-state fMRI: Fractional ALFF. *Journal of Neuroscience Methods*, 172:137–141, 2008.

[131] S Hu, H H a Chao, S Zhang, J S Ide, and C Shan R Li. Changes in cerebral morphometry and amplitude of low-frequency fluctuations of BOLD signals during healthy aging: Correlation with inhibitory control. *Brain Structure and Function*, 219(3):983–994, 2014.

[132] K A Tsvetanov, R N A Henson, L K Tyler, S W Davis, M A Shafto, J R Taylor, N Williams, C Cam, and J B Rowe. The effect of ageing on fMRI: Correction for the confounding effects of vascular reactivity evaluated by joint fMRI and MEG in 335 adults. *Human Brain Mapping*, 36(6):2248–2269, 2015.

[133] S J Zieman, V Melenovsky, and D A Kass. Mechanisms, pathophysiology, and therapy of arterial stiffness. *Arteriosclerosis, Thrombosis, and Vascular Biology*, 25(5):932–943, 2005.

[134] E G Lakatta and D Levy. Arterial and cardiac aging: Major shareholders in cardiovascular disease enterprises: Part I: Aging arteries: A "set up" for vascular disease. *Circulation*, 107(1):139–146, 2003.

[135] O Yildiz. Vascular smooth muscle and endothelial functions in aging. *Annals of the New York Academy of Sciences*, 1100:353–360, 2007.

[136] M D'Esposito, E Zarahn, G K Aguirre, and B Rypma. The effect of normal aging on the coupling of neural activity to the bold hemodynamic response. *NeuroImage*, 10(1):6 – 14, 1999.

[137] W Richter and M Richter. The shape of the fmri {BOLD} response in children and adults changes systematically with age. *NeuroImage*, 20(2):1122 – 1131, 2003.

[138] I Makedonov, S E Black, and B J MacIntosh. BOLD fMRI in the White Matter as a Marker of Aging and Small Vessel Disease. *PLoS ONE*, 8(7):1–9, 2013.

[139] I A D O'Brien, P O'Hare, and R J M Corrall. Heart rate variability in healthy subjects: effect of age and derivation of normal ranges for tests of autonomic function. *Heart*, 55:348–354, 1986.

[140] Beckmann, Mackay, Filippini, and Smith. Group comparison of resting-state FMRI data using multi-subject ICA and dual regression. *NeuroImage*, 47:S148, 2009.

[141] N Filippini, B J Macintosh, M G Hough, G M Goodwin, G B Frisoni, S M Smith, P M Matthews, C F Beckmann, and C E Mackay. Distinct patterns of brain activity in young carriers of the APOE-{varepsilon}4 allele. *Proceedings of the National Academy of Sciences of the United States of America*, 106(17):7209–7214, 2009.

[142] T. Hill and P. Lewicki. *Electronic Statistics Textbook*. StatSoft, Inc. Tulsa, OK. WEB: http://www.statsoft.com/textbook/, 2013. Accessed on 28.12.2016.

[143] J P Marques, T Kober, G Krueger, W van der Zwaag, P-F Van de Moortele, and R Gruetter. Mp2rage, a self bias-field corrected sequence for improved segmentation and t 1-mapping at high field. *Neuroimage*, 49(2):1271–1281, 2010.

[144] C Triantafyllou, R D Hoge, G Krueger, C J Wiggins, A Potthast, G C Wiggins, and L L Wald. Comparison of physiological noise at 1.5 T, 3 T and 7 T and optimization of fMRI acquisition parameters . *NeuroImage*, 26(1):243 – 250, 2005.

[145] S M Smith, M Jenkinson, M W Woolrich, C F Beckmann, T E J Behrens, H Johansen-Berg, P R Bannister, M De Luca, I Drobnjak, D E Flitney, R K Niazy, J Saunders, J Vickers, Y Zhang, N De Stefano, J M Brady, and P M Matthews. Advances in functional and structural MR image analysis and implementation as FSL. *NeuroImage*, 23:208–219, 2004.

[146] P Grolimund and R W Seiler. Age dependence of the flow velocity in the basal cerebral arteries - A transcranial Doppler ultrasound study. *Ultrasound in Medicine and Biology*, 14(3):191–198, 1988.

[147] J Martin, K J Friston, J G Colebatch, and R S Frackowiak. Decreases in regional cerebral blood flow with normal aging. *Journal of Cerebral Blood Flow and Metabolism*, 11:684–689, 1991.

[148] T Tarumi, M Ayaz-Khan, J Liu, B M Tseng, R Parker, J Riley, C Tinajero, and R Zhang. Cerebral hemodynamics in normal aging: central artery stiffness, wave reflection, and pressure pulsatility. *Journal of Cerebral Blood Flow & Metabolism*, 34(6):971–978, 2014.

[149] D Robertson, C F Tessmer, and R L Hughson. Association between arterial stiffness and cerebrovascular resistance in the elderly. *J Hum Hypertens*, 24(3):190–196, 2010.

[150] R Asmar, A Benetos, J Topouchian, P Laurent, B Pannier, A Brisac, R Target, and B I Levy. Assessment of arterial distensibility by automatic pulse wave velocity measurement validation and clinical application studies. *Hypertension*, 26(3):485–490, 1995.

[151] M E Wagshul, P K Eide, and J R Madsen. The pulsating brain: A review of experimental and clinical studies of intracranial pulsatility. *Fluids and barriers of the CNS*, 8(1):5, 2011.

[152] A Marmarou, K Shulman, and R M Rosende. A nonlinear analysis of the cerebrospinal fluid system and intracranial pressure dynamics. *Journal of neurosurgery*, 48(3):332–44, 1978.

[153] M Kosteljanetz. CSF dynamics and pressure-volume relationships in communicating hydrocephalus. *Journal of Neurosurgery*, 64(1):45–52, 1986.

[154] P; Bullock R Reilly. Intracranial Pressure Monitoring. *Head Injury*, pages 209 –216, 1997.

[155] R Aaslid, T M Markwalder, and H Nornes. Noninvasive transcranial Doppler ultrasound recording of flow velocity in basal cerebral arteries. *Journal of neurosurgery*, 57(6):769–774, 1982.

[156] F J Kirkham, T S Padayachee, S Parsons, L S Seargeant, F R House, and R G Gosling. Transcranial measurement of blood velocities in the basal cerebral arteries using pulsed Doppler ultrasound: Velocity as an index of flow. *Ultrasound in Medicine and Biology*, 12(1):15–21, 1986.

[157] M P Hartung, T M Grist, and C J François. Magnetic resonance angiography: current status and future directions. *Journal of Cardiovascular Magnetic Resonance*, 13(1):19, 2011.

[158] D R Enzmann and N J Pelc. Normal flow patterns of intracranial and spinal cerebrospinal fluid defined with phase-contrast cine MR imaging. *Radiology*, 178(2):467–474, 1991.

[159] W R Nitz, W G Bradley, a S Watanabe, R R Lee, B Burgoyne, R M O'Sullivan, and M D Herbst. Flow dynamics of cerebrospinal fluid: assessment with phase-contrast velocity MR imaging performed with retrospective cardiac gating. *Radiology*, 183(2):395–405, 1992.

[160] M Markl, A Frydrychowicz, S Kozerke, M Hope, and O Wieben. 4D flow MRI. *Journal of Magnetic Resonance Imaging*, 36:1015–1036, 2012.

[161] P Wahlin, K Ambarki, R Birgander, O Wieben, K M Johnson, J Malm, and A Eklund. Measuring Pulsatile Flow in Cerebral Arteries Using 4D Phase-Contrast MR Imaging. *American Journal of Neuroradiology*, 34:1740–1745, 2013.

[162] L Yan, C Li, E Kilroy, F W Wehrli, and D J J Wang. Quantification of arterial cerebral blood volume using multiphase-balanced SSFP-based ASL. *Magnetic Resonance in Medicine*, 68(1):130–139, 2012.

[163] L Yan, C Y. Liu, R X Smith, M Jog, M Langham, K Krasileva, Y Chen, J M Ringman, and D J J Wang. Assessing intracranial vascular compliance using dynamic arterial spin labeling. *NeuroImage*, 124:433–441, 2016.

[164] M Bianciardi, N Toschi, J R Polimeni, K C Evans, H Bhat, B Keil, B R Rosen, D A Boas, and L L Wald. The pulsatility volume index: an indicator of cerebrovascular compliance based on fast magnetic resonance imaging of cardiac and respiratory pulsatility. *Philosophical Transactions of the Royal Society A: Mathematical, Physical and Engineering Sciences*, 374:20150184, 2016.

[165] E AH Warnert, K Murphy, J E Hall, and R G Wise. Noninvasive assessment of arterial compliance of human cerebral arteries with short inversion time arterial spin labeling. *Journal of Cerebral Blood Flow & Metabolism*, 35(3):461–468, 2015.

[166] E AH Warnert, E C Hart, J E Hall, K Murphy, and RG Wise. The major cerebral arteries proximal to the circle of willis contribute to cerebrovascular resistance in humans. *Journal of Cerebral Blood Flow & Metabolism*, 36(8):1384–1395, 2016.

[167] A J S Webb, M Simoni, S Mazzucco, W Kuker, U Schulz, and P M Rothwell. Increased cerebral arterial pulsatility in patients with leukoaraiosis: Arterial stiffness enhances transmission of aortic pulsatility. *Stroke*, 43(10):2631–2636, 2012.

[168] G Krüger and G H Glover. Physiological noise in oxygenation-sensitive magnetic resonance imaging. *Magnetic Resonance in Medicine*, 46(4):631–637, 2001.

[169] M S Dagli, J E Ingeholm, and J V Haxby. Localization of cardiac-induced signal change in fMRI. *NeuroImage*, 9(4):407–15, 1999.

[170] Y Tong and B deB. Frederick. Studying the Spatial Distribution of Physiological Effects on BOLD Signals Using Ultrafast fMRI. *Frontiers in Human Neuroscience*, 8:1–8, 2014.

[171] Y Zheng, X Chen, A Yao, H Lin, Y Shen, and Y Zhu. Shear Wave Propagation in Soft Tissue and Ultrasound Vibrometry. *In Tech*, pages 1–24, 2013.

[172] B Rashid, M Destrade, and M D Gilchrist. Mechanical characterization of brain tissue in tension at dynamic strain rates. *Journal of the mechanical behavior of biomedical materials*, 33:43–54, 2014.

[173] J Hennig, K Zhong, and O Speck. Mr-encephalography: Fast multi-channel monitoring of brain physiology with magnetic resonance. *NeuroImage*, 34(1):212 – 219, 2007.

[174] R Bammer, T A. Hope, M Aksoy, and M T Alley. Time-resolved 3d quantitative flow mri of the major intracranial vessels: Initial experience and comparative evaluation at 1.5t and 3.0t in combination with parallel imaging. *Magnetic Resonance in Medicine*, 57(1):127–140, 2007.

[175] C K Kang, C A Park, D S Lee, Y B Lee, C W Park, Y B Kim, and Z H Cho. Velocity measurement of microvessels using phase-contrast magnetic resonance angiography at 7 tesla MRI. *Magnetic Resonance in Medicine*, 75(4):1640–1646, 2016.

[176] W H Bouvy, L J Geurts, H J Kuijf, P R Luijten, L J Kappelle, G J Biessels, and J J M Zwanenburg. Assessment of blood flow velocity and pulsatility in cerebral perforating arteries with 7-T quantitative flow MRI. *NMR in Biomedicine*, 29(9):1295–1304, 2016.

[177] F Schuchardt, L Schroeder, C Anastasopoulos, M Markl, J Bäuerle, A Hennemuth, J Drexl, J M Valdueza, I Mader, and A Harloff. In vivo analysis of physiological 3D blood flow of cerebral veins. *European Radiology*, 25(8):2371–2380, 2015.

[178] D C Zhu, M Xenos, A A Linninger, and R D Penn. Dynamics of lateral ventricle and cerebrospinal fluid in normal and hydrocephalic brains. *Journal of Magnetic Resonance Imaging*, 24(4):756–770, 2006.

[179] Bernstein, M A and King, K F and Zhou, X J. Handbook of MRI Pulse Sequences. *Elsevier*, XXXIII, 2004.

[180] K Obata, T T Liu, K L Miller, W M Luh, E C Wong, L R Frank, and R B Buxton. Discrepancies between BOLD and flow dynamics in primary and supplementary motor areas: Application of the balloon model to the interpretation of BOLD transients. *NeuroImage*, 21(1):144–153, 2004.

[181] K Uludağ, B Müller-Bierl, and K Uğurbil. An integrative model for neuronal activity-induced signal changes for gradient and spin echo functional imaging. *NeuroImage*, 48(1):150–165, 2009.

[182] S Sakadžić, E T Mandeville, L Gagnon, J J Musacchia, M A Yaseen, M A Yucel, J Lefebvre, F Lesage, A M Dale, K Eikermann-Haerter, C Ayata, V J Srinivasan, E H Lo, A Devor, and D A Boas. Large arteriolar component of oxygen delivery implies a safe margin of oxygen supply to cerebral tissue. *Nature Communications*, 5:5734, 2014.

[183] J M Zhao, C S Clingman, M J Närväinen, R A Kauppinen, and P van Zijl. Oxygenation and hematocrit dependence of transverse relaxation rates of blood at 3t. *Magnetic resonance in medicine*, 58(3):592–597, 2007.

[184] J E Cremer and M P Seville. Regional brain blood flow, blood volume, and haematocrit values in the adult rat. *Journal of Cerebral Blood Flow and Metabolism*, 3(2):254–6, 1983.

[185] A R Pries, T W Secomb, and P Gaehtgens. Biophysical aspects of blood flow in the microvasculature. *Cardiovascular Research*, 32(4):654–667, 1996.

[186] E Rostrup, G M Knudsen, I Law, S Holm, H B W Larsson, and O B Paulson. The relationship between cerebral blood flow and volume in humans. *NeuroImage*, 24(1):1–11, 2005.

[187] P Herscovitch and M E Raichle. What is the correct value for the brain–blood partition coefficient for water? *Journal of Cerebral Blood Flow and Metabolism*, 5(1):65–69, 1985.

[188] X Hu, Tuong Huu Le, P T, and P Erhard. Retrospective estimation and correction of physiological fluctuation in functional MRI. *Magnetic Resonance in Medicine*, 34(2):201–212, 1995.

[189] P A Gowland and R Bowtell. Theoretical optimization of multi-echo fMRI data acquisition. *Physics in medicine and biology*, 52(7):1801–1813, 2007.

[190] D A Boas, S R Jones, A Devor, T J Huppert, and A M Dale. A vascular anatomical network model of the spatio-temporal response to brain activation. *NeuroImage*, 40(3):1116–1129, 2008.

[191] B Mokri. The monro–kellie hypothesis applications in csf volume depletion. *Neurology*, 56(12):1746–1748, 2001.

[192] D Ivanov, A Schäfer, A Deistung, M N Streicher, S Kabisch, I Henseler, E Roggenhofer, T H Jochimsen, J Reichenbach, K Uludag, and R Turner. In vivo estimation of the transverse relaxation time dependence of blood on oxygenation at 7 tesla. *Proceedings of the International Society of Magnetic Resonance in Medicine*, page 2472, 2013.

[193] J Xu, S Moeller, E J Auerbach, J Strupp, S M Smith, D A Feinberg, and Kl Yacoub, Eand Uğurbil. Evaluation of slice accelerations using multiband echo planar imaging at 3t. *Neuroimage*, 83:991–1001, 2013.

[194] M Czosnyka and J D Pickard. Monitoring and interpretation of intracranial pressure. *Journal of Neurology, Neurosurgery & Psychiatry*, 75(6):813–821, 2004.

[195] L Huber, J Goense, A J Kennerley, D Ivanov, S N Krieger, J Lepsien, R Trampel, R Turner, and H E Möller. Investigation of the neurovascular coupling in positive and negative BOLD responses in human brain at 7T. *NeuroImage*, 97:349–362, 2014.

[196] L Gagnon, S Sakadzic, F Lesage, J J Musacchia, J Lefebvre, Q Fang, M Yucel, K C Evans, E T Mandeville, J. Cohen-Adad, J R Polimeni, M Yaseen, E H Lo, D N Greve, R B Buxton, M Dale, A Devor, and D Boas. Quantifying the Microvascular Origin of BOLD-fMRI from First Principles with Two-Photon Microscopy and an Oxygen-Sensitive Nanoprobe. *Journal of Neuroscience*, 35(8):3663–3675, 2015.

[197] M J Cipolla. *The cerebral circulation*, volume 1. Morgan & Claypool Publishers, 2009.

[198] M Czosnyka, Z Czosnyka, S Momjian, and J D Pickard. Cerebrospinal fluid dynamics. *Physiological measurement*, 25(5), 2004.

[199] R Turner and D Thomas. Cerebral blood volume: Measurement and change. *Proceedings of the International Society of Magnetic Resonance in Medicine*, page 2771, 2006.

[200] S N Krieger, M N Streicher, R Trampel, and R Turner. Cerebral blood volume changes during brain activation. *Journal of Cerebral Blood Flow and Metabolism*, 32(8):1618–31, 2012.

[201] Yufen Chen, DJJ. Wang, and J A Detre. Comparison of arterial transit times estimated using arterial spin labeling. *Magnetic Resonance Materials in Physics, Biology and Medicine*, 25(2):135–144, 2012.

[202] H BW Larsson, M B Vestergaard, U Lindberg, H K Iversen, and S P Cramer. Brain capillary transit time heterogeneity in healthy volunteers measured by dynamic contrast-enhanced t1-weighted perfusion mri. *Journal of Magnetic Resonance Imaging*, 45(6):1809–1820, 2017.

[203] J J Iliff, M Wang, Y Liao, B Plogg, W Peng, G Gundersen, H Benveniste, G E Vates, R Deane, S Goldman, E Nagelhus, and M Nedergaard. A Paravascular Pathway Facilitates CSF Flow Through the Brain Parenchyma and the Clearance of Interstitial Solutes, Including Amyloid . *Science Translational Medicine*, 4(147):1–11, 2012.

[204] J J Iliff, M Wang, D M Zeppenfeld, B a Venkataraman, Aand Plog, Y Liao, R Deane, and M Nedergaard. Cerebral arterial pulsation drives paravascular CSF-interstitial fluid exchange in the murine brain. *The Journal of neuroscience : the official journal of the Society for Neuroscience*, 33(46):18190–9, 2013.

[205] A Scouten and R T Constable. VASO-based calculations of CBV change: Accounting for the dynamic CSF volume. *Magnetic Resonance in Medicine*, 59(2):308–315, 2008.

[206] A Scouten and RT Constable. Applications and limitations of whole-brain magic vaso functional imaging. *Magnetic resonance in medicine*, 58(2):306–315, 2007.

[207] F N. Van De Vosse and N Stergiopulos. Pulse Wave Propagation in the Arterial Tree. *Annual Review in Fluid Mechanics*, 43:467–99, 2011.

[208] W B Kannel, P A Wolf, D L McGee, T R Dawber, P McNamara, and W P Castelli. Systolic blood pressure, arterial rigidity, and risk of stroke. The Framingham study. *Jama*, 245(12):1225–1229, 1981.

[209] G F Mitchell, H Parise, E J Benjamin, M G Larson, M J Keyes, J A Vita, R S Vasan, and D Levy. Changes in arterial stiffness and wave reflection with advancing age in healthy men and women: The Framingham Heart Study. *Hypertension*, 43(6):1239–1245, 2004.

[210] D Gallichan, J P Marques, and R Gruetter. Retrospective correction of involuntary microscopic head movement using highly accelerated fat image navigators (3d fatnavs) at 7t. *Magnetic Resonance in Medicine*, 75(3):1030–1039, 2016.

[211] M D Tisdall, A T Hess, M Reuter, E M Meintjes, B Fischl, and A J W van der Kouwe. Volumetric navigators for prospective motion correction and selective reacquisition in neuroanatomical mri. *Magnetic Resonance in Medicine*, 68(2):389–399, 2012.

[212] R Frost, A T Hess, T W Okell, M A Chappell, M D Tisdall, A JW van der Kouwe, and P Jezzard. Prospective motion correction and selective reacquisition using volumetric navigators for vessel-encoded arterial spin labeling dynamic angiography. *Magnetic resonance in medicine*, 76(5):1420–1430, 2016.

[213] S Skare and J L R Andersson. On the effects of gating in diffusion imaging of the brain using single shot epi. *Magnetic Resonance Imaging*, 19(8):1125 – 1128, 2001.

[214] P Comon. Independent component analysis, a new concept? *Signal Processing*, 36(3):287 – 314, 1994.

[215] V Kiviniemi, J H Kantola, J Jauhiainen, A Hyvärinen, and O Tervonen. Independent component analysis of nondeterministic fmri signal sources. *NeuroImage*, 19(2):253 – 260, 2003.

[216] C F Beckmann. Investigations into resting-state connectivity using independent component analysis. *Philosophical Transactions of the Royal Society*, 360:1001–1013, 2005.

[217] L Griffanti, G Salimi-Khorshidi, C F Beckmann, E J Auerbach, G Douaud, C E Sexton, E Zsoldos, K P Ebmeier, N Filippini, C E Mackay, S Moeller, J Xu, E Yacoub, G Baselli, K Ugurbil, K L Miller, and S M Smith. Ica-based artefact removal and accelerated fmri acquisition for improved resting state network imaging. *NeuroImage*, 95:232 – 247, 2014.

[218] L Griffanti, G Douaud, J Bijsterbosch, S Evangelisti, F Alfaro-Almagro, M F Glasser, E P Duff, S Fitzgibbon, R Westphal, D Carone, C F Beckmann, and S M Smith. Hand classification of fmri ica noise components. *NeuroImage*, 154:188 – 205, 2017.

[219] B Zahneisen, T Grotz, K J Lee, S Ohlendorf, M Reisert, M Zaitsev, and J Hennig. Three-dimensional mr-encephalography: Fast volumetric brain imaging using rosette trajectories. *Magnetic Resonance in Medicine*, 65(5):1260–1268, 2011.

[220] Renvall V, Witzel T, Bianciardi M, Polimeni J R. Multi-contrast inversion-recovery EPI (MI-EPI) functional MRI at 7T. *Proceedings of the International Society of Magnetic Resonance in Medicine*, page 14075, 2014.

[221] Ville Renvall, Thomas Witzel, Lawrence L. Wald, and Jonathan R. Polimeni. Automatic cortical surface reconstruction of high-resolution t1 echo planar imaging data. *NeuroImage*, 134:338 – 354, 2016.

[222] Yiming Lei, Hongbin Han, Fan Yuan, Aqeel Javeed, and Yong Zhao. The brain interstitial system: Anatomy, modeling, in vivo measurement, and applications. *Progress in Neurobiology*, Article in press, 2016.

[223] I Markuerkiaga, M Barth, and D G Norris. A cortical vascular model for examining the specificity of the laminar BOLD signal. *NeuroImage*, 132:491–498, 2016.

[224] B Weber, A L Keller, J Reichold, and N K Logothetis. The microvascular system of the striate and extrastriate visual cortex of the macaque. *Cerebral Cortex*, 18(10):2318, 2008.

[225] S Laurent, J Cockcroft, L Van Bortel, P Boutouyrie, C Giannattasio, D Hayoz, B Pannier, C Vlachopoulos, I Wilkinson, and Struijker-Boudier. Expert consensus document on arterial stiffness: methodological issues and clinical applications. *European Heart Journal*, 27(21):2588, 2006.

[226] H Ito, I Kanno, M Ibaraki, J Hatazawa, and S Miura. Changes in human cerebral blood flow and cerebral blood volume during hypercapnia and hypocapnia measured by positron emission tomography. *Journal of Cerebral Blood Flow and Metabolism*, 23(6):665–670, 2003.

[227] A Battisti-Charbonney, J Fisher, and J Duffin. The cerebrovascular response to carbon dioxide in humans. *The Journal of physiology*, 589(Pt 12):3039–48, 2011.

Appendices

Appendix A

How to run variable flip angle simulations

This section provides instructions how to reproduce or run a new variable flip angle optimisation. The original C++ code was generously provided by John Mugler (University of Virginia) and is to my knowledge the exact code that is used by the Siemens product code to calculate variable flip angle schemes. To simulate variable flip angle schemes the following files are needed:

- `evolutions.h`
- `variable_flip_anlges.cpp`
- `variable_flip_angles.h`
- `sim12e_vfa.cpp`

They have to be compiled together. I used Microsoft Visual Studio C++ (MSDEV), which is already installed in the virtual machine image. However, there may be a more modern and classier way to do this.

`evolutions.h`

This h file defines the functions for different evolution schemes, i.e. how the shape of the "prescribed" magnetisation evolution should look like. The scheme type is set in `variable_flip_angles.cpp`. For example a T_1-w flip angle scheme should aim to have a constant magnetisation at the beginning of the readout train, whereas a T_2-w scheme aims to keep the signal flat midway through the echo train (k-space centre). The T_1-w suitable schemes are the "`ShortTE_TYPE0X`". T_2-w suitable schemes are the "`EXPO_FLAT_EXPO_Type0X`" schemes, that define a magnetisation course that initially decays exponentially, then stays constant before it decays exponentially towards the end of the ETL. Linear ramps and other schemes can be found here as well. I did not change anything in this file.

`variable_flip_angles.h`

This file is important to set evolution time constants. evolutions.h defines a template function, but the time constants for exponential decays, slopes of linear ramps and durations of various evolution segments have to be initialised here. The evolution shape in this work was "`T2W_TYPE01_1000ms`". The evolution parameter values used in our work can be altered in `EVOLUTION_PARAM_ARRAY{}`.

`variable_flip_angles.cpp`

This is where the meat is. All functions and classes for the Bloch simulations (RF excitation, T_1/T_2 relaxations/decays, rotations, spoiling etc.) are defined here. The optimal flip angles are searched for using interval bisection in the function `OptimizeRefocusingFA(){}`. If a flip angle exceeds/is below the target signal evolution the signal shape will be lower/raised. The flip

angle schemes themselves are calculated in `CalculateRefocusingFA(){}`. I did not change anything in this file. An important preprocessor statement in the beginning of the code is the `#undef IN_A_PULSE_Sequence`. This will be defined on the scanner, but not for "standalone testing" for our simulations.

`sim12e_vfa.cpp`

This file is used for the actual simulations. Evolution shapes can be chosen and protocol settings, such as ETLs and ESPs need to be set here. It is also possible to simulate B_1 inhomogeneity (in terms of nominal flip angle deviation) that will be taken into account for the flip angle calculation. Two sets of T_1/T_2 can be set here. One set are the relaxation constants of the target tissue you want to optimise the flip angles for. The other set are the relaxation constants of any other tissue you would like to calculate the magnetisation evolution under the optimal flip angle scheme of the target tissue. I implemented loops around the simulation code with a range of T_1/T_2 combinations that cover tissues from vessel wall, white matter, grey matter, blood and CSF. The following lines are excerpts of the relevant code. The original .cpp files can be searched for my modifications and edits by searching for "`\\OVOX`"

```
bool main {
\\OVOXstart:  SIMULATION LOOPs
\\OVOX: Initialise the T1 and T2 values that are used for the calculation
of the variable flip angles.  Initialise the T1 and T2 values that
are used for the simulation.  The simulated T1 and T2 values should
be realistic values for white matter at 7T. Define start value, increment
and end value of T1 and T2s.
double dCalculateT1Start = 500;
```

```
double dCalculateT2Start = 20;
double dSimulateT1Start = 700;
...
double dCalculateT1Incr = 100;
double dCalculateT2Incr = 5;
double dSimulateT1Incr = 100;
double dSimulateT2Incr = 5;
double dCalculateT1 = dCalculateT1Start;
...
\\OVOX: Simulation loop over calculation T1
while(dCalculateT1 < dCalculateT1End )
{
\\OVOX: Increment T1 value for calculation of variable flip angle
dCalculateT1 += dCalculateT1Incr;
//OVOX: Reset the calculation T2 value
dCalculateT2 = dCalculateT2Start;
\\OVOX: Simulation loop over calculation T2
while(dCalculateT2 < dCalculateT2End)
...
```

Within the simulation code I exported each optimal flip angle scheme and the magnetisation evolution as a `.txt` file. I used the `.txt` files then to read them into Matlab via a shared disk with the virtual machine:

```
ofstream outfile2("Y:\\Shared Disk\\Mugler_Sim_Results\\
calculated_evolution.txt");
for (size_t k = 0; k != vdEvolution.size(); ++k)
{
sprintf(outext"%6.1lf %6.4lf", k*dESPms, vdEvolution[k]);
```

```
outfile2 << outext << endl;
```

}

A script in Matlab would then plot schemes nicely and allow an easier comparison of magnetisation curves, PSF analysis etc.

Appendix B

χ^2 - goodness of fit for measured vs. simulated data

This section is largely build on an online lecture at "*http* : *//maxwell.ucsc.edu/%7Edrip/133/ch4.pdf*".

To assess the goodness of fit for our simulated data in Chapter 4 we used χ^2 statistics. The χ^2 value is defined as

$$\chi^2 = \sum_{j=1}^{n} \frac{(m_j - s_j)^2}{\sigma_j^2}\,, \tag{B.1}$$

where m_j are the measured data points and s_j the simulated data points from our model, σ_j^2 is the variance of our measured data points and n is the total number of samples. In the ideal case the measured and simulated values are equal and χ^2 equals zero.

Each χ^2 value is associated with a probability density distribution given the "number of degrees of freedom" ν. The degrees of freedom are the number of samples n minus the number of model or fit parameters we vary in our simulated data. In our case we have 10 measurement points and test for two

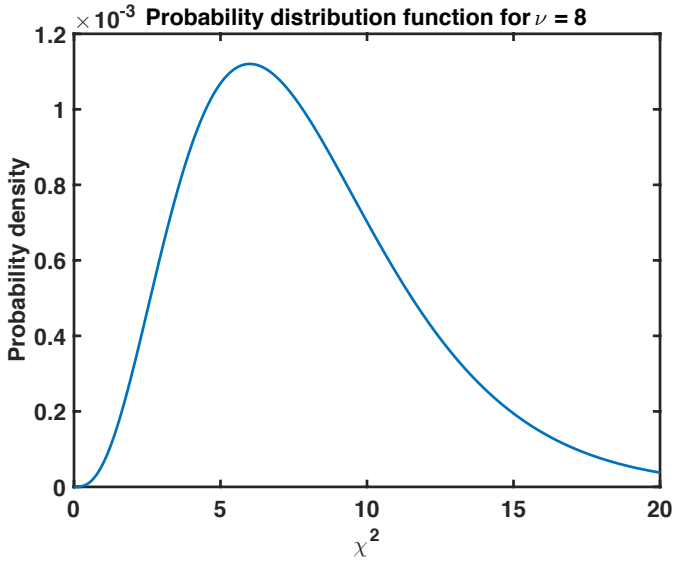


Figure B.1: χ^2 probability density distribution for 8 degrees of freedom.

parameters - the temporal shift of blood volume fluctuation and the scaling factor between S_0 and blood volume change, τ_d and d respectively. Hence, we have to calculate the χ^2 distribution for $\nu = 8$. The general form of the probability density distribution for a given ν is given by

$$p(\chi^2) = \frac{e^{-\chi^2/2}\,(\chi^2)^{\nu/2-1}}{2^{\nu/2}\Gamma(\nu/2)} \tag{B.2}$$

where Γ is the gamma function. Figure B.1 shows the probability density distribution for $\nu = 8$. To test to what significance level α our simulated model fits the measured data we can then calculate the sum under the curve of the distribution

$$\alpha(\chi^2) = \int_{\chi^2}^{\infty} p(\tilde{\chi^2})\,\mathrm{d}\tilde{\chi^2})\,. \tag{B.3}$$

Usually the χ^2 is reported per degree of freedom, i.e. χ^2/ν. Figure B.2 shows the $\alpha(\chi^2)$ per normalised χ^2/ν. If we find that the calculated χ^2/ν from our model fit is larger than the χ^2/ν in Figure B.2 for a desired significance level

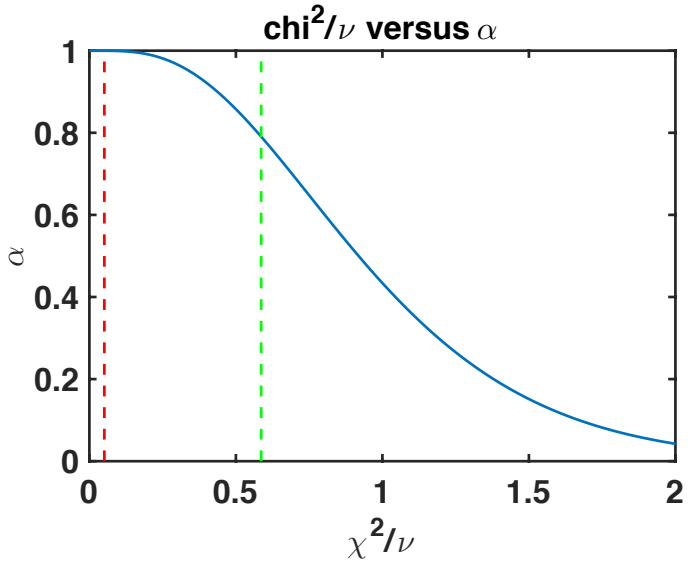


Figure B.2: α distribution per normalised χ^2/ν.The red and green dotted lines indicate the χ^2/ν from our model fit in Chapter 4, for the dynamic CSF volume and the parenchymal volume model respectively.

of α, our model is likely not a good choice and with a confidence level of $1-\alpha$ the model should be rejected.